

Brain stimulation techniques with the aid of nonlinear delayed neurofeedback and MEG inverse methods

vorgelegt von
Diplom-Physiker
Volker Hadamschek
aus Krefeld

Von der Fakultät II - Mathematik und Naturwissenschaften
der Technischen Universität Berlin
zur Erlangung des akademischen Grades
Doktor der Naturwissenschaften
Dr. rer. nat.

genehmigte Dissertation

Promotionsausschuss:

Vorsitzender: Prof. Dr. rer. nat. Erwin Sedlmayr
Berichter: Prof. Dr. rer. nat. Eckehard Schöll
Berichter: Prof. Dr. rer. nat. Dr. med. Peter A. Tass

Tag der wissenschaftlichen Aussprache: 28.6.2006

Berlin 2006

D 83

Meiner Mutter, Gisela Hadamschek
Meinem Vater, Gerd Hadamschek

Abstract

In order to apply model-based neurofeedback methods for the regulation of brain rhythms, an appropriate biomagnetic inverse routine has been developed. This technique has been implemented in a realtime system which processes *magnetoencephalography* (MEG) signals for the feedback. Linear and nonlinear delayed feedback protocols have been investigated in an MEG experiment with visual stimulation. The superposition of neural activity from different brain areas in the feedback signal is unavoidable in MEG. The influence of this MEG characteristic on nonlinear delayed feedback has been studied in a model of interacting neural ensembles.

A benchmark of common distributed source models for the reconstruction of the current density distribution in the brain from MEG data has been performed. For this, the reconstruction of single and multiple current dipoles has been simulated varying their position and orientation across the source space. The presence of detector noise has been taken into account. With respect to realtime applications a weighted Minimum Norm method called GaussMN, which has been tested here against other state-of-the-art algorithms for the first time, showed the best accuracy. A useful regularization routine has been developed.

A spatial filter system has been produced to reduce the cross-contamination from different brain regions in the reconstructed current densities. In numerical simulations it exhibited a significantly better performance than alternative techniques.

A nonlinear delayed feedback method recently proposed for the regulation of brain rhythms is investigated in interacting ensembles of coupled limit cycle oscillators. With respect to the desynchronization and decoupling of two interacting populations, an adequate mixing of their mean fields for the calculation of the stimulation signal leads to an enhanced effect. This is explained by studying the induced phase shift between the synchronized mean fields. A modeling approach for an analytical understanding is given.

The realtime current density reconstruction is verified in phantom experiments. An MEG experiment applying visual delayed neurofeedback in a healthy subject has been performed. The nonlinear delayed feedback method shows a strong suppression of a brain rhythm in this *proof of principle*. Using more localized brain activity for the feedback signal enhances the effect.

Zusammenfassung

Um modellbasierte Rückkoppelungsmethoden zur Regelung von Hirnrhythmen anzuwenden, wurde eine geeignete biomagnetische Inversmethode entwickelt. Diese Routine wurde in einem Echtzeit-System implementiert, welches die rückgekoppelten Signale auf der Grundlage von *Magnetenzephalographie* (MEG) Daten berechnet. Lineare und nichtlineare zeitverzögerte Rückkoppelungsprotokolle sind in einem MEG Experiment mit visueller Stimulation untersucht worden. Die Überlagerung von neuronaler Aktivität aus unterschiedlichen Gehirnregionen in dem rückgekoppelten Signal ist bei Verwendung der Magnetenzephalographie unvermeidbar. Der Einfluss dieser MEG Charakteristik auf nichtlineare zeitverzögerte Rückkoppelung wurde in einem Modell interagierender neuronaler Populationen studiert.

Ein Vergleichstest bekannter Verteilte-Quellen-Modelle zur Rekonstruktion der zerebralen Stromdichteverteilung aus MEG Signalen wurde durchgeführt. Hierfür wurde unter Variierung ihrer Position und Orientierung die Rekonstruktion von Stromdipolen simuliert. Der Einfluss von Detektorrauschen wurde in den Simulationen berücksichtigt. Bezüglich Echtzeit-Anwendungen zeigte eine gewichtete Minimum-Norm Methode namens GaussMN, die in dieser Arbeit zum ersten Mal mit anderen üblichen Algorithmen verglichen wurde, die höchste Genauigkeit. Eine geeignete Regularisierungsprozedur wurde erstellt.

Ein räumlicher Filter zur Reduzierung der Überlagerung von Signalen aus unterschiedlichen Hirnregionen in den rekonstruierten Stromdichten wurde entwickelt. In numerischen Simulationen zeigte diese Methode eine signifikant bessere Güte als alternative Verfahren.

Ein nichtlineares zeitverzögertes Rückkoppelungsprotokoll, das kürzlich zur Regelung von Hirnrhythmen vorgeschlagen wurde, ist in interagierenden Ensembles gekoppelter Oszillatoren theoretisch studiert worden. Bezüglich der Desynchronisation und Entkoppelung zweier interagierender Populationen, führt eine adäquate Überlagerung ihrer Felder zur Berechnung des Stimulationssignals zu einem verstärkten Effekt. Dieser kann mit Hilfe der relativen Phasenlage der synchronisierten Felder erklärt werden. Ein Modellierungsansatz auf dem Weg zu einem analytischen Verständnis ist gegeben.

Die Rekonstruktion der Stromdichteverteilung in Echtzeit wurde mit Hilfe von Messungen an einem Phantom validiert. Ein MEG Experiment unter Verwendung von visuellen zeitverzögerten Rückkoppelungsverfahren wurde an einem gesunden Probanden durchgeführt. Die nichtlineare zeitverzögerte Rückkoppelungsmethode zeigte eine starke Suppression eines Hirnrhythmus. Die Verwendung räumlich lokalisierter Hirnaktivität für das rückgekoppelte Signal steigert diesen Effekt.

Contents

List of figures	VI
List of tables	VIII
1 Introduction	1
2 Magnetoencephalography	3
2.1 Basics	3
2.2 Forward problem	5
2.3 Lead fields	6
2.4 Biomagnetic inverse problem	7
2.4.1 Ill-posed problem	7
2.4.2 Tikhonov regularization	8
2.4.3 Singular value decomposition	9
2.4.4 Cross-validation	11
2.4.5 Assumptions in distributed source models	11
3 Comparative study of inverse methods	13
3.1 Tested distributed source models	14
3.1.1 Weighted Minimum Norm methods	14
3.1.2 sLORETA	15
3.1.3 MFT	16
3.2 Setup of the simulations	17
3.2.1 Configuration of the source space and the sensors	17
3.2.2 Simulated detector signals	18
3.2.3 Measures to quantify the reconstruction performance	18
3.2.4 Defining subregions in the source space	19
3.2.5 Two-dipole configurations	19
3.3 Results	21
3.3.1 Single dipole reconstructions	22
3.3.2 Influence of regularization	24
3.3.3 Two-dipole reconstructions	26
3.4 Discussion	31

4	Specialized distributed source models	41
4.1	SOFIA	42
4.2	WROP	46
4.3	Tests concerning the ability of brain region localization	51
4.3.1	Adjusting methods	51
4.3.2	Results	53
5	Desynchronization of neural populations by delayed feedback	63
5.1	Phase shift in nonlinear delayed feedback	64
5.2	Distributed source models in a nonlinear delayed feedback scenario	67
5.3	Mixed nonlinear delayed feedback	72
5.3.1	Desynchronization and decoupling of interacting populations	73
5.3.2	Mixing the mean fields for the stimulation of interacting populations	75
5.3.3	Modeling ensembles by macroscopic oscillators	81
6	Realtime MEG	85
6.1	Implementation	85
6.2	Phantom tests	87
6.3	Visual delayed feedback in an MEG experiment	89
7	Conclusions and outlook	99
A	Equivalent descriptions of the current density distribution in the Tikhonov regularization	101
B	Covariance matrices of multi-dimensional Gaussian distributions	102
C	Physical meaning of the Laplacian operator	104
D	Implementation of the nonlinear delayed feedback in the experiment	105
	Bibliography	106
	Publications	112

List of Figures

2.1	MEG system at the Research Centre Jülich	4
2.2	Sketch of a pyramidal cell	5
3.1	Weighting profiles for lfMN and GaussMN	15
3.2	Exemplary reconstruction of a current dipole	17
3.3	Defining subregions in the source space	19
3.4	Parallel two dipole configurations I	21
3.5	Orthogonal two dipole configurations II	22
3.6	Tomographic view of the displacement errors for single dipole reconstructions . .	24
3.7	Tomographic view of the volume of activity for single dipole reconstructions . .	25
3.8	Measures in dependence of the setting of the regularization parameter α	26
3.9	Measures in dependence of the setting of the truncating value	27
3.10	Exemplary reconstructions for parallel configurations I	28
3.11	Exemplary reconstructions for antiparallel configurations I	30
3.12	Activity deviations and averaged activity deviation for configuration I	31
3.13	Exemplary reconstructions for antiparallel configurations II	32
3.14	Exemplary reconstructions for orthogonal configurations II	33
4.1	Degree of localization of the virtual lead fields in SOFIA	53
4.2	Exemplary reconstructions of a single current dipole situated inside the ROI . . .	60
4.3	Exemplary reconstructions of a single current dipole situated outside the ROI . .	61
4.4	Resolution kernels for GaussMN, SOFIA, WROP, and pWROP	62
5.1	Influence of the phase shift in the nonlinear delayed feedback on the order parameter	66
5.2	Order parameter in dependence of stimulation strength and the time delay (from: [THP06])	67
5.3	Order parameter in dependence of the mixing parameter ϵ for uncoupled ensembles	70
5.4	Influence of perturbing sources on the degree of synchronization for different inverse methods	71
5.5	Sketch of interacting ensembles with nonlinear delayed feedback	73
5.6	Trajectories of mean fields for two interacting ensembles stimulated with nonlin- ear delayed feedback	74
5.7	Exemplary trajectories of oscillators during nonlinear delayed feedback	75
5.8	Order parameters for both population versus mixing parameter ϵ	76
5.9	Mean frequency deviations versus mixing parameter ϵ	77

5.10	Trajectories of mean fields stimulated with mixed nonlinear delayed feedback . .	77
5.11	Exemplary trajectories of oscillators during mixed nonlinear delayed feedback . .	78
5.12	Synchronization indices for the mixed nonlinear delayed feedback between the mean fields and the stimulation signal	79
5.13	Mean phase differences for the mixed nonlinear delayed feedback between the mean fields and the stimulation signal	80
5.14	Trajectories of mean fields and stimulation signal for $\epsilon = 0.075$	81
5.15	Trajectories of mean fields for $\epsilon = 0.675$	82
5.16	Mean field amplitudes with nonlinear delayed feedback from numerical simula- tions with different macroscopic approximations.	83
6.1	Workflow of the online and realtime MEG system	87
6.2	MEG phantom	88
6.3	Online reconstructed current density distribution in a phantom experiment	88
6.4	Glasses for visual stimulation	90
6.5	Linear delayed sensor feedback for one run of visual stimulation	94
6.6	Replay of the linear delayed sensor feedback for one run of visual stimulation . .	94
6.7	Nonlinear delayed sensor feedback for one run of visual stimulation	95
6.8	Replay of the nonlinear delayed sensor feedback for one run of visual stimulation	95
6.9	Time course of the intensities of the stimulation signals during feedback	96
6.10	Averaged power spectral densities for nonlinear delayed voxel feedback and the corresponding replay	97
6.11	Contour maps of the amplitude of the alpha rhythm comparing sensor and voxel feedback	98

List of Tables

3.1	Results of the weighted Minimum Norm methods for single dipole reconstructions	36
3.2	Measures of the single dipole reconstructions for the sLORETA-Laplacian and MFT methods	37
3.3	Measures of the single dipole reconstructions for different regularization procedures	38
3.4	Measures of the reconstructions of configurations I	39
3.5	Measures of the reconstructions of configurations II	40
4.1	Mean localization error of single dipole reconstructions for SOFIA, WROP, and pWROP	55
4.2	Values for the degree of mixing between voxels inside and outside the ROI for different reconstruction methods and settings of their constraint parameter	57
6.1	Displacement results of a phantom experiment	89

Chapter 1

Introduction

Several neurological diseases have in common an abnormal synchronized activity of nerve cells in the brain [TRW⁺98, Tas03, ADTG⁺04]. In order to study brain processes, different techniques are used [OJLSH95]. Functional imaging techniques like *Positron Emission Tomography* (PET), which delivers information about the distribution of radioactively labeled organic molecules, and *functional Magnetic Resonance Tomography* (fMRT) detecting blood oxygenation level dependent changes exhibit spatial resolutions as high as 1 mm. The temporal resolution however is limited to approximately 1 s [BML01].

Complementary non-invasive methods which provide direct information of neural activity are given by electroencephalography (EEG) measuring electrical potential differences and magnetoencephalography (MEG) detecting the magnetic field around the head. The temporal resolution for EEG as well as for MEG is in the millisecond regime. However, the accuracy in localizing the current sources in the brain, which generate the measured signals, is restricted. In MEG the estimated current source distribution is less sensitive to spatial conductivity gradients in the brain tissue [HHR⁺93], which are very difficult to determine. Therefore, concerning the accuracy of the reconstruction MEG is favored versus EEG.

Due to its excellent temporal resolution, MEG is useful for the investigation of synchronization processes in the brain [TFD⁺03]. An *online* tomography of the current density distribution, which provides spatial information about brain activity as accurate as possible, would be of great practical use for experiments in neuroscience and clinical applications. Such a three-dimensional tomography should display the reconstructed current density distribution with respect to the entire source space with a latency of the order of a second after measuring the magnetic fluxes, which is called *online* in this work. The reconstruction should moreover be updated several times per second. Several reconstruction methods are proposed (see [BML01] for a review), but a quantified comparison of techniques applied to MEG which takes into account realistic detector noise is lacking.

Feedback of brain activity is used for the training of *brain computer interfaces* (BCI) (see e.g. [LSH⁺05]). The principal application of a BCI is as a form of neural prosthesis for people suffering from severe paralyzing conditions. *Biofeedback* (or *neurofeedback*) protocols are also applied in behavioral medicine (see e.g. [LHR96, Lub97, Swi96, Tho02]). The patient may acquire an enhanced awareness of the brain processes which underly the disease and learn how to shape them in a desired direction. For these techniques the subject has to

be able and to be willing to control specific brain functions. For the therapy of pathological brain rhythms, novel demand controlled as well as feedback methods have been proposed [Tas01b, Tas01c, Tas01a, Tas02, Tas03, RP04b, PHT05b, THP06]. In contrast to common neurofeedback techniques, these methods are based on physical models of the involved neural ensembles. Therefore these protocols work in an automatized manner in the sense that they do not require the active participation of the subject. Especially the recently introduced nonlinear delayed feedback protocol [PHT05b, PHT05a, PHT06a, THP06] shows a very robust behavior concerning the suppression of rhythms in models of coupled neural oscillators.

To apply such feedback of activity from selective brain regions, several ingredients are necessary. Approaches from different branches of physics are required. First, a reconstruction method is necessary which delivers information about the current density distribution in *realtime*. In this work a reconstruction is considered as being calculated in realtime, if there is a fixed latency as short as possible between measuring the magnetic fluxes and delivering the reconstructed current densities. Moreover the large sampling rate of the MEG and the EEG in the range of kHz should be conserved such that, current density information is available with a sufficiently large temporal resolution. Such a realtime system should also exploit the superior spatial resolution of MEG compared to EEG. For this challenge the biomagnetic inverse problem has to be studied with special regard to the realtime demand. Moreover, the cross-contamination from different brain regions in the reconstructed cerebral currents has to be taken into account. With respect to this problem the physical modeling of the feedback in neural ensembles has to be extended. Finally, the neurofeedback protocols of interest have to be verified experimentally.

This manuscript is organized as follows. In chapter 2 an introduction into MEG and especially into the biomagnetic inverse problem is given. Afterwards a benchmark of reconstruction methods regarding to realtime applications is presented. In chapter 4 a new spatial filter approach is introduced. It is compared to present techniques that try to produce more localized reconstructed current densities with respect to predefined brain regions. In chapter 5 delayed feedback methods are studied in models of coupled oscillators. A modified nonlinear delayed feedback protocol is proposed which exhibits an enhanced desynchronization and decoupling of interacting neural ensembles. This protocol uses constructively the mixing of signals from different brain regions in the reconstructed current densities. The effect is explained and a modeling approach for an analytical understanding is presented. Chapter 6 shows a first application of the implemented realtime MEG system. A healthy subject is visually stimulated with the aid of a linear and a nonlinear delayed neurofeedback protocol, which realizes a regulation of his brain rhythm. Finally, concluding remarks summarize this work and give an outlook.

Chapter 2

Magnetoencephalography

2.1 Basics

Measuring the magnetic field in a non-invasive manner, i.e. outside the body without energy input, is called *magnetoencephalography* (MEG) and *magnetocardiography* (MCG), respectively, in medical imaging. In MEG the aim is to detect signals which originate from currents flowing inside the brain, whereas information about dynamical processes in the heart is of interest in MCG. The signals to be measured are tiny compared to environmental disturbances. In MEG the order of magnitude of magnetic flux densities which are generated by cerebral currents is 100 fT. In contrast the earth magnetic field is of the order of $50 \mu\text{T}$. In normal buildings the magnetic field due to cable currents exhibit flux densities of circa $100 \mu\text{T}$ [D00]. Thus in order to detect biomagnetic signals, a lot of care has to be taken that noise can be reduced effectively and that the sensors provide an excellent sensitivity. In practice *SQUIDs* (Superconducting Quantum Interference Devices) are applied for detection. Usually these SQUIDs are helium-cooled with a working temperature of circa 4 K. If the magnetic flux is coupled into the SQUID via a single coil, the detector is called *magnetometer*. In contrast *gradiometers* measure spatial differences of the magnetic field instead of the magnetic field itself. A first-order gradiometer e.g. consists of two stacked coils, which are linked in a way so that the difference of each measured magnetic flux is coupled into the SQUID. The idea is to reduce spatially homogeneous parts of the magnetic field, for example given by the earth field, during detection. In general gradiometers provide a noise reduction but they exhibit a lowered sensitivity with respect to distant biomagnetic generators. As a further instrument to suppress noise disturbances, MEG measurements are performed in magnetically shielded rooms. For the shielding, materials with large conductivity values are usually used to produce strong eddy currents. Even high-temperature superconductors are applied as a whole-body shielding [MIY92]. An active form of shielding is implemented by coils outside the cabin which produce an opposite field with respect to the noise. For this, the magnetic field of the noise generators is measured by reference coils situated nearby the biomagnetic field generators. A typical value for the white noise of an MEG system in a shielded room is 300 fT [Fie00]. Typical fields evoked by brain activity have a strength of roughly 200 fT. In experiments the signal-to-noise of averaged signals can be improved by an adequate number of trials, i.e. a number of measurements with the same protocol.

The MEG system BTi MAGNES 2500 WH (please see figure 2.1) installed at the Research Centre

Jülich exhibits 148 magnetometers in its helmet. The coils are arranged in a uniformly distributed way with a mean inter-channel distance of 2.9 cm. The shielding of the measurement cabin in



Figure 2.1: Preparation of an MEG experiment in the Research Centre Jülich. The helmet which holds the magnetometers is put on the volunteer's head (right picture). During this measurement the subject is supposed to fulfill arranged tasks with the aid of a small keyboard.

Jülich consists of multiple aluminum layers and layers of ferromagnetic material with high permeability.

Which neuronal processes are responsible for the measured magnetic field being evoked by brain activity? Mainly neurons inside the cortex contribute to these signals. The cortex denotes the 2 – 4 mm thick superficial layer of the brain which is active in many situations like speech processing or sensory stimulation.

In figure 2.2 a sketch of a nerve cell from the cortex is shown. Neurons of this kind are called *pyramidal cells* due to their characteristically shaped cell body. For a single cell a signal, which is coupled into the neuron by synapses, can be defined as time-dependent voltages between the inner and outer of the cell membrane (*membrane potentials*). These signals are received at the dendrites, which refer to the expanded cell branches. The branches extending from the tip of the cell body are called *apical* dendrites, the side dendrites are called *basal*. The dendrites exhibit a mean thickness of $1 \mu\text{m}$ and are branched much more complex than shown in the sketch.

The signals detected by the neuron propagate along the dendrites to the cell body where they can induce *action potentials*. These output signals of the cell spread out along the *axon* where they can serve as input signals for other neurons.

Membrane potentials which differ from their resting values due to signal transmission evoke electrical currents flowing inside the cell, through the cell membrane and moreover in the conducting medium surrounding the neurons. A detectable signal for MEG is produced, if a sufficient number of such currents with a similar orientation (originating from many dendrites and nerve cells, respectively) superimpose. More sophisticated considerations show that in the cortex mainly overlaying currents inside the apical dendrites are responsible for MEG signals [EWRKM83]. These dendrites are arranged perpendicular to the cortex surface. Currents of about 10^6 active dendrites have to superimpose in order to produce a detectable signal of a few fT in MEG [EWRKM83]. This corresponds to a cortex section of the order of 100 mm^2 which has to be active entirely.

[HHR⁺93] gives a more detailed description about the theoretical and instrumental background

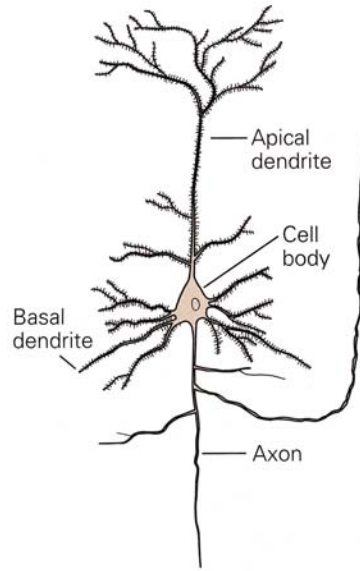


Figure 2.2: Sketch of a pyramidal cell (from: [KSJ00])

in MEG.

2.2 Forward problem

In studies on biomagnetism the forward problem stands for the challenge to give a quantitative description of the evoked magnetic field outside the head, if the underlying current density distribution and the electrical conductivity profile in the brain is given. This challenge has to be solved before the inverse problem can be tackled.

In solving the forward problem the current density $j(\vec{r})$ at each position \vec{r} is usually split into two contributions [D00]:

$$j(\vec{r}) = j^p(\vec{r}) + \sigma(\vec{r})\vec{E}(\vec{r}) \quad (2.1)$$

In this equation $\sigma(\vec{r})$ denotes the electrical conductivity profile in the brain and $j^p(\vec{r})$ is the *primary current density distribution* which macroscopically (cellular details are not taken into account) describes the currents inside the neurons. The term $\sigma(\vec{r})\vec{E}(\vec{r})$ stands for the return currents in the conducting medium surrounding the cells. The dynamics of these currents follow Ohm's law. Thus, from a physiological point of view the interest in the cerebral current density distribution is reduced to the primary current density distribution, because its quantification gives spatial and temporal information about neural activity. As a further assumption the conductivity profile of the brain is modeled as spherically symmetric, i.e. $\sigma(\vec{r}) = \sigma(|\vec{r}|)$. Here the origin of the underlying coordinate system is set to the center of the sphere.

In tomographic views with the aid of other medical imaging techniques, e.g. the functional magnetic resonance tomography (fMRT), there is often focal activity in several distinct areas of the

brain. On a way to an analytical solution, this justifies the simplification that the primary current density distribution can be described as a discretized superposition of focal sources:

$$\vec{j}^p(\vec{r}) = \sum_{i=1}^n \vec{q}_i \delta(\vec{r} - \vec{r}_i) \quad (2.2)$$

The so called *current dipoles* \vec{q}_i (SI-unit: Am) represent the strengths and directions of the point-like sources at positions \vec{r}_i [HHR⁺93]. If it is furthermore assumed that the magnetic permeability inside the brain is equal to the value of free space μ_0 , the *Sarvas-equation* follows which describes the magnetic field outside the volume conductor in quasi-static approximation of the Maxwell equations [Sar87, Fie00]:

$$\vec{B}(\vec{r}) = \frac{\mu_0}{4\pi} \sum_{i=1}^n \frac{F_i \vec{q}_i \times \vec{r}_i - (\vec{q}_i \times \vec{r}_i \cdot \vec{r}) \nabla F_i}{F_i^2} \quad (2.3)$$

whereby

$$F_i = a_i(r a_i + r^2 - \vec{r}_i \cdot \vec{r}) \quad (2.4)$$

and

$$\nabla F_i = (r^{-1} a_i^2 + a^{-1} \vec{a} \cdot \vec{r} + 2a + 2r) \vec{r} - (a + 2r + a^{-1} \vec{a} \cdot \vec{r}) \vec{r}_i \quad (2.5)$$

with $\vec{a} = \vec{r} - \vec{r}_i$, $a = |\vec{a}|$ and $r = |\vec{r}|$. This equation enables the calculation of the magnetic field without explicit knowledge about the conductivity profile $\sigma(r)$. Please note that according to equation 2.3 a radial current dipole, i.e. a dipole \vec{q}_i being parallel to its associated vector \vec{r}_i , does not produce a magnetic field outside the volume conductor. Thus, in this model it represents an example for a *silent* source which cannot be detected with an MEG sensor outlined above.

2.3 Lead fields

By usage of the Sarvas-equation 2.3 the linear mapping between the predicted magnetic flux m_i in each sensor i and the underlying primary current density distribution $j^p(\vec{r})$ can be determined [HHR⁺93]. This delivers vector fields $\vec{\Phi}_i(\vec{r})$ (*lead fields*) which describe the sensitivity of each sensor including its geometry for every source location \vec{r} . With knowledge about the lead fields, the expected detector signals can be determined by integration over the source space S :

$$m_i = \int_S \vec{\Phi}_i(\vec{r}) \cdot \vec{j}^p(\vec{r}) d^3 r \quad (2.6)$$

Modeling $\vec{j}^p(\vec{r})$ as a superposition of n current dipoles (equation 2.2) the magnetic fluxes are obtained by $m_i = \sum_{k=1}^n \vec{\Phi}_i(\vec{r}_k) \cdot \vec{q}_k$. If the source space is furthermore discretized into a source space grid with N_s volume elements, the average primary current density \vec{j}_k^p in voxel V_k is intertwined with the current dipole in this voxel by:

$$\vec{q}_k = \vec{j}_k^p \Delta V_k \quad (2.7)$$

With this the interrelation between the magnetic fluxes through the sensors and the primary current density distribution can be described in a matrix notation as:

$$\vec{m} = \Phi \vec{j}^p \quad (2.8)$$

The vector \vec{m} (dimension: number of detectors N_d) is built by the fluxes m_i in the sensors. Each current density \vec{j}_k^p for voxel k gives three components of the vector \vec{j}^p (dimension: $3 \cdot N_s$). Vector \vec{j}^p is ordered in blocks for each voxel so that all three spatial components of the current density in a specific voxel appear directly one after the other, i.e. $\vec{j}^p = (\dots, j_k^{p,x}, j_k^{p,y}, j_k^{p,z}, \dots)^T$ (T : transposed). The lead field matrix Φ (dimension: $N_d \times (3 \cdot N_s)$) consists of the discretized lead fields of the detectors times the size of the volume elements. It is defined by the chosen forward model. In the following the index p in \vec{j}^p is dropped and current density distribution is used synonymously for primary current density distribution, because this is the distribution of interest which determines the magnetic fluxes.

2.4 Biomagnetic inverse problem

In reconstructing the current density distribution from the measured magnetic field, fundamental difficulties and approaches for their solution are discussed in the next sections.

2.4.1 Ill-posed problem

The aim of MEG reconstruction methods is to obtain the underlying current density distribution inside the brain from the measured signals:

$$\vec{m} = \Phi \vec{j} + \vec{n} \quad (2.9)$$

In this equation the vector \vec{n} stands for the noisy contributions that each detector picks up in practice. The inverse problem means the search for the inverse matrix Φ . Already 1853 Helmholtz however has been able to prove that it is impossible to reconstruct the current density distribution inside a 3-dimensional volume conductor from a given field even with an infinite number of detectors outside the conductor [Hel53]. Moreover the number of grid points (center of each volume element) N_s inside the source space is usually much larger than the number of applied detectors N_d so that the inverse matrix Φ^{-1} is not defined irrespectively of the choice of the forward model. Thus the MEG inverse problem belongs to the class of *ill-posed* problems [FB05].

What makes things even more difficult is the fact that a *singular value decomposition* (SVD) of Φ gives very small singular values, which can result in drastic errors in estimating \vec{j} especially in the presence of detector noise [FB05]. Here a singular value has to be considered as very small, if after normalization by the largest singular value it is of the same order of magnitude as the applied floating point number accuracy [PTVF92]. The physical reason for the tiny singular values is given by the large spatial overlap of the lead fields which results in an approximately linear relationship of rows in matrix Φ [HI94].

The concrete shape of current source configurations which are difficult to reconstruct depends on the chosen forward model. An example for a source which cannot be detected at all with the

applied model of a spherically symmetric volume conductor is a radial current dipole. Any number of such silent sources could be added to a current density distribution \vec{j} without changing the resulting magnetic field \vec{m} . Each of these current density distributions would be equivalent with respect to their evoked MEG signals, if no further assumptions were made.

Accordingly, different *a priori* assumptions have led to a number of different approaches to find algorithms which uniquely describe the estimated current source distribution. Beamformer methods like linearly constrained minimum variance spatial filtering (LCMV [vVvDYS97]) and multiple signal classification [MLL92], which originated from radar and sonar signal processing, filter activity at each grid position in the source space with the aid of the covariance of the data. This reconstruction approach assumes that the underlying current densities between different voxels are uncorrelated. In the Bayesian approach *a priori* information, e.g. from fMRT, is incorporated in the reconstruction algorithm favoring specific current source distributions [BML01]. Parametric modeling like the spatiotemporal multiple source analysis technique [SvC86] handles the non-uniqueness of the inverse problem by allowing only a fixed number of active current sources in order to make the inverse problem overdetermined.

Because of the fact that this number cannot be determined *a priori* [MML⁺04], methods that do not need this assumption have received growing attention [IBC90, HI94, TYY⁺99, PM99a, dPMA00a, PM02, MML⁺04, WFK04, SLRH05]. In these *distributed source models* the number of simultaneously active sources is only bound by the number of points in the source space grid. Due to the underdetermined nature of the biomagnetic inverse problem, algorithms following this approach produce solutions with relatively low resolution. From the point of view of real-time applications studied however, distributed source models have the additional advantage of providing a linear mapping between the measured signals and the estimated current density distributions under certain circumstances described in chapter 3. This allows a very fast calculation of the cerebral currents making it possible to implement a neurofeedback system. In contrast beamformer algorithms e.g. require information about the covariance of the signals which hinders to estimate the current density distributions in real-time; Multiple-dipole models require a time-consuming iterative algorithm in order to find a current dipole configuration which best describes the signals. The regularization process which all distributed source models have in common will be described in the next section.

2.4.2 Tikhonov regularization

An obvious measure for the quality of a current density reconstruction \vec{j} is the euclidian distance

$$D(\vec{j}) = |\vec{m} - \Phi \vec{j}| \quad (2.10)$$

between the given signal \vec{m} and a simulated signal which is determined by the forward solution of the reconstructed current density distribution \vec{j} . As already explained, this measure on its own is not sufficient to describe \vec{j} uniquely because any current density distribution \vec{j}^k being situated in the kernel of matrix Φ could be added to \vec{j} without changing the value of D . An additional criterion for the goodness of the solution is therefore introduced by

$$\Omega(\vec{j}) = |L\vec{j}| \quad (2.11)$$

with a so far arbitrarily chosen *weighting matrix* L (dimension: $N_d \times (3 \cdot N_s)$). It will be specified in the next chapter. An appropriate matrix L together with an adequate setting of the regularization parameter α results in a unique description of the estimated current density distribution \vec{j} which has to minimize the weighted sum of D and Ω :

$$\vec{j} = \operatorname{argmin}\{\alpha|\vec{L}\vec{j}|^2 + |\vec{m} - \Phi\vec{j}|^2\} \quad (2.12)$$

This minimization ansatz, in finding a unique solution by a tradeoff between criteria 2.10 and 2.12, is the widely used *Tikhonov regularization* [FB05, PM02, PMML94, TBAVVS04, GA99]. The degree of the tradeoff is tuned via the regularization parameter α . For the minimum it follows:

$$\begin{aligned} & \frac{\partial}{\partial j_i} (\alpha \vec{j}^T L^T L \vec{j} + (\vec{m} - \Phi \vec{j})^T (\vec{m} - \Phi \vec{j})) &= 0 \\ \Rightarrow & \frac{\partial}{\partial j_i} (\alpha \vec{j}^T L^T L \vec{j} + \vec{m}^T \vec{m} - \vec{j}^T \Phi^T \vec{m} - \vec{m}^T \Phi \vec{j} + \vec{j}^T \Phi^T \Phi \vec{j}) &= 0 \\ \Rightarrow & \frac{\partial}{\partial j_i} (\alpha \sum_{k=1}^{3 \cdot N_s} j_k (\sum_{l=1}^{3 \cdot N_s} (L^T L)_{kl} j_l) - \frac{\partial}{\partial j_i} \sum_{k=1}^{3 \cdot N_s} j_k (\Phi^T \vec{m})_k \\ & - \frac{\partial}{\partial j_i} \sum_{k=1}^{N_d} m_k (\sum_{l=1}^{3 \cdot N_s} \Phi_{kl} j_l) + \frac{\partial}{\partial j_i} (\sum_{k=1}^{3 \cdot N_s} j_k (\sum_{l=1}^{3 \cdot N_s} (\Phi^T \Phi)_{kl} j_l)) &= 0 \\ \Rightarrow & \alpha \sum_{k,l=1}^{3 \cdot N_s} (\delta_{ik} (L^T L)_{kl} j_l + \delta_{il} (L^T L)_{kl} j_k) - (\Phi^T \vec{m})_i - \sum_{k=1}^{N_d} m_k \Phi_{ki} \\ & + \sum_{k,l=1}^{3 \cdot N_s} (\delta_{ik} (\Phi^T \Phi)_{kl} j_l + \delta_{il} (\Phi^T \Phi)_{kl} j_k) &= 0 \\ \Rightarrow & 2\alpha \sum_{k=1}^{3 \cdot N_s} (L^T L)_{ik} j_k - 2(\Phi^T \vec{m})_i + 2 \sum_{k=1}^{3 \cdot N_s} (\Phi^T \Phi)_{ik} j_k &= 0 \\ \Rightarrow & 2(\alpha L^T L + \Phi^T \Phi) \vec{j} &= 2\Phi^T \vec{m} \end{aligned}$$

Thus, the current density distribution is determined by

$$\vec{j} = (\alpha L^T L + \Phi^T \Phi)^{-1} \Phi^T \vec{m} \quad (2.13)$$

or equivalently (see appendix A):

$$\vec{j} = (L^T L)^{-1} \Phi^T (\Phi (L^T L)^{-1} \Phi^T + \alpha 1)^{-1} \vec{m} \quad (2.14)$$

Usually formula 2.14 is more useful: The number of components in matrix $(\Phi (L^T L)^{-1} \Phi^T + \alpha 1)^{-1}$ in equation 2.14 is significantly smaller than those in the inverse matrix in equation 2.13 ($N_d \times N_d$ compared to $(3 \cdot N_s) \times (3 \cdot N_s)$). Moreover the inverse matrix $(L^T L)^{-1}$ can be calculated easily, if, for example, L is a diagonal matrix with diagonal elements unequal to 0.

In the solution for \vec{j} with the aid of the Tikhonov regularization the role of α becomes evident: For $\alpha = 0$ the approach would reduce to the minimization of D (see equation 2.10) without getting rid of the difficulties of the ill-posed problem. A regularization parameter $\alpha > 0$ however increases the range of the matrix which has to be inverted. This is shown explicitly in the following description of the SVD, which can be used for the calculation of inverse matrices.

2.4.3 Singular value decomposition

The following theorem from linear algebra helps to calculate the inverse of a matrix with dimension $M \times N$ ([PTVF92] [FB05]): Each matrix A whose number of rows M is larger or equal than

its number of columns N can be written as the product of a matrix U (dimension: $M \times N$) with orthonormal columns, a diagonal matrix W (dimension: $N \times N$) and a matrix with orthonormal rows V (dimension: $N \times N$):

$$A = UWV \quad \text{with} \quad UU^T = 1 \quad \text{and} \quad VV^T = 1 \quad (2.15)$$

This decomposition is unique except for a permutation of the column vectors in matrix U (and an corresponding permutation of the diagonal elements w_i in matrix W and the row vectors in matrix V , respectively) as well as for a linear combination of column vectors in matrix U (and corresponding linear combinations of row vectors in V) whose associated diagonal elements in W are equal. In section 2.4.2 (equation 2.14) the matrix $P = C + \alpha 1 = \Phi(L^T L)^{-1} \Phi^T + \alpha 1$, which has to be inverted, is square. In this case it holds $V = U^T$ in the SVD of $C = UQV$ [FB05] and furthermore:

$$\begin{aligned} P^{-1} &= (C + \alpha 1)^{-1} \\ \Rightarrow &= (UQU^T + \alpha 1)^{-1} \\ \Rightarrow &= (U(Q + \alpha 1)U^T)^{-1} \\ \Rightarrow &= U(Q + \alpha 1)^{-1}U^T \\ \Rightarrow P_{ij}^{-1} &= \sum_{k=1}^{N_d} U_{ik}((Q + \alpha 1)^{-1}U^T)_{kj} \\ \Rightarrow &= \sum_{k=1}^{N_d} U_{ik} \sum_l (Q + \alpha 1)^{-1}_{kl} U_{lj}^T \\ \Rightarrow &= \sum_{k=1}^{N_d} \frac{U_{ik}U_{kj}^T}{q_k + \alpha} \\ \Rightarrow &= \sum_{k=1}^{N_d} \frac{U_{ik}U_{jk}}{q_k + \alpha} \end{aligned}$$

It is $q_k \geq 0$ for all k . If the regularization parameter α is chosen larger than 0, the matrix P^{-1} is also well-defined in case of $q_k = 0$ for some k . Alternatively to regularization with the aid of the parameter α , the influence of diagonal elements q_i which are 0 or close to 0 (and therefore falsified due to rounding errors after numerical calculation) can be removed by a restricted summation in the determination of P_{ij}^{-1} . For this in

$$P_{ij}^{-1} = \sum_{k=1}^{N_s} \frac{U_{ik}U_{jk}}{q_k + \alpha} \quad (2.16)$$

the parameter α is set to 0 and the maximal summation index is set to a value $\tilde{k} \leq N_m$ [PTVF92][FB05][HI94]. Here the diagonal elements q_k are supposed to be ordered descendently. The *truncating parameter* \tilde{k} is the regularizing variable in this alternative regularization process. Thus the components of P^{-1} are now given by:

$$P_{ij}^{-1} = \sum_{k=1}^{\tilde{k}} \frac{U_{ik}U_{jk}}{q_k} \quad (2.17)$$

2.4.4 Cross-validation

A method which tries to find an optimal value for α in equation 2.14 with respect to a specific data vector \vec{m} in an automatized way is given by the cross-validation algorithm [PM99a]. The components m_i of \vec{m} are given by the outputs of each detector i . The cross-validation error is defined as

$$CVE(\alpha) = \frac{1}{N_d} \sum_{i=1}^{N_d} (m_i - (\Phi_{\vec{j}_{[i]}})_i)^2 \quad (2.18)$$

where $(\Phi_{\vec{j}_{[i]}})_i$ is component i of vector $\Phi_{\vec{j}_{[i]}}$ and

$$\vec{j}_{[i]} = (L^T L)^{-1} \Phi_{[i]}^T (\Phi_{[i]} (L^T L)^{-1} \Phi_{[i]}^T + \alpha 1)^{-1} \vec{m}_{[i]} \quad (2.19)$$

with a dimension of $3 \times N_s$. Matrix $\Phi_{[i]}$ (dimension: $(N_d - 1) \times (3 \times N_g)$) is obtained from matrix Φ by removing its i th row and vector $\vec{m}_{[i]}$ (dimension: $N_d - 1$) is \vec{m} without component i .

In other words, the cross-validation error defined in equation 2.18 measures the mean squared difference between the actual output of the i th detector and the predicted output of detector i by a reconstructing including the signals of all other detectors. The resulting value of α after cross-validation is given by taking the derivative of $CVE(\alpha)$ with respect to α and setting it to zero.

With cross-validation there is no linear mapping between the signals and the estimated current density distribution because the parameter α used in equation 2.14 depends on the data vector \vec{m} and is different for each time slice. Therefore, this automatized regularization technique is not suitable for the real-time MEG system presented in chapter 6, if the cross-validation is performed for each \vec{m} independently.

After presenting different regularization strategies, the constraint on the solutions given by the weighting matrix L will be further explained. It will be shown that this constraint can also be interpreted as an assumption on the current density distributions to be estimated. This insight helps to motivate choices for L discussed in the next chapter.

2.4.5 Assumptions in distributed source models

The estimated current density distributions depend crucially on the choice of the weighting matrix L . In a statistical description of the Tikhonov regularization the role of matrix L becomes more evident.

Here the inverse problem

$$\vec{m} = \Phi \vec{j} + \vec{n} \quad (2.20)$$

to reconstruct the original current density distribution from the measured magnetic fluxes \vec{m} takes place in the presence of detector noise \vec{n} . This noise is assumed to be Gaussian distributed with mean 0 and a covariance matrix Γ . Thus the probability density function of the noise vector \vec{n} is determined by (please see also appendix B)

$$p(\vec{n}) = \mathcal{N} e^{-\frac{1}{2}(\vec{n}^T \Gamma^{-1} \vec{n})} \quad (2.21)$$

with an appropriate normalization factor \mathcal{N} . Let us further assume that $\Gamma = \sigma^2 \mathbf{1}$ and that the *a priori* probability density function for the original current density distribution is given by

$$p(\vec{j}) = \mathcal{M} e^{-\frac{1}{2}(\vec{j}^T Z^{-1} \vec{j})} \quad (2.22)$$

with a further normalization factor \mathcal{M} . The covariance of this probability density function is described by matrix Z . Any *a priori* knowledge about the underlying current density distribution besides the signals \vec{m} can be incorporated in this matrix.

It can be shown [FB05] that with these assumptions the minimization condition for \vec{j} according to the Tikhonov regularization is equivalent to the maximization of the *a posteriori* probability density function $p(\vec{j}|\vec{m})$. This function describes the probability of \vec{j} for a given data vector \vec{m} . The equivalence holds, if the covariance matrix Z in equation 2.22 and the weighting matrix L in equation 2.12 are connected by [FB05]

$$L^T L = Z^{-1} \quad (2.23)$$

Summarizing what the Tikhonov regularization does from a statistical point of view is providing that current density distribution which is most probable for the given data vector \vec{m} and for the predefined *a priori* probability density function of \vec{j} in equation 2.22. Here the noise picked up by the detectors is supposed to be Gaussian distributed. The *a priori* probability density function for \vec{j} is related to the weighting matrix L in the Tikhonov regularization by formula 2.23.

In the following chapter, specific distributed source models are investigated with respect to their reconstruction accuracy.

Chapter 3

Comparative study of inverse methods

When searching for a method that should provide information about the current density distribution in the human brain in realtime, decisive criteria are the required computation time and the goodness of the delivered reconstruction. Several distributed source models are candidates for the desired realtime algorithm due to their relatively small computational costs as will be explained. Furthermore quantitative knowledge about the accuracy of these methods is of considerable interest in order to evaluate the significance of the localization of reconstructed current generators from experimental data.

In this chapter a study of distributed source models will be presented based on numerical experiments. The discussed simulations rely are based on a setup taken from a real MEG experiment which has been performed at the Research Centre Jülich. The method presented first will be the *Minimum Norm* (MN) algorithm introduced by Hämäläinen et al. in 1994. Extending the MN, several *weighted Minimum Norm* methods have been developed like the *lead field normalized Minimum Norm* (lFMN [FWKW99]) approach also tested here and the *Gaussian weighted Minimum Norm* algorithm studied for the first time in this work. Furthermore the recently established *standardized Low Resolution Brain Electromagnetic Tomography* [PMML94, PM99a, FWKW99, dPMA00a, PM02, WFK04] will be included in the benchmark. This technique has already been investigated in *electroencephalography* (EEG) with the aid of numerical simulations [PM02, WFK04] but not in an MEG framework.

The inverse methods named so far are suited for realtime applications and produce a linear mapping between the magnetic fluxes and their associated reconstructed current density distributions, if an appropriate regularization is performed. In contrast the multi-step *Magnetic Field Tomography* (MFT) cannot be implemented in the realtime MEG system presented in chapter 6 due to its large computational costs. In many off-line MEG surveys however the MFT has been applied (e.g. [IBC90, TIV01, MLC⁺03, TFD⁺03, BAD⁺05]). Therefore a comparison with linear methods is interesting and important. In this work the MFT is compared for the first time to the algorithms mentioned above. The crucial influence of the concrete regularization on the estimated current density distributions will also be investigated. For this the strategies presented in the preceding chapter to handle this unsolved problem [BML01] will be evaluated.

In sections 3.1.1 to 3.1.3 the investigated algorithms will be presented. Afterwards the configurations of the numerical experiments are described. The chapter ends with the results of the simulations and a discussion about the quantified goodnesses of the reconstruction methods and

the tested regularization techniques.

3.1 Tested distributed source models

3.1.1 Weighted Minimum Norm methods

In the classical MN algorithm, the matrix L is set to 1 in equation 2.12. It is well-known [PM02, FWKW99, WFK04] that for sources located deeper in source space, the applied method gives a reconstruction which is too superficial. The reason for this is that in equation 2.12 the term $|\vec{m} - \Phi \vec{j}|^2$ can give similar values for deeper and more superficial situated current sources. The latter are relatively smaller concerning their amplitude. Because of this the second term $|L \vec{j}|^2$ favors the superficial solution for $L = 1$.

From a statistical point of view (section 2.4.5) the reciprocals of the diagonal components L_{kk} of matrix L determine the *a priori* probability of current density at index k , if L is a diagonal matrix. An extension of MN (see e.g. [FWKW99]) is therefore given by defining L in a way that helps recovering deeper sources by increasing their *a priori* probability. In the following descriptions of weighted Minimum Norm methods as well as the Magnetic Field Tomography, L is defined as a diagonal matrix and the same *a priori* probability is set for all three components of the current density belonging to the same grid point i . This means that for $0 \leq i < N_s$ it holds

$$L_{i \times 3, i \times 3} = L_{i \times 3+1, i \times 3+1} = L_{i \times 3+2, i \times 3+2} =: \mathcal{L}_{ii} \quad (3.1)$$

Thus, in this case the definition of matrix \mathcal{L} (dimension: $N_s \times N_s$) determines all components of matrix L which is then applied to perform the reconstruction.

In order to quantify the entries of \mathcal{L} in a weighted Minimum Norm method, a natural approach is given by a weighting at each grid position which corresponds to the mean lead field strength in the associated voxel. This means defining \mathcal{L} by [FWKW99]

$$\mathcal{L}_{ij} = \delta_{ij} \frac{\sum_{k=1}^{N_d} |\vec{\Phi}_{ki}|^p}{N_d} \quad (3.2)$$

with N_d representing the number of applied detectors and $p = 1$. In equation 3.2, $\vec{\Phi}_{ki}$ is a three-dimensional vector built by those components in the lead field matrix Φ which describe the sensitivity of detector k to a unit dipole source in x -, y -, or z -direction, respectively, at grid position i ($\delta_{ij} = 1$ for $i = j$, otherwise $\delta_{ij} = 0$). In order to not overemphasize deep sources, values of \mathcal{L}_{ij}^{-1} which are larger than a regularizing threshold value according to equation (3.2) have been set to the threshold value. The specific value of the threshold had been optimized with respect to the mean localization error over dipoles at each grid position in x -, y -, and z -direction in preliminary noiseless simulations as well as choosing p equal to 1 in equation (3.2). For normalization the components \mathcal{L}_{ij}^{-1} had been divided by their maximum. The reconstruction method with a matrix L defined that way will be called *lead field Normalized Minimum Norm* (lfMN) in the following (see also figure 3.1).

As an alternative *a priori* probability function, in this work a Gaussian profile (see figure 3.1) will be tested, motivated by its successful application in MFT ([TIMG99]). In this case the matrix

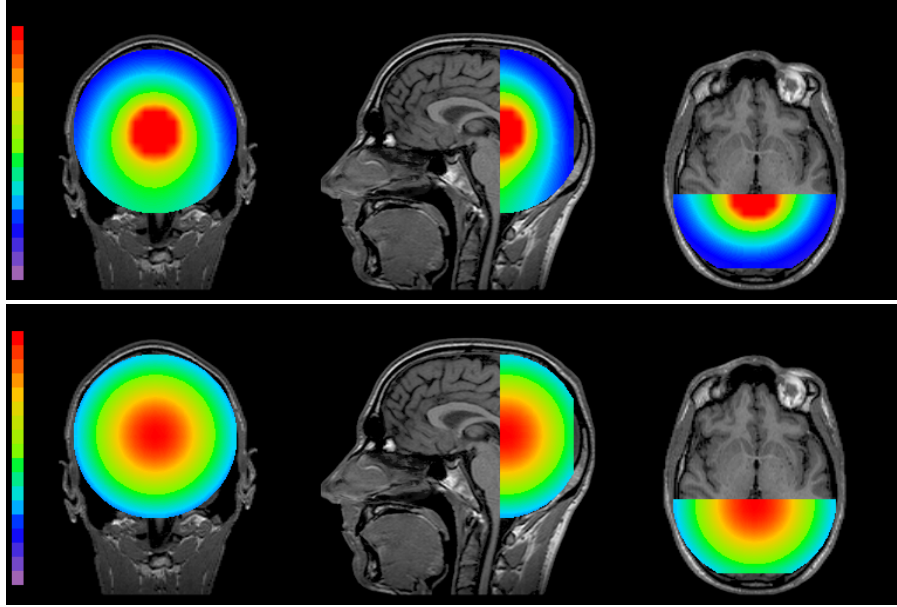


Figure 3.1: Color coded values for \mathcal{L}_{ii}^{-1} in dependence of grid position i for the lfMN (top) and the GaussMN reconstruction method (bottom). The source space grid, which is underlying the interpolated weighting profile shown in this figure, has been constructed from a spherical segment fitted to the back of the head. The joint intersection point of the presented slices is $[-3.9 \text{ cm}, 0 \text{ cm}, 1.5 \text{ cm}]$. Values range from 0 to 1 where purple indicates the smallest and red the largest values (linear scaling).

\mathcal{L} and L , respectively, are defined by:

$$\mathcal{L}_{ij} = \delta_{ij} \exp\left(\frac{1}{2} \left(\frac{y_i^2 + z_i^2}{\lambda_{y,z}^2} + \frac{x_i^2}{\lambda_x^2} \right)\right) \quad (3.3)$$

Here $\lambda_{y,z}$ and λ_x are fitted decay parameters whereas x_i , y_i , and z_i are the coordinates of the position of point i in the grid. The associated reconstruction method will be denoted as *GaussMN* in this work.

3.1.2 sLORETA

In the absence of noise the solution of the Tikhonov regularization (see equations 2.9 through 2.13) can be written as:

$$\vec{j} = (\alpha L^T L + \Phi^T \Phi)^{-1} \Phi^T \Phi \vec{j}_{\text{Orig}} \quad (3.4)$$

This describes explicitly the mapping between the original current density distribution \vec{j}_{Orig} and the reconstructed current density \vec{j} . The square matrix

$$R = (\alpha L^T L + \Phi^T \Phi)^{-1} \Phi^T \Phi \quad (3.5)$$

is called the *resolution matrix* [dPMHA⁺97] (dimension: $(3 \cdot N_s) \times (3 \cdot N_s)$). The key idea in sLORETA is to modify the solution of the Tikhonov regularization by applying

$$\vec{j}_{\text{sLOR,k}} = R_k^{-\frac{1}{2}} \vec{j}_k \quad (3.6)$$

which estimates the current density distribution in form of a statistical map [PM02]. The index k in the current density distributions denotes again that $\vec{j}_{\text{sLOR},k}$ describes the sLORETA solution of the current density at grid position k . Analogous, \vec{j}_k is given by those components of \vec{j} which describe the current density at point k according to equation 3.4. Thus $\vec{j}_{\text{sLOR},k}$ and \vec{j}_k themselves just hold 3 components for each k . Analogous R_k refers to that 3×3 -section in the resolution matrix which links the original current density distribution at position k to the reconstructed current density distribution at position k .

The weighting matrix L was set to the unity matrix (uniform depth weighting) in the introduction of sLORETA, which produces a localization error of 0 with an appropriate regularization in the absence of detector noise [GOP05]. In a more general framework however it can be set to other values [PM02] analogous to the weighted Minimum Norm methods. In this work the Laplacian Matrix $L = \Delta$ is chosen motivated by the *Low Resolution Electromagnetic Tomography* (LORETA [PMML94]), because it gave better results than $L = 1$ (not shown here) in the presence of detector noise. This specific sLORETA version will be called sLORETA-Laplacian in the following. As can be deduced from equation 2.12, the choice of the Laplacian matrix for L produces a constraint on \vec{j} which prefers solutions with small values concerning its spatial gradients (see appendix C).

3.1.3 MFT

In contrast to the other reconstruction routines described so far, MFT is a multi-step and non-linear method (please see also [IBC90]), in order to refine the estimated current density distribution in each calculation step. In the following its algorithm will be described whereby all matrices, vectors, and scalars, which refer to the n -th step, are indexed with n .

In the solution for its n -th iteration ($n \geq 1$)

$$\vec{j}^n = ((L^n)^T L^n)^{-1} \Phi^T (\tilde{P}^n)^{-1} \tilde{m}^n \quad (3.7)$$

the associated weighting matrix \mathcal{L}^n (section 3.1.1) is defined by

$$\mathcal{L}_{kl}^n = |\vec{j}_k^{n-1}|^{-\frac{1}{2}} \mathcal{L}_{kl}^0 \quad (3.8)$$

in order to produce more focal solutions [IBC90]. This definition delivers also

$$L_{i \times 3, i \times 3}^n = L_{i \times 3+1, i \times 3+1}^n = L_{i \times 3+2, i \times 3+2}^n = \mathcal{L}_{ii}^n \quad (3.9)$$

for each grid position i . The 3-dimensional vector \vec{j}_k^{n-1} describes the estimated current density after step $n - 1$ at grid position k . The starting condition of the iteration procedure is given by

$$\mathcal{L}_{ij}^0 = \delta_{ij} \exp\left(\frac{1}{2} \left(\frac{y_i^2 + z_i^2}{\lambda_{y,z}^2} + \frac{x_i^2}{\lambda_x^2} \right)\right) \quad (3.10)$$

and

$$|\vec{j}_k^0| = 1 \quad (3.11)$$

for all k . Moreover according to [IBC90], \tilde{m} and \tilde{P} are set to

$$\tilde{m}^n = \Phi((L^n)^T L^n)^{-1} \Phi^T \vec{m} \quad (3.12)$$

and, respectively,

$$\tilde{P}^n = (\Phi((L^n)^T L^n)^{-1} \Phi^T + \alpha_n \mathbf{1}) \Phi((L^n)^T L^n)^{-1} \Phi^T \quad (3.13)$$

with a regularization parameter α_n which is defined by

$$\alpha_n = \frac{\text{tr}(\Phi((L^n)^T L^n)^{-1} \Phi^T)}{N_d} \zeta \quad (3.14)$$

Here ζ stands for a fitting parameter.

In [IBC90] no criterion is given about the choice of the number of iteration steps. In practice, MFT is usually used with two iterations, i.e. $n = 2$ (see e.g. [TIMG99, TFD⁺03, DI00]), which has been followed in this study.

3.2 Setup of the simulations

3.2.1 Configuration of the source space and the sensors

The simulations discussed in this work are based on a setup taken from an MEG experiment with visual stimulation. A setup has been chosen which is similar to common studies involving MFT [TIMG99, TFD⁺03, TIV01, Dam00, MLC⁺03]. This implies that only those $N_d = 90$ detectors are used which are located in the back of the helmet. Furthermore the source space containing the

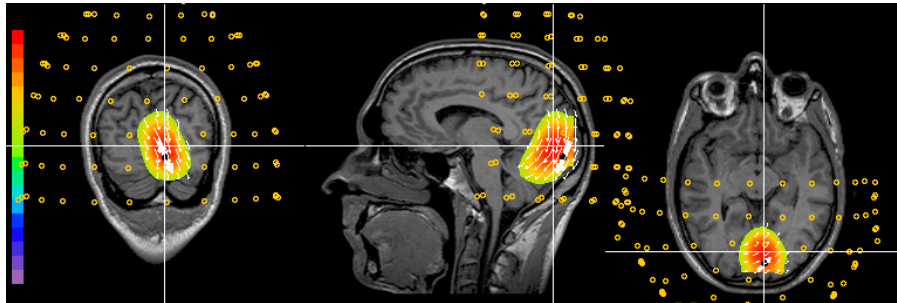


Figure 3.2: Exemplary reconstruction of a current dipole situated in the area V1 of the visual cortex: The orientation and the modulus (a.u.) of the reconstructed current density distribution are shown with the cursor at the maximum, along with the positions of the 90 applied detectors (indicated by the small orange circles around the head). GaussMN is used here for the reconstruction. Activity is shown only at positions where the modulus of the current density is equal to or larger than 60% of the maximum activity in the reconstructed current density distribution.

current density distribution was modeled as a segment of a sphere fitted to the back of the brain. The source space is embedded in a regular display grid with $17 \times 17 \times 9$ grid points.

The positive x -axis of the underlying coordinate system extends from the center of the head to the nose, the positive z -axis leads to the top of the head being perpendicular to the line between the left and right ears (defining the direction of the y -axis), and the positive y -axis points to the left side of the head. In the applied setup the minimum distance of grid points has been 7.8 mm in the x -direction and 8.7 mm in the y -direction as well as in the z -direction, whereby $N_s = 1281$ of the total amount of 2601 display grid points are located inside the spheric segment. Considering

the fact that a cortex section of approximately 100 mm^2 has to be active entirely to generate a detectable MEG signal, the chosen grid density is not considerably undersized.

3.2.2 Simulated detector signals

In order to investigate the accuracy of the reconstruction of the methods, current dipoles have been situated on the source space grid points (figure 3.2). Different dipole orientations have been investigated but the radial component has been removed before calculating the forward solutions for each configuration, because these components represent silent sources in the forward model used here. Moreover, the strength of the dipoles has always been set to 1 (a.u.) after removing the radial component.

In order to simulate detector noise, the standard deviation of the distribution of the detector outputs σ_{sign} has been determined for each dipole configuration after calculation of the forward solution. For a given value of the signal-to-noise-ratio (SNR), the standard deviation of the Gaussian distributed noise σ_{noise} is calculated, which has mean zero, according to

$$SNR = \frac{\sigma_{sign}}{\sigma_{noise}} \quad (3.15)$$

From the resulting Gaussian distribution randomly chosen values are added to the forward solution. For single dipole reconstructions noise levels with $SNR = 1$ and $SNR = 2$ are tested which correspond to experimental conditions [Dam00]. An alternative way to define the signal-to-noise-ratio is by taking the maximum signal among all detectors in the above formula for SNR instead of σ_{sign} [IBC90]. For the same detector signals and the same values of σ_{noise} the two definitions lead to significantly different values. Tests have shown that under these conditions the signal-to-noise-ratio defined in the alternative manner is approximately three times larger compared to the SNR via definition 3.15 applied in this work.

In noise simulations 300 noise realizations are used to calculate the mean and standard error of the mean for the measures which will be described in the following.

3.2.3 Measures to quantify the reconstruction performance

For single dipole reconstructions the *displacement* (or *localization error*) is defined as the distance between the original dipole position and the position of maximum activity, i.e. the position of the reconstructed current density vector with the largest modulus.

To measure the accuracy of estimating the orientation of current dipoles the *angle difference* between the original one and the current density vector at the position of maximum activity in the reconstructed distribution is calculated.

Moreover, it has been investigated how blurred the reconstructed current densities have been. For this, the number of voxels has been counted whose associated activity has been larger than a threshold activity. For single dipole simulations 60 percent of the maximum activity in the reconstructed current density distribution has been chosen as the threshold. This corresponding volume will be called *volume of activity*. To account for very deformed current density reconstructions, the *spreading* is defined as the maximal distance of the voxels in the volume of activity to the position of the original dipole.

3.2.4 Defining subregions in the source space

The quality of the reconstruction of current dipoles is strongly dependent on their relative positions to the sensors because of the spatial distribution of their sensitivity profiles [PMML94, FWKW99, dPMA00b]. Thus, for single dipole reconstructions tomographic figures of the measures in the source space will be shown. Additionally, averaged values are given with respect to the total source space and subregions defined in the following way: first (see also equation 3.2)

$$l_{\max} = \max_i \left(\frac{\sum_{k=1}^{N_d} |\vec{\Phi}_{ki}|}{N_d} \right) \quad (3.16)$$

represents the maximal lead field strength in the source space grid averaged over all detectors. Current dipoles are then defined as *deep*, if their associated grid position i shows a lead field strength \mathcal{L}_{ii} (equation 3.2) which is smaller or equal than $\frac{1}{3}l_{\max}$. A midrange region is defined by positions i with $\frac{1}{3}l_{\max} < \mathcal{L}_{ii} \leq \frac{2}{3}l_{\max}$. Finally, the remaining positions in the source space are associated to superficial dipoles according to this division (see also figure 3.3).

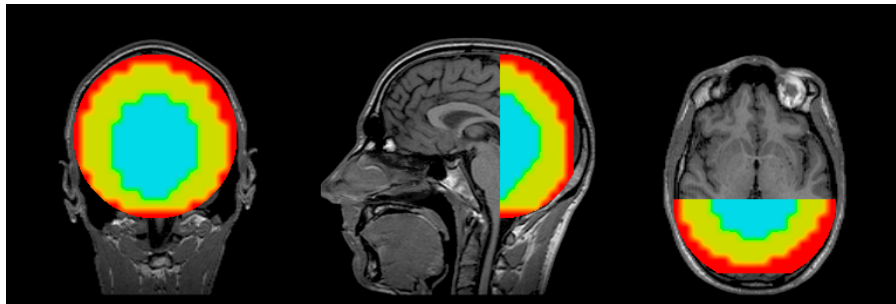


Figure 3.3: In order to give averaged measures characterizing similar current dipole positions with respect to lead field strength, the source space is divided into three regions: deep (blue), midrange (yellow) and superficial region (red). The joint intersection point of the presented slices is $[-3.9 \text{ cm}, 0 \text{ cm}, 1.5 \text{ cm}]$.

To give an impression about the anatomical division by the subregions, cytoarchitectonic probability maps (see [ZSPGA02]) show that in this head-sensor configuration the area V5 of the visual cortex area is situated in the boundary regime of the superficial and the midrange region, whereas V1 is distributed across all three regions (17 percent deep, 61 percent midrange, and 22 percent in the superficial region with a 50 percent probability setting of the brain map).

3.2.5 Two-dipole configurations

In order to perform a quantitative analysis with the defined measures also for two-dipole configurations, first threshold activities in the reconstructed current density distribution are looked for which produce two separated regions of activity. If such a threshold (in simulations with detector noise in at least 60 percent of the noise realizations) cannot be found, this specific configuration is considered as not resolved. Otherwise the coherent region of activity which holds the absolute maximum activity in the reconstructed current density reconstruction is attached to the original dipole which is nearest to the absolute maximum. In this way the defined measures can still be

applied to both original dipoles and their corresponding regions of activities. Because the values of the volume of activity as well as the spreading are very sensitive to the used threshold, their analysis is omitted in two-dipole configurations. In addition to the localization error and angle difference the relative strength of the reconstructed dipoles, i.e. the ratio of the local maximum activities in the two separated regions, is investigated.

Furthermore, the following measures are defined, which do not rely on a threshold activity at all but take into account all reconstruct current density. First, for each original dipole $k = 1, 2$ at grid position \vec{r}_k in a specific configuration

$$d'_k = \left(\frac{\sum_{i=1}^{N_k} |\vec{j}_i| |\vec{r}_k - \vec{r}_i|^2}{\sum_i^{N_k} |\vec{j}_i|} \right)^{\frac{1}{2}} \quad (3.17)$$

is calculated with \vec{j}_i representing the current density in voxel i and \vec{r}_i giving the position of the center of voxel i . The sums in equation (3.17) run over all voxels in the source space which are closer to dipole k than to the other dipole. The region described by these voxels will be indexed by segment k for the rest of this section. In order to get values between 0 and 1, d'_k is normalized by the largest distance between the original dipole and voxels in segment k

$$r_k^{\max} = \max_{N_k} \{|\vec{r}_k - \vec{r}_i|\} \quad (3.18)$$

obtaining

$$d_k = \frac{d'_k}{r_k^{\max}} \quad (3.19)$$

This measure will be called *activity deviation* in the following. Its analog in classical mechanics is the moment of inertia. Extending this approach by quantifying the whole current reconstruction with only one measure that averages the activity deviations d_k across all segments, the measure

$$d' = \left(\frac{\sum_{i=1}^{N_g} |\vec{j}_i| \min_k \{|\vec{r}_k - \vec{r}_i|^2\}}{\sum_i^{N_g} |\vec{j}_i|} \right)^{\frac{1}{2}} \quad (3.20)$$

is calculated and normalized via

$$d = \frac{d'}{\max_k \{r_k^{\max}\}} \quad (3.21)$$

defining the *averaged activity deviation*. A signal-to-noise ratio of 2 is chosen for all discussed two-dipole simulations.

In the following, two different sets of configurations are described, which will be called configurations I and configurations II in this work. Each consists of several two-dipole setups which differ concerning the positions and relative orientations of the dipoles. The resulting reconstructions of these configurations by GaussMN, MFT, and sLORETA-Laplacian will be interpreted in section 3.3.3.

Configurations I For the first set of two-dipole configurations intermediate x - and z -coordinates have been chosen, which are fixed for all original dipole positions ($x = -7$ cm and $z = 1.5$ cm). The y -coordinate is varied in a way that both original dipoles approach each other between the setups starting from positions in the midrange subregion with a distance of 8.7 cm and ending in the deep region with the smallest possible distance in the used grid (0.9 cm). Configurations with parallel and antiparallel orientations of the dipoles have been tested. This refers to the orientations of the dipoles before removing the radial component due to the applied forward model. For parallel setups both dipoles point to the positive z -axis, for antiparallel ones the dipole in the right hemisphere is rotated by 180 degrees (see figure 3.11). In figure 3.4 all parallel configurations I are sketched.

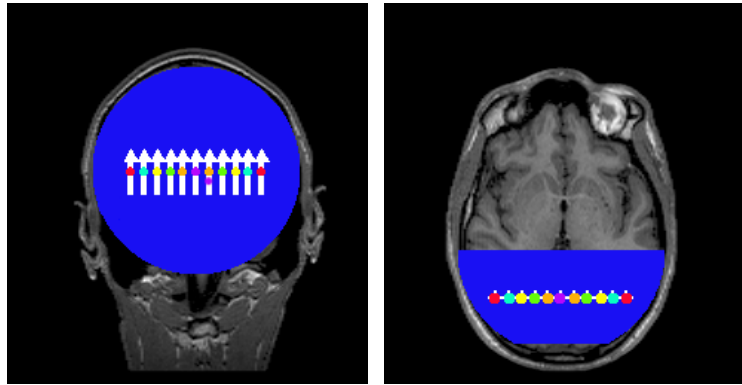


Figure 3.4: Parallel configurations I: white arrows indicate the orientations of the dipoles. Positions of the two dipoles belonging to the same configuration are identified by spots with the same color. The fifth dipole (counting from right to left in the left slice), which is identified by two colored spots in the left slice, is used in two different configurations with the upper spot showing the position. The source space is filled with blue color.

Configurations II In the second set the z -component of all dipole positions is again fixed ($z = 1.5$ cm). Moreover the superficial position of dipole no. 2 in the right hemisphere is the same for all configurations ($x = -9.3$ cm and $y = 4.4$ cm) whereas current dipole no. 1 is wandering from the left hemisphere towards the other dipole between configurations staying superficial all the time.

Parallel, antiparallel, and also orthogonal relative orientations of the dipoles, which are shown in figure 3.5, are tested. In the parallel and antiparallel configurations, both dipoles are arranged in a line parallel to the y -axis in contrast to configurations I (see figure 3.13 for examples).

3.3 Results

In this section the focus is first on single dipole simulations discriminating the investigated reconstruction methods. For this, the fixed value of the regularization parameter α is used which showed the lowest displacement error for each method. Afterwards other regularization strategies (described in sections 2.4.3 and 2.4.4) are compared to the fixed- α approach. Using the best regularization setting according to the performed simulations, MFT, sLORETA-Laplacian and the best

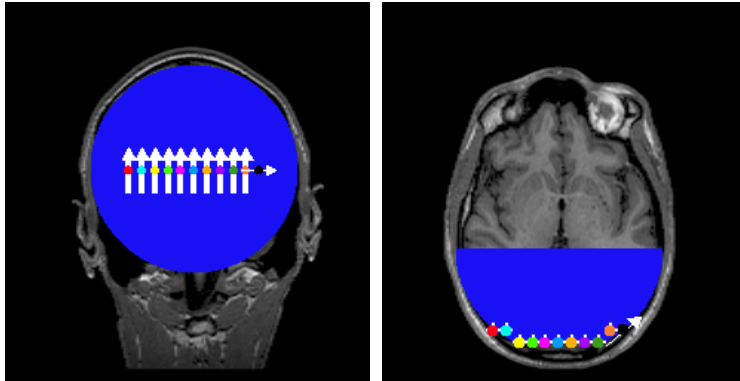


Figure 3.5: Orthogonal configurations II: Dipole no. 2 indicated by a black spot does not change its position between the configurations whereas the other dipole is approaching. Each colored spot at dipole no. 1 describes a different configuration.

Minimum Norm method from the single-dipole tests are further investigated in multiple-dipole configurations.

3.3.1 Single dipole reconstructions

Single dipole reconstructions have been performed for the described methods with different noise levels. Here the grid position of the original dipole has been varied over the entire source space between simulations of each method for a specific noise level and with a fixed regularization parameter. Also, for each position three different dipole orientations (dipole pointing in x -, y -, and z -direction, respectively) have been tested. Each set of calculated measures for a specific noise level and setting of regularization has been averaged over the entire source space and the predefined subregions, respectively, in order to summarize results. The resulting averaged measures of single dipole reconstructions for the MN, lFMN and GaussMN methods are shown in table 3.1 along with the setting of the applied regularization parameter α . The specific value α in table 3.1 was chosen for each combination of noise level and reconstruction method by scanning for the lowest mean of the localization error averaged over the entire source space.

The MN method localizes nicely superficial current dipoles with a relatively focal reconstructed current density distribution but fails in the detection of deeper sources as expected (see e.g. [FWKW99]). Furthermore, the results presented in table 3.1 show that the lFMN method produces a good tradeoff between displacements of deeper and superficial dipoles in the noise-free case, but its performance drops drastically when noise is added to the signals. The averaged localization error in the superficial region (4.5 cm for SNR=1) is similar to the averaged localization error for MN in the deep region. Apparently the very low weighting values in the superficial region compared to deeper positions for lFMN (see figure 3.1) induce this effect.

The GaussMN shows the lowest overall localization error as well as angle difference among the Minimum Norm methods for all noise levels. The volume of activity is significantly larger compared to MN and lFMN but the relatively small displacement of the original dipole makes the spreading measures to be similar to those in MN and lFMN as it quantifies the maximum distance

of the original dipole to activity above the threshold.

The averaged measures of the sLORETA-Laplacian and MFT reconstructions are presented in table 3.2.

Without noise sLORETA-Laplacian shows the best localization error (0.6 cm averaged over the entire source space) among all investigated methods. The increase of the displacement by adding noise however is more pronounced than in the results of the other methods. Taking into account the minimum distance of grid points (0.78 cm), the localization errors of sLORETA-Laplacian and GaussMN are similar in the presence of noise which is true also for the angle difference. However, the reconstructed current density distributions of sLORETA-Laplacian are very blurred compared to all other methods because of the influence of the Laplacian operator what has also been observed in [WFK04].

The localization errors and the angle differences of the MFT method are only slightly smaller compared to GaussMN whereas the solutions tend to be much more focal. Due to its iteration procedure the MFT is much more computationally demanding than the other tested methods. Because of these tremendous computational costs the scanning for the best setting of the regularization parameter ζ in MFT (see equation 3.14) was only performed for a small subset of randomly chosen dipole positions. For this, the reconstruction accuracy for 3 different pairs of x- and y-components of the original dipole position for each of the 9 possible values of the z-component in the source space, i.e. 27 single-dipole configurations, has been tested for different values of ζ .

In figure 3.6 tomographic views of the distribution of the localization error in the source space is presented referring to GaussMN, sLORETA-Laplacian, and MFT. At each position of the original dipole the displacement in its reconstructed current density distribution is color coded. The signal-to-noise ratio was equal to 2 for each individual dipole location and direction and the underlying setting of the regularization parameter α can be gathered from tables 3.1 and 3.2. The tomographies for GaussMN and MFT are rather similar. The chosen decay values of the Gaussian profile, which had been fitted in a test according to the reconstruction of a small subset of single dipoles uniformly distributed in the source space [Dam00], deliver a tradeoff between the displacement of deeper and more superficial sources. The plot is not symmetric with respect to a reflection of right and left hemisphere due to a slightly asymmetric head-sensor configuration. At the bottom of the source space the displacement error is significantly larger than at the top because of a bad coverage of detectors in that area (see figure 3.2). The MFT displays a slightly smaller localization error than the GaussMN method in most grid positions.

The distribution of the localization error of the sLORETA-Laplacian in figure 3.6 shows a relatively homogeneous profile. One reason for this could be the independence of a fitting parameter for its constraint matrix L in equation 2.12. sLORETA-Laplacian is capable to deliver lower values for the displacement for most of the dipoles in the deep subregion as well as at the bottom of the source space compared to MFT and GaussMN.

The angle difference averaged in the superficial subregion (table 3.1 and table 3.2) shows a significant disadvantage of LORETA-Laplacian favoring MFT and GaussMN. Very deep sources produces an angle difference which is much larger than in other areas of the source space for all of these three methods. The averaged values of the volume of activity show the tremendous blurring effect of sLORETA-Laplacian especially in the deep subregion and the superiority of MFT with respect to this measure in all subregions (see also figure 3.7).

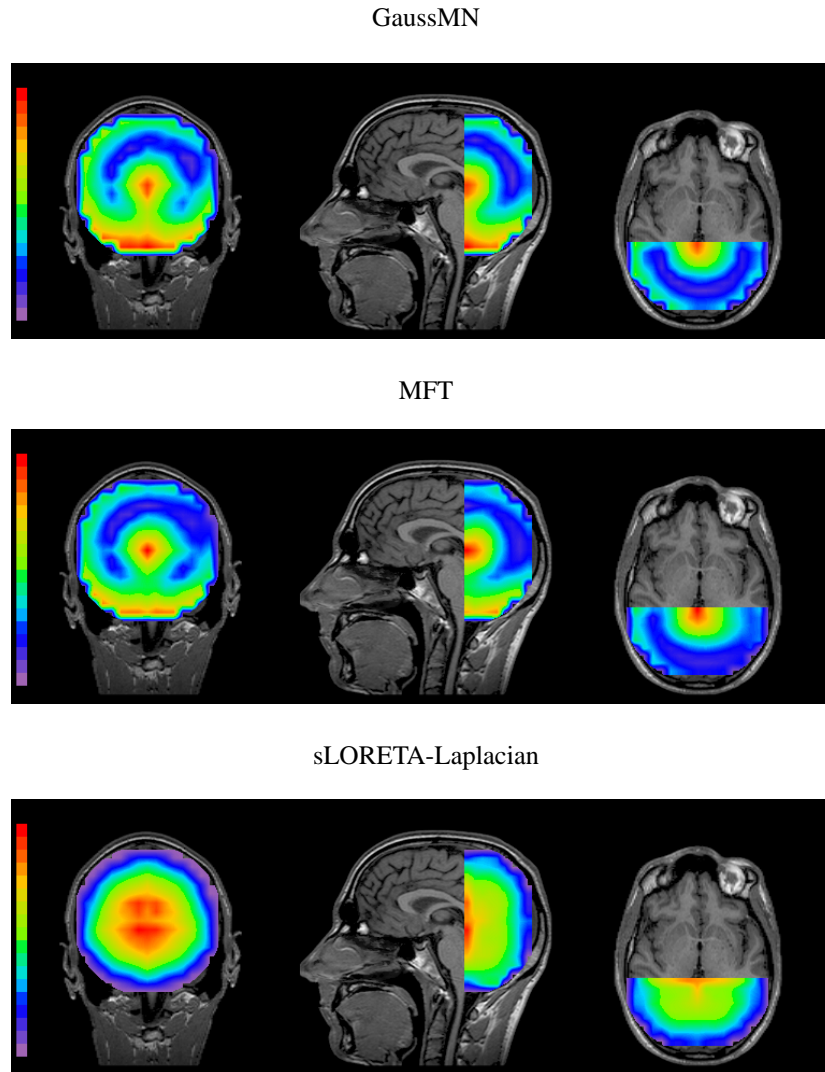


Figure 3.6: Tomographic view of the dependence of the displacement error (color coded in cm) on the position of the dipole in the source space with a signal-to-noise-ratio of 2. The applied reconstruction methods have been GaussMN (top), MFT (middle), and sLORETA-Laplacian (below). The measures for the three tested dipole directions (x -, y -, and z -direction) are averaged for each position. The joint intersection point of the presented slices is $[-3.9 \text{ cm}, 0 \text{ cm}, 1.5 \text{ cm}]$. Values range from 0 to 4 cm where purple indicates the smallest and red the largest values (linear scaling).

3.3.2 Influence of regularization

The results presented so far have been produced with a setting of the regularization parameter α which resulted in the lowest overall localization error. In figure 3.8 the influence of the chosen value of α on the measures is presented exemplary for the GaussMN method. The crucial dependence of α on the mean of the localization error and the angle difference with respect to the entire source space is shown for a signal-to-noise ratio equal to 2. The shape of both graphs is very similar and the value for α at the measured absolute minimum is the same. Especially an

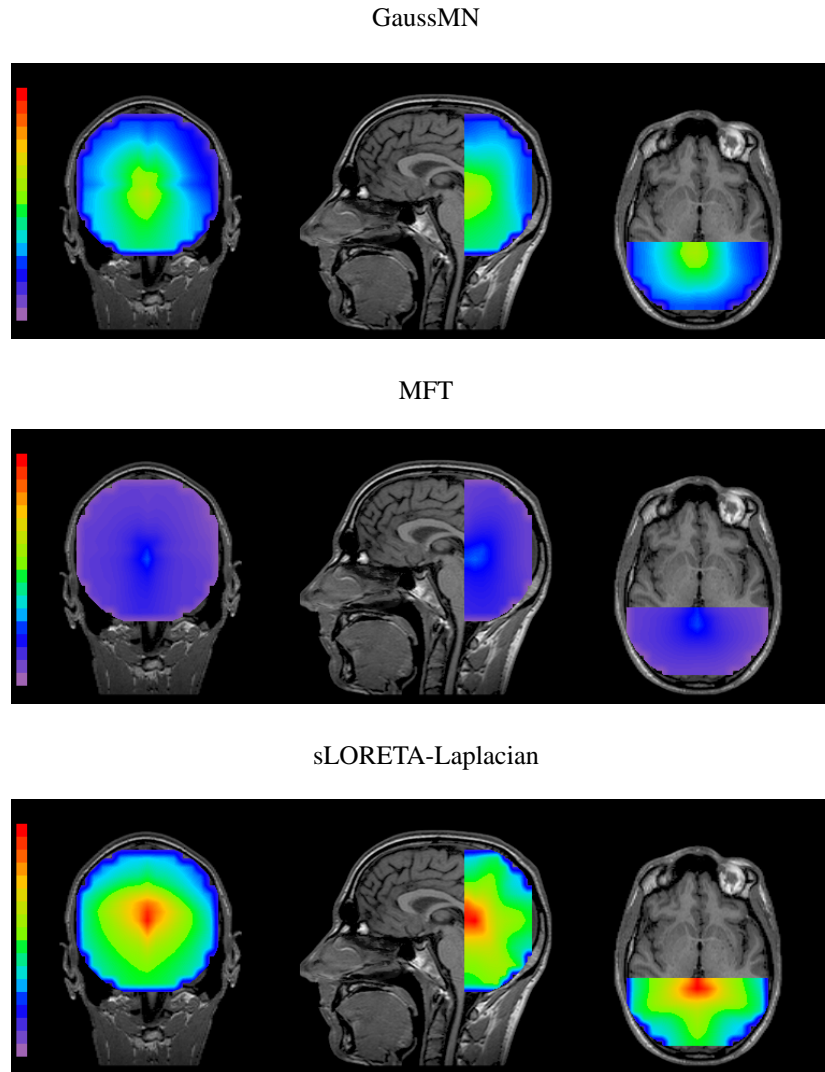


Figure 3.7: Tomographic view of the dependence of the volume of activity (color coded in ml) on the position of the dipole in the source space with a signal-to-noise-ratio of 2; top: applied reconstruction method is GaussMN, middle: MFT, bottom: sLORETA-Laplacian. Values range from 0 (purple) to 450 cm³ (red).

underestimation of α of more than one order of magnitude provokes significantly worse values for the displacement and the angle difference.

In figure 3.9 the influence of truncating the singular value decomposition of the inverse matrix via \tilde{k} (see equation 2.17) instead of regularizing with the aid of α is presented. Here for each setting of \tilde{k} and each dipole position, identified by a one-dimensional index, the localization error and the angle difference are color-coded, with $SNR = 2$. This again demonstrates how important an adequate setting of the regularization parameter is for the accuracy of reconstruction. The influence of the value of \tilde{k} is qualitatively the same for the localization error and the angle difference. In table 3.3 the results of the measures are shown for the best truncating values determined again by inspecting the overall mean of displacements. For $SNR = 1$ the regularization via α (see table 3.1) produces significantly smaller localization errors, angle differences, and spreading

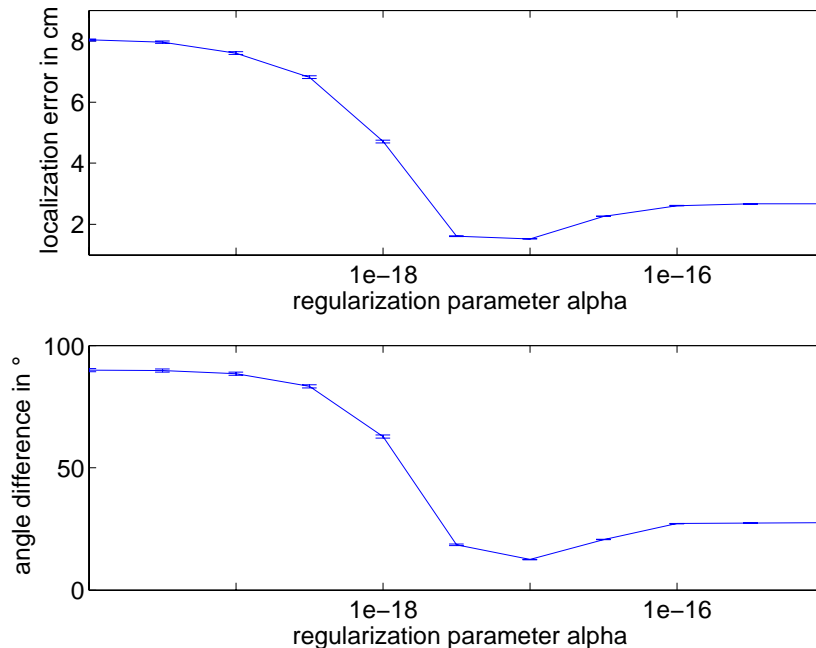


Figure 3.8: Dependence of the localization error (top) and the angle difference on the regularization parameter α for GaussMN ($SNR = 2$). For each setting of α the measures have been averaged over the results of single dipole reconstructions in the entire source space with three different dipole orientations for each position.

values in all regions than regularization via truncating. For $SNR = 2$ truncating shows more focal solutions but regularization with the aid of α reconstructs better the original positions and angles of the dipoles.

Because Pascual-Marqui, the originator of sLORETA, proposes to use cross-validation to regularize his reconstruction method [PM02, PM99a], this regularization technique is tested in simulations with the implemented sLORETA-Laplacian. In table 3.3 the results are shown for the investigated measures and the average setting of α for $SNR = 2$ and $SNR = 1$. If these values are compared with those associated to sLORETA-Laplacian by regularizing with a fixed α (see table 3.2), the displacement and angle differences are similar. However, the measures detecting the expansion of the reconstructed current density distributions discriminate the regularization techniques significantly to the disadvantage of the cross-validation algorithm: averaged over the entire source space with a signal-to-noise ratio of 2 for example, the volume of activity is here more than 2.5 times larger.

3.3.3 Two-dipole reconstructions

In the following, results of two-dipole simulations are shown with respect to the GaussMN, MFT, and sLORETA-Laplacian methods with a signal-to-noise ratio of 2. The applied regularization corresponds to the optimized setting of the regularization parameter α and ζ , respectively, for this strength of noise which can be extracted from table 3.1 and table 3.2, respectively.

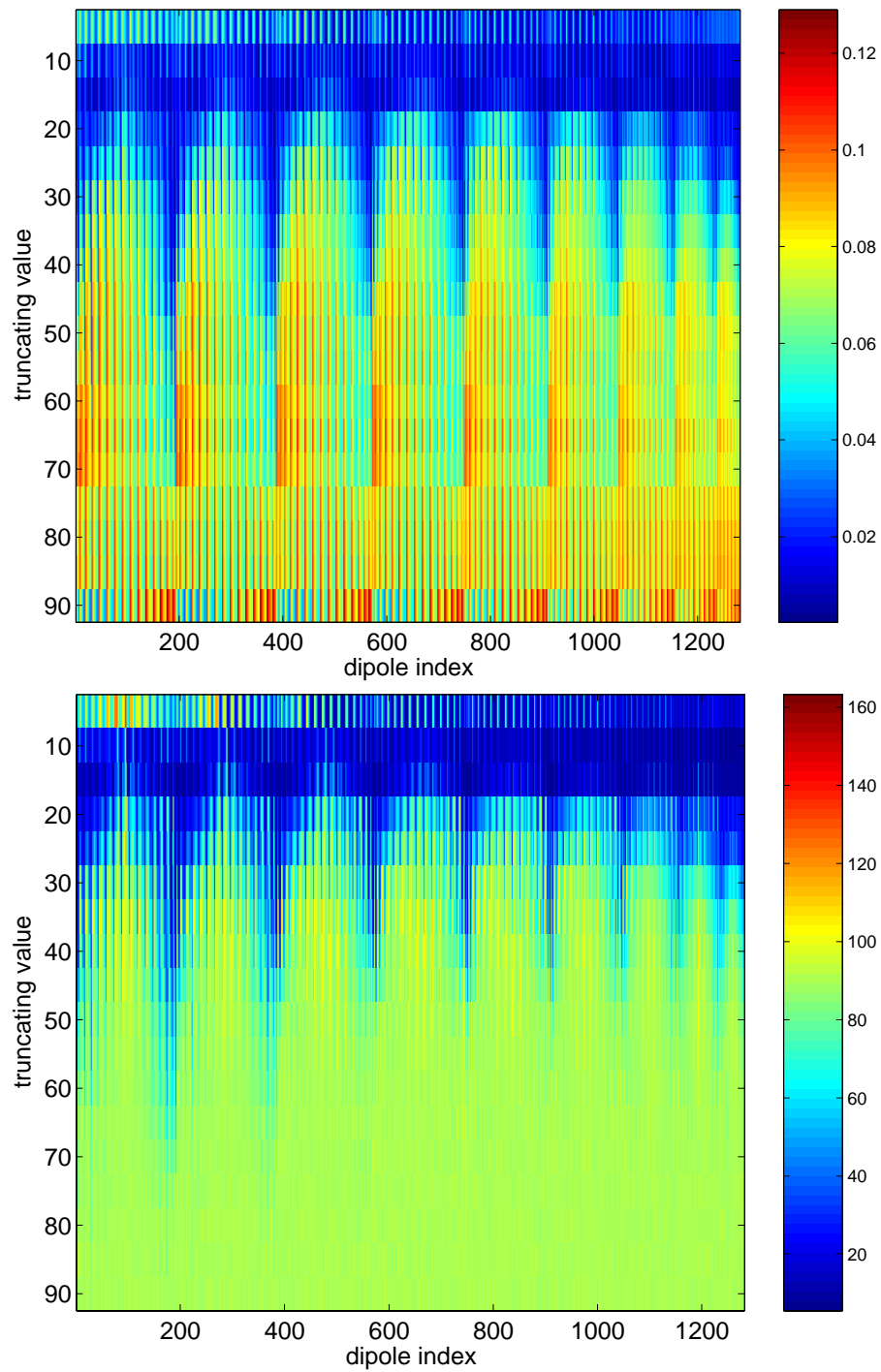


Figure 3.9: Displacement error in cm (top) and angle difference in degree (bottom) versus the truncating value of the singular values for each dipole position. The reconstruction method shown here is the GaussMN with a SNR of 2. The dipole index identifies each dipole position one-dimensionally. From left to right in the figure, the corresponding dipole position is wandering from the bottom frontal area of the source space to the occipital pole of the head. The measures for the three tested dipole directions (x -, y -, and z -direction) are averaged for each position.

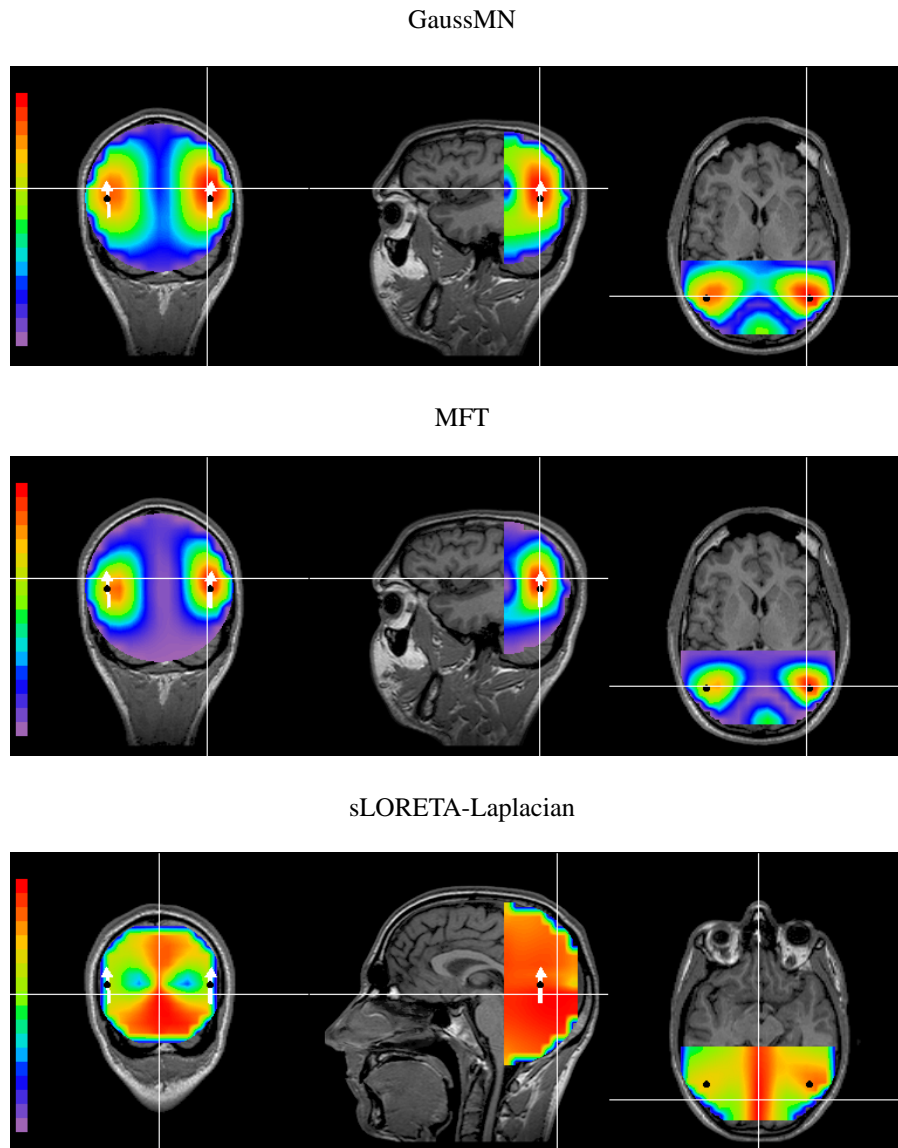


Figure 3.10: Exemplary reconstructions for configurations I with $\text{SNR}=2$: top panel: GaussMN (parallel original dipoles, distance between original dipoles: 8.7 cm), middle: MFT (parallel, 8.7 cm), bottom: sLORETA-Laplacian (parallel, 8.7 cm). The joint intersection point of the shown slices corresponds to the position of maximum activity (white cursor) for all three pictures. The white arrows represent the direction and orientation of the original current dipoles. Their positions are indicated by the black spots at the center of each arrow. The arrows are projected onto the displayed MRT slice in all cases. Values range from 0 (purple) to the maximum of the modulus of the current density in each reconstruction (red).

Configurations I In any of the parallel configurations I, the sLORETA-Laplacian method is not able to resolve the two original dipoles. The reconstructions are very blurred with the largest values for the current density in the middle of both original dipoles (figure 3.10) and relatively lower activity at the positions of the original dipoles, so that the estimated current density distribution does not nearly reflect the real positions of the dipoles. The GaussMN method can only resolve

the parallel dipoles in the configuration with the largest distance tested (8.7 cm, see figure 3.10). Among the parallel configurations MFT resolves the dipoles just for the tested distances larger or equal to 7.0 cm (figure 3.10). It gives more focal solutions than the other methods, which is true for all investigated reconstructions, and delivers relatively small localization errors (see table 3.4 for the resulting measures of configurations I). The estimated current density distributions for GaussMN as well as for MFT exhibit a ghost source in the occipital area (please see figure 3.10) in the parallel configurations I. However, its local maximum of the modulus of the current density is distinctly smaller than those for the other two regions of activity nearby the original dipoles, which still gives resolved current dipoles according to the definition described in section 3.2.5.

Concerning all antiparallel configurations GaussMN, MFT, and sLORETA-Laplacian can produce two clearly separated regions of activity (see figure 3.11 for examples). A problem all methods have in common is the large localization error of antiparallel dipoles which are relatively close together, see e.g. the reconstruction of dipoles with a distance of 5.3 cm in figure 3.11 by MFT. The displacement of the dipoles increases strongly with a decrease of the relative distance (table 3.4). The MFT delivers the lowest values for the localization error but the performance of the GaussMN method is only slightly worse with respect to this measure. The GaussMN method gives the best estimate of the angles of the original dipoles in most cases ahead of MFT and sLORETA. The ratio of the strengths of the original dipole shown in table 3.4 is defined by the ratio of the modulus of the current density at the local maximum of activity associated to dipole no. 1 and the modulus of the current density at the local maximum of activity associated to dipole no. 2. Here, sLORETA-Laplacian reproduces the original ratio of 1 best, whereas GaussMN and MFT underestimate the strength of dipole no. 1. In figure 3.12 the activity deviations for both dipoles and the averaged activity deviation are plotted for the antiparallel configurations I. The values of all these measures increase with decreasing distance of the dipoles which had also been observed with respect to the localization errors. The activity deviations discriminate the reconstruction methods in the same order for all tested distances: MFT gives the lowest and hence best values followed by GaussMN and sLORETA-Laplacian. This is true also for the parallel configurations I giving qualitatively similar results (not shown here). For the antiparallel configurations the difference between sLORETA-Laplacian and the other methods decreases for larger distances between the dipoles.

Configurations II All parallel as well as antiparallel configurations II cannot be reconstructed adequately by any of the tested methods (see figure 3.13 for exemplary reconstructions). The parallel configurations result in estimates of the current density distribution which show only one more or less blurry region of activity even for original sources which are located far away from each other (see figure 3.13 for distance 8.8 cm). This region of activity embraces the positions of both original dipoles. The reconstructions of antiparallel configurations show distinct regions of activity around the positions of the original sources but produce ghost sources (figure 3.13).

Among the orthogonal configurations II the sources can be resolved in case of distances smaller or equal to 7.0 cm with GaussMN and sLORETA-Laplacian (see figure 3.14 for examples). In addition, the MFT method is able to resolve the dipoles in the setup where the original dipoles are 0.8 cm closer to each other. Once again the solutions by MFT are distinctly less blurred (see figure 3.14). All methods can localize dipole no. 2, which is situated in a fixed superficial position in the right hemisphere in all cases, better than the left dipole whose associated local maximum

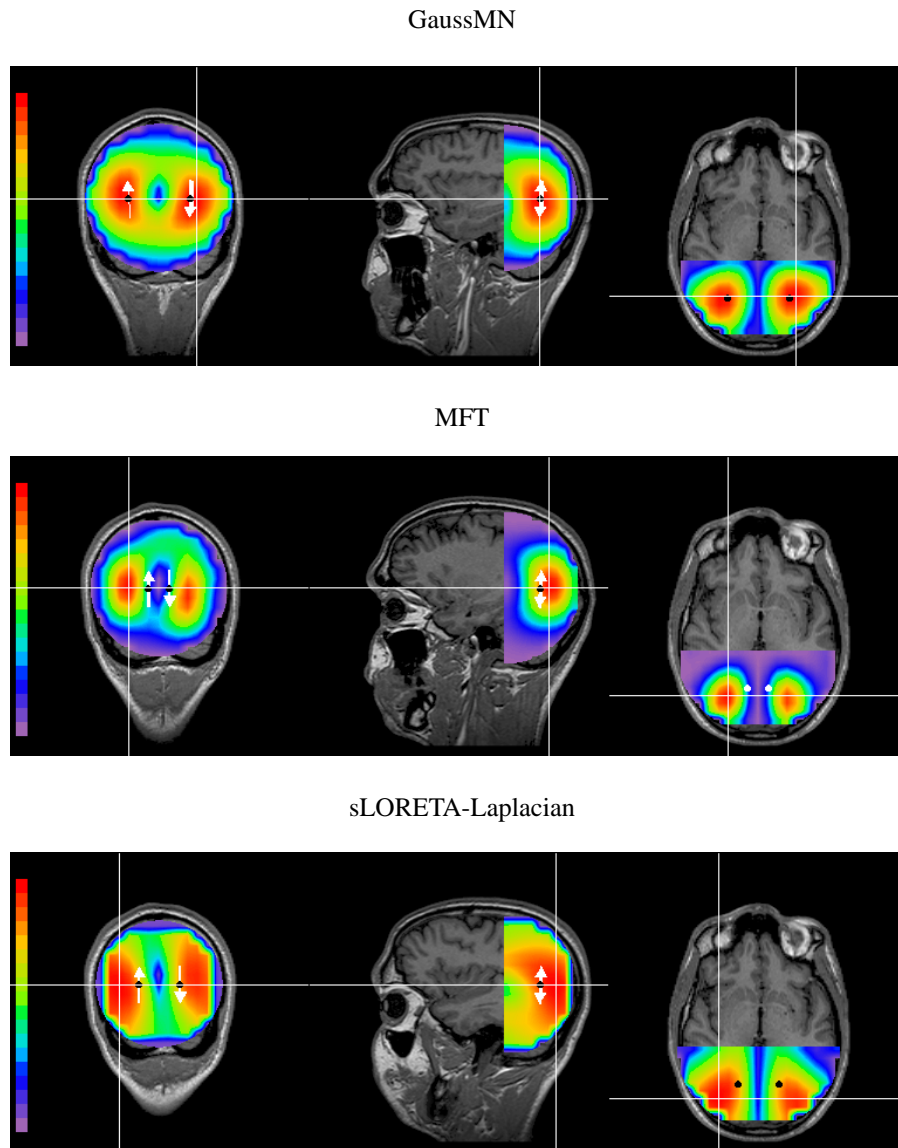


Figure 3.11: Exemplary reconstructions for configurations I with different distances between the original dipoles and $\text{SNR}=2$: top panel: GaussMN (antiparallel original dipoles, distance between original dipoles: 7.0 cm), middle: MFT (antiparallel, 5.3 cm), bottom: sLORETA-Laplacian (antiparallel, 6.2 cm). The white arrows represent the projected original current dipoles whereby their positions are indicated by the spots at the center of each arrow. The color of these spots is white, if the dipole is situated inside the displayed slice, otherwise they are black. Values range from 0 (purple) to the maximum of the modulus of the current density in each reconstruction (red).

of activity is biased downwards. Also, the ratio of strengths shows that dipole no.1 is underestimated. The position of dipole no. 2 is apparently favored with respect to detection which has also been observed in the single dipole reconstructions in MFT and GaussMN (see figure 3.6). The MFT is superior in most reconstructions considering localization error as well as angle difference (table 3.5).

The activity deviations (not shown here) significantly separate the reconstruction methods giv-

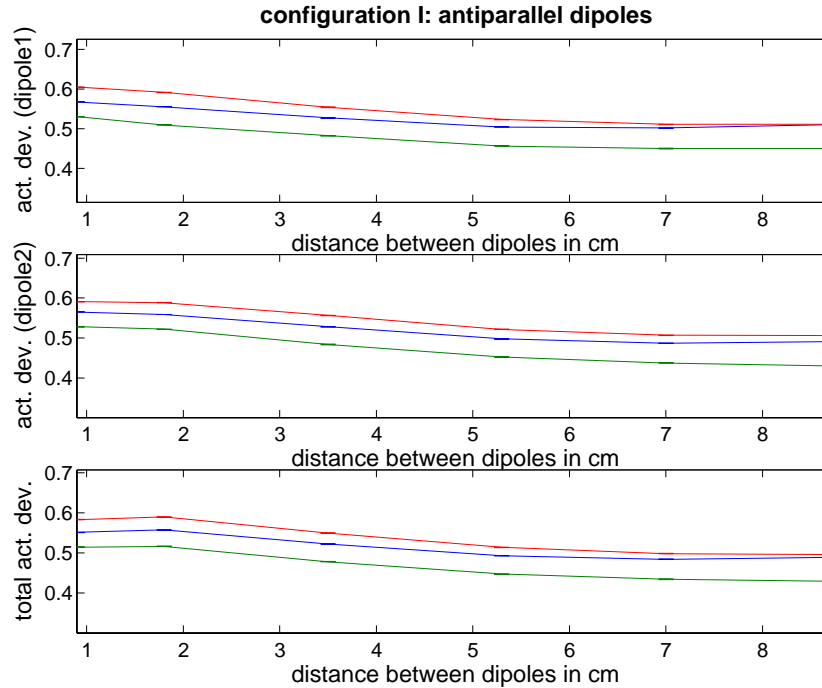


Figure 3.12: Activity deviations for the antiparallel dipoles in configuration I as well as the averaged activity deviation together with the tiny error bars (red: sLORETA-Laplacian, blue: GaussMN, green: MFT). The measures are plotted in dependence of the distance of between the two dipoles.

ing lowest values for MFT and largest values for sLORETA-Laplacian for all orientations and distances between the dipoles considered in this study. This order had also been observed in the results of the activity deviations of configuration I. Moreover in the performed tests these measures do not depend sensitively on the distances between dipoles.

3.4 Discussion

A detailed study concerning the reconstruction accuracy in MEG of several weighted Minimum Norm methods, the sLORETA with a smoothing constraint, and the MFT algorithm has been performed. In order to give quantified results the displacement of the current dipoles in the reconstructed current density distributions, the error in the estimate of the orientation of the original sources, the spreading of solutions, and the relative strength of reconstructed sources in multiple-dipole configurations have been investigated. This makes it possible to discriminate the reconstruction methods. The simulations have shown the importance of including realistic levels of detector noise [Dam00] in evaluating the inverse routines.

With respect to single-dipole configurations, which are intrinsically a very difficult challenge for the tested distributed source models, among the weighted Minimum Norm methods the GaussMN gives overall by far the best values for the localization accuracy as well as the angle estimates, if noise is added to the simulated magnetic signals. Minimum Norm has the well-known ability to

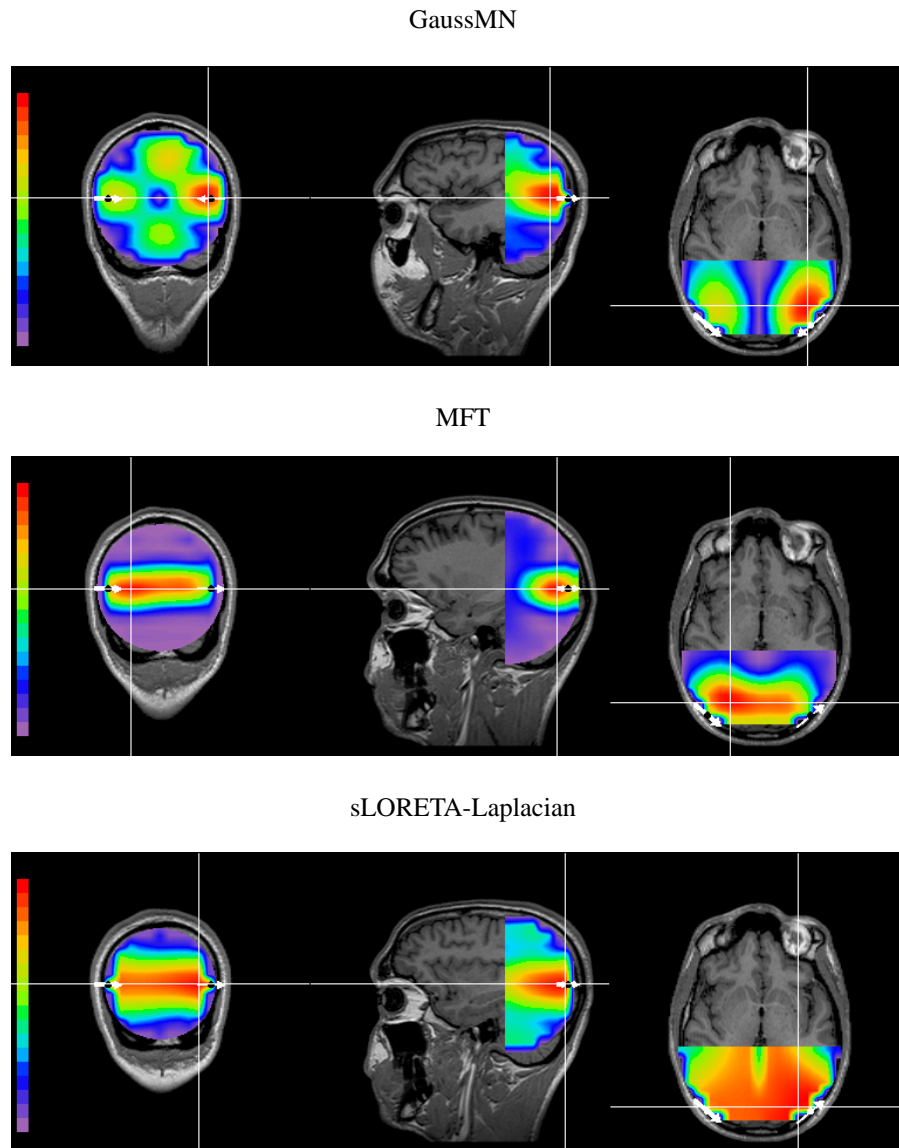


Figure 3.13: Exemplary reconstructions for configurations II with SNR=2: top panel: GaussMN (antiparallel original dipoles, distance between original dipoles: 8.8 cm), middle: MFT (parallel, 8.8 cm), bottom: sLORETA-Laplacian (parallel, 8.8 cm). Values range from 0 (purple) to the maximum of the modulus of the current density in each reconstruction (red).

reconstruct superficial sources relatively well (displacement here between 1.1 cm and 1.3 cm for the tested noise levels) but for deeper current dipoles the reconstruction quality of the unweighted Minimum Norm is not acceptable. The obvious extension of Minimum Norm via weighting by the sensitivity profiles of the detectors gives good results in the noise-free case but the performance drops drastically in the presence of noise compared to the other investigated inverse techniques. Referring to the presented results the empirical weighting function given by a Gaussian profile is superior.

In the light of the applied measures the tested form of sLORETA gives worse reconstruction

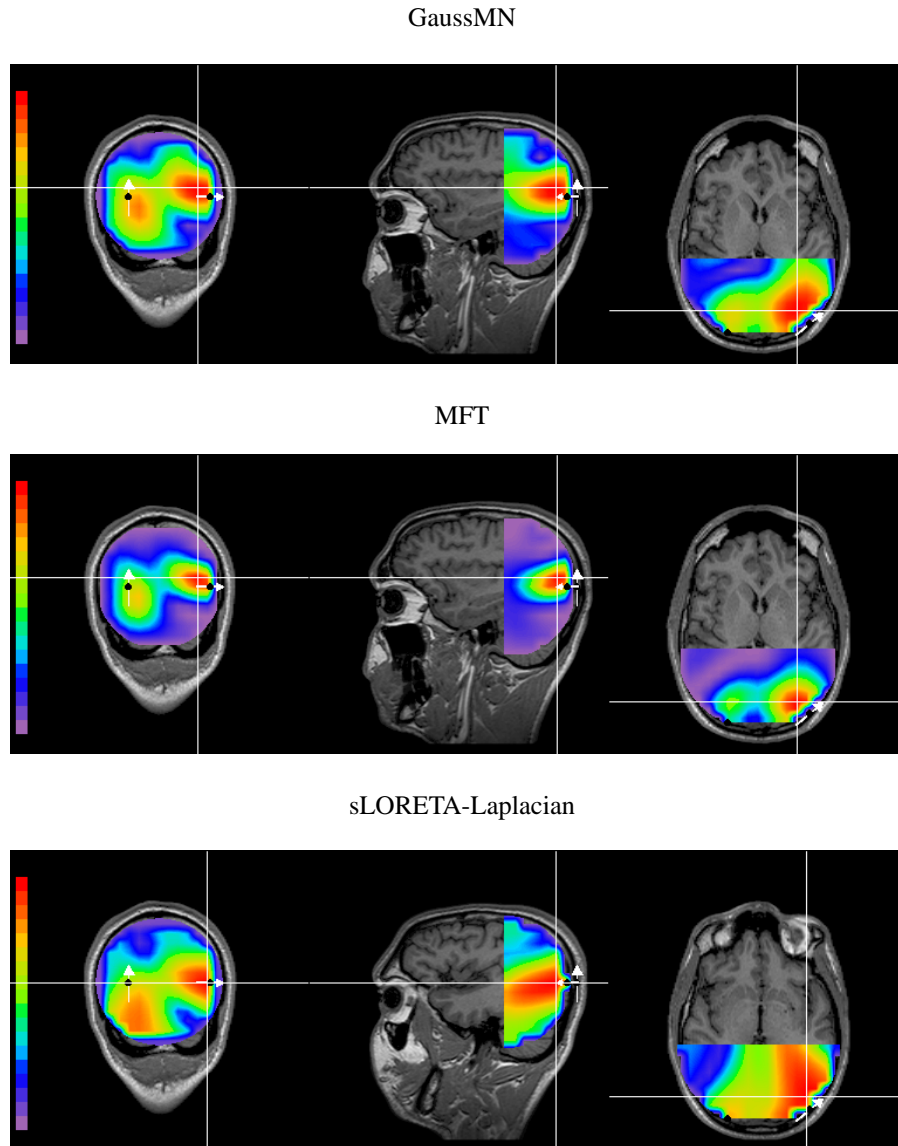


Figure 3.14: Exemplary reconstructions for configurations II with SNR=2: top panel: GaussMN (orthogonal original dipoles, distance between original dipoles: 7.0 cm), middle: MFT (orthogonal, 7.0 cm), bottom: sLORETA-Laplacian (orthogonal, 7.0 cm). Values range from 0 (purple) to the maximum of the modulus of the current density in each reconstruction (red).

results than MFT and the GaussianMN, if detector noise is taken into account. Especially the outcome of the current density estimates of the parallel two-dipole configurations I cause concern. In spite of the implemented standardization in sLORETA the ratio of the strengths of the current dipoles is not correctly reconstructed in all cases which has also been observed in EEG simulations like those shown in [WFK04]. The smoothness constraint in sLORETA proposed in [PMML94] and further criticized in [dPMA00a] results in very blurred current density reconstructions.

In simulation studies without detector noise and for weak noise levels the performance of

sLORETA with uniform weighting was convincing [PM02, WFK04, SSN05]. In contrast, the results obtained here for sLORETA with Laplacian weighting in the presence of realistic detector noise are not encouraging. A Laplacian weighting has been chosen because for the tested noise levels it resulted in a smaller localization error in single dipole simulations than sLORETA with a uniform weighting. Accordingly, it remains to be shown whether sLORETA with an appropriate weighting may perform well also in the presence of strong detector noise compared to weighted Minimum Norm solutions as well as MFT.

Considering all tested configurations the GaussMN, whose definition is very similar to a one-step iterated MFT, shows a slightly worse performance compared to the implemented MFT. Due to its small computation time GaussMN can be exploited for real time applications in contrast to MFT. Because of its iteration MFT gives more focal solutions. In the investigated multiple-dipole configurations the critical distance of the two dipoles, where both cannot be resolved any more in the inverse solution, has been one grid point distance less (approx. 0.8 cm) in MFT than in the other tested methods.

The results of two different sets of two-dipole configurations have been presented. In configurations I both dipoles are situated symmetrically with respect to the detector helmet (except for the sixth configuration in this set; see figure 3.4) so that they evoke magnetic fluxes of similar strengths in corresponding detectors in the case of equal orientations of the dipoles. Configurations II (figure 3.5) simulate a scenario with both sources being located in the cortex. In each set of configurations the distance between the dipoles and their orientations have been varied. The exact values of the measures in these two-dipole configurations depend very much on the relative orientation as well as on the positions of the current dipoles in the source space.

In all investigated distributed source models the resolution is rather poor. A substantial number of tested configurations could not be reconstructed in a satisfiable way by any method. Parallel as well as antiparallel configurations can evoke ghost sources. Parallel ones with both dipoles being aligned tend to produce unseparated current sources even for large distances between the original dipoles (≤ 5 cm). For applications this means that interpretation of results given by the reconstruction methods in this study has to be done with great care. Especially aligned current dipoles which are relatively orientated in an antiparallel way produce distinct artificial regions of activity in the reconstructed current density distribution. It is important to note that this effect does not vanish, if the original current dipoles are situated far away from each other. Thus for these configurations conclusions about the exact number of simultaneously active sources without further information are not advisable.

For single sources and a signal-to-noise ratio equal to 2 the localization error for GaussMN and MFT averaged in the superficial region is 1.5 cm and 1.0 cm, respectively, and averaged in the midrange region it is 1.5 cm and 1.3 cm, respectively. This may be acceptable depending on the applied experiment.

Concerning regularization, which critically influences the quality of reconstruction in all inverse techniques, different approaches have been compared in this work. The truncating-SVD procedure gives worse reconstruction than taking a fitted value of α in the Tikhonov regularization which is fixed here for all single dipole positions and therefore for all given data vectors. The cross-validation procedure, which in general is applicable only for off-line reconstructions (see section 2.4.4), tries to optimize α with the aid of the magnetic signals. Nevertheless the performed tests show that by this, the reconstruction quality decreases compared to the fixed- α approach.

It is worth to invest more efforts in finding an optimal and also automatized regularization for off-line as well as on-line applications. Other available procedures like the *Bayesian approach* [TBAVVS04] and the *generalized cross-validation* [GHW79] should stand a test versus a fitted value of α like that performed in this work.

The GaussMN inverse method in combination with a fixed setting of α provides a constant linear mapping between the measured magnetic fluxes and the estimated current density distribution. This makes it possible to reconstruct the cerebral currents in the realtime MEG system presented in chapter 6. For regularization in practice, knowledge about the present signal-to-noise ratio is important. However between the realistic noise levels tested in this study, the optimal value of α changes only by one order of magnitude. Figure 3.8 shows that especially an underestimation of α by this amount does not influence the reconstruction accuracy severely.

In the following chapter the GaussMN will be the starting point of distributed source models which exhibit an additional constraint. These methods can be considered as a spatial filter which focuses on a specific region of interest inside the source space.

Minimum Norm (MN)					
	displacement/ cm	angle difference/°	volume of activity/cm ³	spreading/ cm	α
stand. error	<0.05	<1.1	<2	<0.05	
<i>no noise</i>					
overall	2.2	12.3	29	4.5	1.0E-14
deep	4.3	20.5	63	6.5	
midrange	2.2	11.9	25	4.5	
superficial	0.9	7.1	13	3.1	
<u>SNR=2</u>					
overall	2.5	16.6	52	6.0	1.0E-13
deep	4.5	26.7	100	7.7	
midrange	2.5	16.6	48	6.1	
superficial	1.1	9.1	26	4.5	
<u>SNR=1</u>					
overall	2.8	23.2	51	6.9	1.0E-13
deep	5.0	39.9	85	8.1	
midrange	2.8	22.4	49	7.2	
superficial	1.3	12.3	28	5.4	
lead field normalized Minimum Norm (lfMN)					
	displacement/ cm	angle difference/°	volume of activity/cm ³	spreading/ cm	α
stand. error	<0.05	<1.1	<1	<0.05	
<i>no noise</i>					
overall	1.9	20.0	38	4.9	1.0E-16
deep	1.7	27.9	30	4.5	
midrange	2.3	21.0	42	4.9	
superficial	1.2	11.9	37	5.2	
<u>SNR=2</u>					
overall	3.3	25.2	41	5.8	1.0E-15
deep	1.8	30.6	29	4.8	
midrange	3.4	24.9	42	5.8	
superficial	4.3	21.9	48	6.6	
<u>SNR=1</u>					
overall	3.5	34.9	46	6.8	1.0E-15
deep	2.0	38.3	33	5.5	
midrange	3.6	32.8	46	6.7	
superficial	4.5	37.0	55	8.0	
Gaussian weighted Minimum Norm (GaussMN)					
	displacement/ cm	angle difference/°	volume of activity/cm ³	spreading/ cm	α
stand. error	<0.05	<0.9	<2	<0.05	
<i>no noise</i>					
overall	1.0	8.8	70	4.4	1.0E-15
deep	1.6	17.5	116	5.4	
midrange	1.1	8.1	70	4.4	
superficial	0.3	3.8	37	3.4	
<u>SNR=2</u>					
overall	1.5	12.5	113	5.7	1.0E-14
deep	1.7	20.9	166	6.4	
midrange	1.5	12.2	110	5.9	
superficial	1.5	6.6	77	4.9	
<u>SNR=1</u>					
overall	1.8	17.5	120	6.5	1.0E-14
deep	2.1	29.9	173	7.0	
midrange	1.7	16.7	118	6.7	
superficial	1.6	10.1	82	5.5	

Table 3.1: Measures of the single dipole reconstructions for the MN, lfMN and GaussMN methods for different noise levels. The measures have been averaged with respect to the entire source space and the subregions, respectively (left column). An upper bound of the standard deviations of the means is given in the first line for each described method. Also shown is the setting of the regularization parameter α for each noise level and reconstruction algorithm.

sLORETA-Laplacian					
	displacement/ cm	angle difference/°	volume of activity/cm ³	spreading/ cm	α
stand. error	<0.05	<0.8	<3	<0.2	
<i>no noise</i>					
overall	0.6	8.5	28	3.3	0
deep	0.9	15.9	68	4.7	
midrange	0.7	7.1	23	3.1	
superficial	0.1	6.1	9	2.6	
<u>SNR=2</u>					
overall	1.5	15.2	190	7.1	1.0E-15
deep	2.4	25.5	269	7.6	
midrange	1.5	12.4	187	7.0	
superficial	0.8	13.7	135	6.8	
<u>SNR=1</u>					
overall	2.0	20.4	338	9.4	1.0E-14
deep	3.0	31.4	459	9.2	
midrange	1.9	17.4	331	9.6	
superficial	1.3	19.0	263	9.1	
MFT					
	displacement/ cm	angle difference/°	volume of activity/cm ³	spreading/ cm	ζ
stand. error	<0.05	<0.9	<1	<0.05	
<i>no noise</i>					
overall	1.0	8.4	33	3.2	1.0
deep	1.4	15.7	51	4.0	
midrange	1.0	7.8	32	3.3	
superficial	0.6	4.1	21	2.6	
<u>SNR=2</u>					
overall	1.3	11.7	35	3.7	1.7
deep	1.6	20.3	53	4.6	
midrange	1.3	11.1	35	3.8	
superficial	1.0	6.8	24	3.0	
<u>SNR=1</u>					
overall	1.7	17.4	47	4.6	3.4
deep	2.1	29.6	64	5.4	
midrange	1.7	16.5	46	4.7	
superficial	1.5	10.4	36	3.8	

Table 3.2: Measures of the single dipole reconstructions for the sLORETA-Laplacian and MFT methods for different noise levels. The measures have been averaged with respect to the entire source space and the subregions, respectively (left column). An upper bound of the standard deviations of the means is given in the first line for each described method. Also shown is the setting of the regularization parameter.

GaussMN: truncating singular values					
	displacement/ cm	angle difference/°	volume of activity/cm ³	spreading/ cm	truncating value
stand. error	<0.06	<1.3	<2	<0.05	
<u>no noise</u>					
overall	1.2	11.1	82	5.4	15
deep	1.7	19.3	119	5.8	
midrange	1.2	10.3	82	5.4	
superficial	0.9	6.7	53	5.0	
<u>SNR=2</u>					
overall	1.6	18.0	88	6.4	15
deep	2.3	30.3	127	6.9	
midrange	1.6	17.2	88	6.4	
superficial	1.1	10.6	58	5.8	
<u>SNR=1</u>					
overall	2.3	27.3	126	7.7	10
deep	2.7	41.2	162	7.4	
midrange	2.2	26.8	128	7.9	
superficial	1.9	17.7	95	7.3	
sLORETA-Laplacian: cross-validation					
	displacement/ cm	angle difference/°	volume of activity/cm ³	spreading/ cm	mean α
stand. error	<0.05	<0.8	<2.5	<0.01	
<u>SNR=2</u>					
overall	1.6	13.9	493.0	11.0	1.5E-13
deep	2.4	23.5	573.1	9.6	
midrange	1.7	10.8	497.9	11.3	
superficial	1.1	13.5	421.4	10.9	
<u>SNR=1</u>					
overall	2.0	19.5	503.2	11.1	2.3E-13
deep	2.9	30.5	574.2	9.5	
midrange	2.3	16.5	506.5	11.3	
superficial	1.4	17.7	442.4	11.6	

Table 3.3: Measures of the single dipole reconstructions for different regularization procedures. The measures have been averaged with respect to the entire source space and the subregions, respectively (left column). An upper bound of the standard deviations of the means is given in the first line for each tested method. Also shown is the applied setting of the truncating parameter \tilde{k} , which produced the lowest overall localization error for each specific noise level (right column), as well as the mean setting of α in using cross-validation.

configurations I

	dipole 1		dipole 2		ratio of strengths
dipole distance/cm	displacement/cm	angle difference/°	displacement/cm	angle difference/°	
<i>gaussMN</i>					
parallel					
8.7	0.7 (0.4)	9.3 (1.1)	0.3 (0.4)	5.8 (0.4)	0.82 (0.06)
<=7.0			{not resolved}		
antiparallel					
8.7	1.2 (0.07)	8.3 (1.0)	1.0 (0.05)	7.1 (0.7)	0.88 (0.02)
7.0	0.8 (0.04)	9.3 (0.4)	0.5 (0.03)	7.3 (0.3)	0.88 (0.01)
5.3	0.8 (0.03)	9.2 (0.4)	1.0 (0.02)	7.4 (0.3)	0.92 (0.01)
3.5	1.3 (0.02)	9.0 (0.3)	1.4 (0.02)	8.3 (0.3)	0.91 (0.01)
1.8	2.0 (0.02)	8.8 (0.3)	2.1 (0.02)	8.6 (0.3)	0.93 (0.02)
0.9	2.9 (0.02)	8.0 (0.3)	2.6 (0.02)	7.5 (0.3)	0.87 (0.04)
<i>MFT</i>					
parallel					
8.7	0.4 (0.04)	5.9 (0.3)	0.3 (0.03)	6.0 (0.3)	0.80 (0.02)
7.0	0.8 (0.07)	12.1 (1.1)	1.0 (0.06)	10.2 (0.6)	0.86 (0.04)
<=5.3			{not resolved}		
antiparallel					
8.7	1.1 (0.07)	8.9 (1.0)	0.7 (0.05)	8.5 (0.9)	0.83 (0.01)
7.0	0.7 (0.03)	8.6 (0.4)	0.6 (0.03)	8.2 (0.4)	0.89 (0.01)
5.3	1.0 (0.03)	8.8 (0.4)	1.2 (0.03)	9.0 (0.4)	0.94 (0.01)
3.5	1.4 (0.02)	9.2 (0.4)	1.6 (0.03)	8.7 (0.4)	0.93 (0.01)
1.8	2.1 (0.02)	9.0 (0.4)	2.3 (0.02)	8.4 (0.3)	0.93 (0.02)
0.9	2.9 (0.02)	10.2 (0.4)	2.6 (0.03)	8.2 (0.3)	0.81 (0.02)
<i>sLORETA-Laplacian</i>					
parallel					
<=8.7			{not resolved}		
antiparallel					
8.7	1.5 (0.3)	14.3 (2.3)	1.3 (0.4)	12.9 (1.8)	0.94 (0.03)
7.0	1.8 (0.1)	14.2 (1.2)	1.7 (0.1)	13.1 (0.8)	1.00 (0.02)
5.3	2.5 (0.06)	11.5 (0.5)	2.3 (0.05)	11.0 (0.5)	1.04 (0.02)
3.5	3.0 (0.03)	10.9 (0.5)	3.0 (0.03)	10.3 (0.5)	1.00 (0.02)
1.8	3.6 (0.02)	10.9 (0.4)	3.6 (0.02)	10.2 (0.4)	1.00 (0.02)
0.9	4.1 (0.02)	11.2 (0.5)	3.7 (0.03)	8.7 (0.4)	0.90 (0.03)

Table 3.4: Measures of the reconstructions of configurations I. In closed brackets the standard errors of the means are presented. The ratio of the strength of the reconstructed dipoles is given by the fraction of the modulus of the reconstructed current density of dipole no. 1 and the modulus of the reconstructed current density of dipole no. 2.

configurations II

dipole distance/cm	dipole 1 displacement/cm	dipole 1 angle difference/°	dipole 2 displacement/cm	dipole 2 angle difference/°	ratio of strengths
<i>gaussMN</i>					
parallel					
<=8.8			{not resolved}		
antiparallel					
<=8.8			{not resolved}		
orthogonal					
8.8	2.2 (0.2)	16.2 (0.4)	1.5 (0.3)	10.1 (0.3)	0.87 (0.01)
7.9	2.2 (0.2)	22.6 (0.4)	1.4 (0.02)	9.6 (0.3)	0.75 (0.01)
7.0	2.1 (0.03)	23.0 (0.4)	1.5 (0.03)	14.1 (0.4)	0.87 (0.01)
<=6.2			{not resolved}		
<i>MFT</i>					
parallel					
<=8.8			{not resolved}		
antiparallel					
<=8.8			{not resolved}		
orthogonal					
8.8	1.4 (0.5)	6.5 (0.4)	1.1 (0.5)	7.8 (0.4)	0.80 (0.03)
7.9	1.5 (0.06)	12.3 (1.1)	1.0 (0.03)	7.0 (0.3)	0.62 (0.02)
7.0	1.6 (0.04)	13.2 (0.4)	1.1 (0.03)	9.8 (0.6)	0.71 (0.01)
6.2	1.7 (0.04)	18.3 (0.5)	1.0 (0.02)	11.0 (0.4)	0.65 (0.01)
<=5.3			{not resolved}		
<i>sLORETA-Laplacian</i>					
parallel					
<=8.8			{not resolved}		
antiparallel					
<=8.8			{not resolved}		
orthogonal					
8.8	0.5 (0.09)	17.3 (1.2)	1.3 (0.1)	34.3 (1.7)	0.87 (0.07)
7.9	2.3 (0.1)	28.3 (1.2)	0.8 (0.09)	28.9 (1.4)	0.76 (0.03)
7.0	1.7 (0.1)	25.7 (1.0)	0.8 (0.09)	31.8 (1.1)	0.89 (0.03)
<=6.2			{not resolved}		

Table 3.5: Measures of the reconstructions of configurations II. In closed brackets the standard errors of the means are presented. The ratio of the strength of the reconstructed dipoles is given by the fraction of the modulus of the reconstructed current density of dipole no. 1 and the modulus of the reconstructed current density of dipole no. 2.

Chapter 4

Specialized distributed source models

Using the distributed source models in the preceding chapter, the ill-posed MEG problem results in more or less spreaded reconstructed current density distributions. Considering the tested focal source configurations, anatomical conclusions about active brain regions in experiments with the aid of these methods are problematic. Another problem arises, if the experimenter is interested in the time course of current densities in a specific area, e.g. in order to apply a feedback protocol: activities in other source space regions affect the reconstructed current density in the *region of interest* (ROI) in a significant way. The current densities in the brain are calculated from the MEG signals. The nature of the way the MEG data is recorded guarantees that each signal has a certain amount of *cross-contamination* from other locations [DN02]. This results in a bias concerning the estimates of dynamical measures like synchronization indices or coherence measures between different brain areas [TRW⁺98, DN02].

In order to reduce these *mixing* effects specialized distributed source models have been designed. These reconstruction methods use an additional constraint besides the definition of the depth weighting matrix L (equation 2.12). In this chapter the *Spatially Optimal Fast Initial Analysis Of Biomagnetic Signals* (SOFIA) according to [BGLI99] and the so called *Weighted Resolution Optimization Method* (WROP [dPMHA⁺97]) will be presented. They are implemented with an additional condition to reduce the contamination between a region of interest and the remaining source space. The aim is to increase the ratio of reconstructed activity in that area of the brain, which actually exhibits active sources, and reconstructed activity in other parts of the brain. The latter can be regarded as some projection from the real sources due to cross-contamination between regions resulting from the inverse problem, which is a projection from the real sources due to the cross contamination between regions. Hence the resolution between brain areas would be increased regarding to the reconstructed current density distribution. Truly active regions would show larger reconstructed activity than without the additional constraint. Due to the ill-posed problem this improvement is at the costs of the resolution between active sources inside the region of interest and the resolution between sources within the remaining source space.

The specialized distributed source models are designed to be useable for realtime applications, too. They also deliver a linear mapping between the measured MEG signals and the estimated current density distribution, which could be implemented in the realtime system presented in chapter 6.

SOFIA and WROP will be compared to the best linear method from the study shown the pre-

ceding chapter, the GaussMN inverse algorithm. The WROP technique will be improved in this work to recover deeper current sources and to reduce the contamination effects in the reconstruction process.

4.1 SOFIA

SOFIA builds on the weighted Minimum Norm methods. In the original work of SOFIA [BGLI99] a uniform depth weighting had been tested. In this work the successful Gaussian profile from the GaussMN routine and the MFT, respectively, is chosen as the depth weighting function for the version of SOFIA under investigation. The user of SOFIA is moreover supposed to predefine a ROI whose associated activity is of special interest in the performed experiment. For the explanation of SOFIA it makes sense to use a different notation for the solution of the underlying Minimum Norm method than in the matrix equation 2.14, which is repeated here:

$$\vec{j} = (L^T L)^{-1} \Phi^T (\Phi (L^T L)^{-1} \Phi^T + \alpha 1)^{-1} \vec{m} \quad (4.1)$$

In the following α will be set to 0 as in the original formulation of SOFIA [BGLI99]. The regularization process will be discussed at the end of this section. The estimated current density distribution in equation 4.1 can be written as

$$\vec{j}(\vec{r}) = \sum_{k=1}^{N_d} w(\vec{r}) a_k \vec{\phi}_k(\vec{r}) \quad (4.2)$$

whereby $\vec{j}(\vec{r})$ provides the reconstructed current density vector at source space grid point \vec{r} , $\vec{\phi}_k(\vec{r})$ is the lead field of the k -th detector at grid point \vec{r} and $w(\vec{r})$ is given by

$$w(\vec{r}) = \exp\left(-\frac{y^2 + z^2}{\lambda_{y,z}^2} - \frac{x^2}{\lambda_x^2}\right) \quad (4.3)$$

defining the weighting profile. With this definition, it holds $w(\vec{r}) = (L^T L)_{ii}^{-1}$, if \vec{r} is the position of the grid point belonging to the i -th voxel and L is defined like in the GaussMN method (section 3.1.1). The coefficients a_k are obtained by inverting

$$m_i = \sum_{j=1}^{N_d} P_{ij} a_j \quad \text{with} \quad P_{ij} = \int_S \vec{\phi}_i(\vec{r}) \cdot \vec{\phi}_j(\vec{r}) w(\vec{r}) d^3 r \quad (4.4)$$

Matrix P stands for the term $\Phi (L^T L)^{-1} \Phi^T$ in the former notation according to equation 4.1. It gives the products of the lead field vectors between sensors integrated over the source space S . The key idea in SOFIA is to obtain *virtual lead fields* $\vec{\chi}_i(\vec{r})$ with specific characteristics via a linear transformation of the physical lead fields $\vec{\phi}_i(\vec{r})$ [BGLI99]

$$\vec{\chi}_i(\vec{r}) = \sum_{k=1}^{N_d} c_{ik} \vec{\phi}_k(\vec{r}) \quad (4.5)$$

The coefficients c_{ik} will be derived in this section. The new lead fields have the condition to be orthonormal in the sense of

$$\int_S \vec{\chi}_i(\vec{r}) \cdot \vec{\chi}_k(\vec{r}) w(\vec{r}) d^3 r = \delta_{ik} \quad (4.6)$$

Furthermore they have to be ordered descendently according to their *degree of localization* inside the region of interest. The degree of localization is defined by [BGLI99]

$$l_i = \frac{\Omega_{ext} \int_{S_{int}} |\vec{\chi}_i(\vec{r})|^2 w(\vec{r}) d^3 r}{\Omega_{int} \int_{S_{ext}} |\vec{\chi}_i(\vec{r})|^2 w(\vec{r}) d^3 r} \quad (4.7)$$

Ω_{int} is the volume of the ROI and Ω_{ext} the volume of the source space without the ROI. Moreover S_{int} is the region of interest and S_{ext} the remaining source space. Thus l_i gives the ratio of the mean sensitivities of the i -th *virtual detector* inside the ROI and outside the ROI.

Following the concept of virtual lead fields, the quantities

$$\mu_i = \sum_{k=1}^{N_d} c_{ik} m_k \quad (4.8)$$

can be considered as *virtual signals* because the measured signals $m_i = \int_S \vec{\phi}_i(\vec{r}) \cdot \vec{j}(\vec{r}) d^3 r$ together with equations 4.5 and 4.8 deliver

$$\mu_i = \int_S \vec{\chi}_i(\vec{r}) \cdot \vec{j}(\vec{r}) d^3 r \quad (4.9)$$

Hence the equations for the measured signals $m_i = \int_S \vec{\phi}_i(\vec{r}) \cdot \vec{j}(\vec{r}) d^3 r$ and equations 4.9 have the same form, if the lead fields are replaced by the virtual lead fields. According to SOFIA the estimated current density distribution should now be described by an expansion of the virtual lead fields

$$\vec{j}(\vec{r}) = \sum_{k=1}^{N_d} w(\vec{r}) b_k \vec{\chi}_k(\vec{r}) \quad (4.10)$$

instead of the physical lead fields in equation 4.2. Because the virtual lead fields are orthonormal in the sense of equation 4.6, from equation 4.9 and equation 4.10 it follows that $\mu_k = b_k$, if $\vec{j}(\vec{r}) = \vec{j}(\vec{r})$ [BGLI99].

The ansatz for the estimation of the current density distribution inside the ROI is now given by [BGLI99]

$$\vec{j}(\vec{r}) \approx \sum_{k=1}^{N_f} w(\vec{r}) \mu_k \vec{\chi}_k(\vec{r}) \quad (4.11)$$

which is the linear estimation of the current density distribution by the N_f strongest localized virtual lead fields. On the one hand, the parameter N_f ($N_f \leq N_d$) should be set to such a low value that it prevents projections of activity from outside the ROI by virtual lead fields with low degree of localization. On the other hand, a sufficient number of virtual detectors has to be used in order to provide an adequate reconstruction inside the region of interest [BGLI99].

In estimating $\vec{j}(\vec{r})$ according to formula 4.11, the coefficients c_{ik} have to be determined to obtain

μ_k and $\vec{\chi}_k$ according to equations 4.8 and 4.5. Their description will be deduced in the following. First, a singular value decomposition of matrix P gives

$$P = U^T Q U \quad (4.12)$$

with a diagonal matrix Q and an orthogonal matrix U as described in section 2.4.3. The diagonal elements of Q are denoted by q_i . In the next step, a further set of virtual lead fields is defined by

$$\vec{\theta}_i(\vec{r}) = \frac{1}{\sqrt{q_i}} \sum_{k=1}^{N_d} U_{ik} \vec{\phi}_k(\vec{r}) \quad (4.13)$$

These functions are also orthonormal with respect to the entire source space, because it holds

$$\int_S \vec{\theta}_i(\vec{r}) \cdot \vec{\theta}_n(\vec{r}) w(\vec{r}) d^3 r = \frac{\sum_{k,l=1}^{N_d} U_{ik} P_{kl} U_{ln}^T}{\sqrt{q_i q_n}} = \delta_{in} \quad (4.14)$$

Furthermore, the following matrices P^{ext} and P^{int} are defined

$$P_{ik}^{ext} = \int_{S_{ext}} \vec{\theta}_i(\vec{r}) \cdot \vec{\theta}_k(\vec{r}) w(\vec{r}) d^3 r \quad (4.15)$$

$$P_{ik}^{int} = \int_{S_{int}} \vec{\theta}_i(\vec{r}) \cdot \vec{\theta}_k(\vec{r}) w(\vec{r}) d^3 r \quad (4.16)$$

Please note that $P^{ext} + P^{int} = 1$. These matrices are real and symmetric and can thus be diagonalized in a joint basis. Another SVD delivers

$$P^{ext} = V^T Q^{ext} V \quad \text{and} \quad P^{int} = V^T Q^{int} V \quad (4.17)$$

where V is an orthogonal matrix. Q^{ext} and Q^{int} denote diagonal matrices with singular values $0 \leq q_i^{ext} \leq 1$ arranged in order of increasing magnitude and $0 \leq q_i^{int} \leq 1$ arranged in order of decreasing magnitude. It holds $q_i^{ext} + q_i^{int} = 1$ for all i . If the virtual lead fields $\vec{\chi}_i(\vec{r})$ are now given by

$$\vec{\chi}_i(\vec{r}) = \sum_{j=1}^{N_d} V_{ij} \vec{\theta}_j(\vec{r}) \quad (4.18)$$

it holds

$$\int_{S_{ext}} \vec{\chi}_i(\vec{r}) \cdot \vec{\chi}_j(\vec{r}) w(\vec{r}) d^3 r = \sum_{kl=1}^{N_d} V_{ik} P_{kl}^{ext} V_{lj}^T = q_i^{ext} \delta_{ij} \quad (4.19)$$

$$\int_{S_{int}} \vec{\chi}_i(\vec{r}) \cdot \vec{\chi}_j(\vec{r}) w(\vec{r}) d^3 r = \sum_{kl=1}^{N_d} V_{ik} P_{kl}^{int} V_{lj}^T = q_i^{int} \delta_{ij} \quad (4.20)$$

This helps to show that the virtual lead fields constructed in this way are orthonormal with respect to the entire source space, because

$$\int_S \vec{\chi}_i(\vec{r}) \cdot \vec{\chi}_j(\vec{r}) w(\vec{r}) d^3 r = (q_i^{ext} + q_i^{int}) \delta_{ij} = \delta_{ij} \quad (4.21)$$

The degree of localization (formula 4.7) can now be calculated easily, because

$$\frac{\Omega_{ext} \int_{S_{int}} |\vec{\chi}_i(\vec{r})|^2 w(\vec{r}) d^3 r}{\Omega_{int} \int_{S_{ext}} |\vec{\chi}_i(\vec{r})|^2 w(\vec{r}) d^3 r} = \frac{\Omega_{ext} q_i^{int}}{\Omega_{int} q_i^{ext}} = \frac{\Omega_{ext} q_i^{int}}{\Omega_{int} (1 - q_i^{int})} \quad (4.22)$$

The virtual lead fields $\vec{\chi}_i(\vec{r})$ are ordered descendently with respect to the degree of localization as desired. The wanted coefficients c_{ij} are now given by using the functions $\vec{\theta}_i(\vec{r})$ according to definition 4.13 in equation 4.18 (cf. equation 4.5):

$$c_{ij} = \sum_{k=1}^{N_d} \frac{V_{ik} U_{kj}}{\sqrt{q_k}} \quad (4.23)$$

The current density distributions reconstructed by SOFIA can now be determined by using these coefficients to build the virtual lead fields according to equation 4.5 and the virtual signals according to equation 4.8 and finally $\vec{j}(\vec{r})$ in formula 4.11. The setting of N_f has to be tested. It gives a tradeoff between two characteristics of the reconstructed current density distribution inside the ROI: the accuracy of the resolution of sources inside the ROI and the reduction of contamination between signals originating from the region of interest and sources localized inside the remaining source space [BGLI99]. The virtual lead fields $\vec{\chi}_i(\vec{r})$ build an optimal hierarchy with respect to the degree of localization in the following sense: no linear combination of the physical lead fields $\vec{\phi}_i(\vec{r})$ is stronger localized in the region of interest, referring to the criterion in equation 4.7, than $\vec{\chi}_1(\vec{r})$. Moreover $\vec{\chi}_2(\vec{r})$ is the optimal choice concerning the degree of localization among linear combinations of the physical lead fields which are orthogonal to $\vec{\chi}_1(\vec{r})$ and so forth [BGLI99]. Furthermore it can be shown that SOFIA is equivalent to GaussMN, if N_f is set to its maximal possible value N_d in equation 4.11. Hence it delivers an approximated reconstructed current density distribution compared to GaussMN, which is the same as for GaussMN for the extreme case $N_f = N_d$. According to SOFIA, the aim of the approximation is to focus on the region of interest [BGLI99].

The singular values q_k , whose reciprocals are needed in equation 4.23, are the result of an SVD of matrix P . This matrix has to be regularized because of the ill-posed problem. In [BGLI99] no useful recipe is proposed for its regularization. Taking into account the discretization of the source space, this matrix however is the same as the one which had to be inverted in GaussMN (see equation 4.4 and following comments). In the light of the tests of GaussMN presented in the preceding chapter, matrix P for SOFIA is therefore regularized via an appropriate setting of the regularization parameter α as described in section 2.4.3. The applied setting of α , which depends on the signal-to-noise ratio, can be gathered from the results for GaussMN in table 3.1. Explicitly, after regularization with a fixed α formula 4.23 for the coefficients c_{ij} is changed to

$$c_{ij} = \sum_{k=1}^{N_d} \frac{V_{ik} U_{kj}}{\sqrt{q_k + \alpha}} \quad (4.24)$$

This adequate regularization developed in this work is absolutely necessary to apply SOFIA in practice. Before SOFIA is tested concerning its ability to reduce the mixing of different brain areas, the WROP technique is presented. This alternative approach is more general than SOFIA [dPMHA⁺97]. Its concept improved in this work is introduced next.

4.2 WROP

WROP [BG68, dPMHA⁺97, dPMA99] also belongs to the class of linear distributed source models. In matrix notation the estimated current density distribution $\vec{\hat{j}}$ can be written as

$$\vec{\hat{j}} = G\vec{m} \quad (4.25)$$

with a linear mapping which will be specified in the following. Matrix G , which maps the measured magnetic fluxes to the reconstructed current density reconstructions, has the dimension $(3 \cdot N_s) \times N_d$ (N_s : number of source space grid points, N_d : number of detectors). Component r ($r = 1, 2, 3$) of the current density at grid point i is obtained by

$$\hat{j}_i^r = \sum_{k=1}^{N_d} G_{ik}^r m_k \quad (4.26)$$

Here G_{ik}^r describes that entry in matrix G (see also equation 2.9) which connects the signal of detector k with the r -th component of the estimated current density at voxel i . Here detector noise is not taken into account. The mapping between the original current density distribution \vec{j} and the estimated current density distribution $\vec{\hat{j}}$ is now explicitly given by

$$\hat{j}_i^r = \sum_{k,s=1}^{N_s,3} \left(\sum_{l=1}^{N_d} G_{il}^r \Phi_{lk}^s \right) j_k^s \quad (4.27)$$

In the preceding equation Φ_{lk}^s is that entry in matrix Φ which describes the lead field of detector l at grid point k referring to direction s . The term in braces defines the resolution matrix R (dimension: $(3 \cdot N_s) \times (3 \cdot N_s)$) delivering

$$\hat{j}_i^r = \sum_{k,s=1}^{N_s,3} R_{ik}^{rs} j_k^s \quad (4.28)$$

The rows of the resolution matrix are also called *resolution kernels* [dPMHA⁺97]. They determine the reconstructed current density \hat{j}_i^r for a specific voxel i and a specific direction r . The columns are called *point spread functions* [PM99b]. In the ideal case of a perfect linear reconstruction method, which the ill-posed biomagnetic inverse problem disallows, its associated resolution matrix would be equal to 1. The entry

$$R_{ik}^{rs} = \sum_{l=1}^{N_d} G_{il}^r \Phi_{lk}^s \quad (4.29)$$

of the resolution matrix describes the influence of component s of the original current density at grid position k in the source space on the reconstructed component r of the current density at grid position i . Thus, in the optimal case, i.e. without mixing effects during reconstruction, this entry would be 1 for $i = k$ together with $r = s$ and 0 otherwise.

In WROP the starting point for the derivation of matrix G is a cost function which measures the

distance between the actual resolution matrix and the perfect resolution matrix. This cost function is defined by [dPMHA⁺97]

$$s(R) = \sum_{i,k,r,s=1}^{N_s, N_s, 3, 3} W_{ik}^{rs} (R_{ik}^{rs} - \delta_{ik}^{rs})^2 \quad \text{with} \quad (4.30)$$

$$\delta_{ik}^{rs} = \begin{cases} 1 & : \text{ if } (r = s \quad \wedge \quad i = j) \\ 0 & : \text{ otherwise} \end{cases} \quad (4.31)$$

The wanted matrix G providing the inverse mapping is derived by minimization of this cost function as shown later. In the WROP approach the weighting coefficients W_{ij}^{rs} play an important role: by their specific choice, certain terms $(R_{ij}^{rs} - \delta_{ij}^{rs})^2$ in the cost function are penalized stronger than others which influences the derived reconstruction mapping. Please note that this additional weighting introduced by WROP is independent of the depth weighting discussed in the preceding chapter. By manipulation of the cost function via its weighting coefficients, WROP puts an additional constraint on the solution.

Menendez et al. for example proposed to define $W_{ij}^{rs} = 1 + |\vec{r}_i - \vec{r}_j|^2 + (1 - \delta_{rs})\gamma$ with \vec{r}_i and \vec{r}_j , respectively, denoting the positions of grid point i and j , respectively [dPMHA⁺97]. Their idea is the following. Every component \hat{j}_i^r is a weighted average of the actual current density distribution \vec{j} . The weighting factors for this average are given by that row of the resolution matrix which is responsible for the reconstruction of the r -th component of the current density in voxel i . By penalizing more remote voxels stronger in their cost function, Menendez et al. intended to produce resolution kernels which have a distinct peak around \vec{r}_i and are less spreaded over the source space. This would reduce the contamination of current densities from remote voxels. According to Menendez et al. the fitting parameter γ should take care of penalizing the mixing between current density components which belong to different directions [dPMHA⁺97].

In this section the general case for arbitrary positive W_{ij}^{rs} will be covered. In the next section WROP is proposed for reducing the mixing of signals which belong to different brain regions. This will induce special settings of W_{ij}^{rs} .

Because WROP handles the ill-posed biomagnetic inverse problem, an appropriate regularization has also to be an essential part of this method. For this, another term is added to the cost function [dPMHA⁺97]

$$s_\alpha(R) = \sum_{i,k,r,s=1}^{N_s, N_s, 3, 3} W_{ik}^{rs} (R_{ik}^{rs} - \delta_{ik}^{rs})^2 + \alpha \sum_{i,l,r=1}^{N_s, N_d, 3} (G_{il}^r)^2 \quad (4.32)$$

Here α again is a regularizing parameter tuning the tradeoff between the minimization of both terms. The cost function $s_\alpha(R)$ is brought into form $s_\alpha(G)$ which directly yields the wanted inverse

mapping G at its minimum:

$$\begin{aligned}
s_\alpha(G) &= \sum_{i,k,r,s=1}^{N_s, N_s, 3, 3} W_{ik}^{rs} \left(\sum_{l=1}^{N_d} G_{il}^r \Phi_{lk}^s - \delta_{ik}^{rs} \right)^2 + \alpha \sum_{i,l,r=1}^{N_s, N_d, 3} (G_{il}^r)^2 \\
&= \sum_{i,k,r,s=1}^{N_s, N_s, 3, 3} \left(W_{ik}^{rs} \left(\sum_{l=1}^{N_d} G_{il}^r \Phi_{lk}^s \right)^2 - 2 W_{ik}^{rs} \left(\sum_{l=1}^{N_d} G_{il}^r \Phi_{lk}^s \right) \delta_{ik}^{rs} + \delta_{ik}^{rs} W_{ik}^{rs} \right) + \alpha \sum_{i,l,r=1}^{N_s, N_d, 3} (G_{il}^r)^2 \\
&= \sum_{i,k,r,s=1}^{N_s, N_s, 3, 3} W_{ik}^{rs} \left(\sum_{l=1}^{N_d} G_{il}^r \Phi_{lk}^s \right)^2 - 2 \sum_{i,r=1}^{N_s, 3} W_{ii}^{rr} \sum_{l=1}^{N_d} G_{il}^r \Phi_{li}^r + \sum_{i,r=1}^{N_s, 3} W_{ii}^{rr} + \alpha \sum_{i,l,r=1}^{N_s, N_d, 3} (G_{il}^r)^2
\end{aligned}$$

The first term in this equation can be written as:

$$\begin{aligned}
\sum_{i,k,r,s=1}^{N_s, N_s, 3, 3} W_{ik}^{rs} \left(\sum_{l=1}^{N_d} G_{il}^r \Phi_{lk}^s \right)^2 &= \sum_{i,k,r,s=1}^{N_s, N_s, 3, 3} W_{ik}^{rs} \sum_{l=1}^{N_d} G_{il}^r \Phi_{lk}^s \sum_{l'=1}^{N_d} G_{il'}^r \Phi_{l'k}^s \\
&= \sum_{i,l,r=1}^{N_s, N_d, 3} G_{il}^r \sum_{k,l',s=1}^{N_s, N_d, 3} W_{ik}^{rs} \Phi_{lk}^s \Phi_{l'k}^s G_{il'}^r \\
&= \sum_{i,l,r=1}^{N_s, N_d, 3} G_{il}^r \sum_{l'}^{N_d} S_{ll'}^{ir} G_{il'}^r \quad \text{with} \\
S_{ll'}^{ir} &= \sum_{k,s=1}^{N_d, 3} W_{ik}^{rs} \Phi_{lk}^s \Phi_{l'k}^s
\end{aligned} \tag{4.33}$$

For s_α this delivers

$$\begin{aligned}
s_\alpha(G) &= \sum_{i,l,r=1}^{N_s, N_d, 3} G_{il}^r \sum_{l'=1}^{N_d} S_{ll'}^{ir} G_{il'}^r - 2 \sum_{i,r=1}^{N_s, 3} W_{ii}^{rr} \sum_{l=1}^{N_d} G_{il}^r \Phi_{li}^r + \sum_{i,r=1}^{N_s, 3} W_{ii}^{rr} + \alpha \sum_{i,l,r=1}^{N_s, N_d, 3} (G_{il}^r)^2 \\
&= \sum_{i,r=1}^{N_s, 3} \left(\sum_{l=1}^{N_d} G_{il}^r \sum_{l'=1}^{N_d} S_{ll'}^{ir} G_{il'}^r - 2 W_{ii}^{rr} \sum_{l=1}^{N_d} G_{il}^r \Phi_{li}^r + W_{ii}^{rr} \right) + \alpha \sum_{i,l,r=1}^{N_s, N_d, 3} (G_{il}^r)^2
\end{aligned}$$

The desired coefficients G_{il}^r are now be obtained by setting $\frac{\partial s_\alpha}{\partial G_{il}^r} = 0$. After a few simple transformations this leads to

$$\sum_{l'=1}^{N_d} (S_{ll'}^{ir} + \delta_{ll'} \alpha) G_{il'}^r = W_{ii}^{rr} \Phi_{li}^r \tag{4.34}$$

which is in matrix notation

$$(S^{ir} + \alpha I) G_{i \cdot}^r = W_{ii}^{rr} \Phi_{\cdot i}^r \tag{4.35}$$

$(G_{i \cdot}^r)^T$ is a row vector of matrix G , and $\Phi_{\cdot i}^r$ is a column vector of the lead field matrix Φ . Finally is

$$G_{i \cdot}^r = W_{ii}^{rr} (S^{ir} + \alpha I)^{-1} \Phi_{\cdot i}^r \tag{4.36}$$

What is the relationship between WROP and the Tikhonov regularization? For the special case $W_{ij}^{rs} = \beta$, i.e. constant weighting of costs for components of the resolution matrix in equation 4.32, formula 4.36 together with definition 4.33 can be written as

$$\begin{aligned} G_i^r &= \beta \left(\beta \Phi \Phi^T + \alpha \mathbf{1} \right)^{-1} \Phi_i^r \\ &= \left(\Phi \Phi^T + \frac{\alpha}{\beta} \mathbf{1} \right)^{-1} \Phi_i^r \end{aligned}$$

Transposing both sides gives

$$(G_i^r)^T = (\Phi_i^r)^T \left(\Phi \Phi^T + \frac{\alpha}{\beta} \mathbf{1} \right)^{-1} \quad (4.37)$$

and for matrix G

$$G = \Phi^T \left(\Phi \Phi^T + \frac{\alpha}{\beta} \mathbf{1} \right)^{-1} \quad (4.38)$$

Please note that this is the Minimum Norm solution (equation 2.14 with $L = 1$) regularized by α , if β is equal to 1 (otherwise α could be rescaled appropriately). Thus the WROP approach is equivalent to the Minimum Norm method, if its weighting coefficients W_{ij}^{rs} in the cost function 4.32 are identical [dPMHA+97].

But in chapter 3 it has been shown that the MN method is not capable to reconstruct current sources which are situated deeper in the source space in a satisfying manner. Because the WROP approach is equivalent to the Minimum Norm method in the limit of $W_{ij}^{rs} = \beta$, the presumption is obvious that this method also struggles in reconstructing deeper sources. This will be demonstrated at the end of this chapter.

In this work the WROP approach is improved in order to recover also deeper sources. For this it will be proved that the extended approach is equivalent to the *weighted* Minimum Norm solution in the limit of constant coefficients $W_{ij}^{rs} = \beta$.

The starting point for the extension of WROP is again the connection between the estimated and the original current density distribution

$$\vec{\tilde{j}} = G \vec{m} = G \Phi \vec{j} \quad (4.39)$$

Let us now combine this equation with an arbitrary depth weighting matrix L from the Tikhonov regularization (equation 2.12)

$$L \vec{\tilde{j}} = LG \Phi L^{-1} L \vec{j} \quad (4.40)$$

The *transformed current density distribution* $\vec{\tilde{j}}$ and the *transformed lead field matrix* $\tilde{\Phi}$ are now defined by $\vec{\tilde{j}} = L \vec{j}$ and $\tilde{\Phi} = \Phi L^{-1}$, respectively, which gives

$$\vec{\tilde{j}} = \tilde{G} \tilde{\Phi} \vec{\tilde{j}} = \tilde{G} \Phi \vec{j} = \tilde{G} \vec{m} \quad (4.41)$$

if $\tilde{G} = LG$ and $\vec{\tilde{j}} = L \vec{j}$. The new approach is now introduced by considering matrix $\tilde{G} \tilde{\Phi}$ as a *transformed resolution matrix* \tilde{R} . The requirement for the wanted matrix \tilde{G} (which gives matrix

G via inverting $\tilde{G} = LG$) is, that matrix \tilde{R} is as close as possible to the unity matrix. Analogous to equation 4.32 a cost function for \tilde{R} is now defined by:

$$s_\alpha(\tilde{R}) = \sum_{i,k,r,s=1}^{N_s, N_s, 3, 3} W_{ik}^{rs} (\tilde{R}_{ik}^{rs} - \delta_{ik}^{rs})^2 + \alpha \sum_{i,l,r=1}^{N_s, N_l, 3} (\tilde{G}_{il}^r)^2 \quad (4.42)$$

Analogous to the derivation of equation 4.36, the minimization of $s_\alpha(\tilde{R})$ leads to

$$\tilde{G}_i^r = W_{ii}^{rr} (\tilde{S}^{ir} + \alpha \mathbf{1})^{-1} \tilde{\Phi}_i^r \quad (4.43)$$

with $\tilde{S}_{ll'}^{ir} = \sum_{k,s} W_{ik}^{rs} \tilde{\Phi}_{lk}^s \tilde{\Phi}_{l'k}^s$. With $\tilde{G} = LG$ this give the inverse mapping in equation 4.39 for the extended WROP approach.

In the following it will be proved that this new approach is equivalent to the corresponding weighted Minimum Norm solution in the limit of $W_{ik}^{rs} = \beta = \text{const.}$ First, in this special case the matrices \tilde{S}^{ir} obey

$$\tilde{S}^{ir} = \beta \tilde{\Phi} \tilde{\Phi}^T = \beta \Phi L^{-1} (L^{-1})^T \Phi^T \quad (4.44)$$

and analogous to the common WROP approach (see derivation of equation 4.38)

$$\tilde{G} = \tilde{\Phi}^T \left(\Phi L^{-1} (L^{-1})^T \Phi^T + \frac{\alpha}{\beta} \mathbf{1} \right)^{-1} \quad (4.45)$$

With this, it follows for the transformed current density distribution in equation 4.41

$$\tilde{j} = \tilde{\Phi}^T \left(\Phi (L^T L)^{-1} \Phi^T + \frac{\alpha}{\beta} \mathbf{1} \right)^{-1} \vec{m} \quad (4.46)$$

Using the definitions for \tilde{j} and $\tilde{\Phi}$ this can be written as

$$L \hat{j} = (L^{-1})^T \Phi^T \left(\Phi (L^T L)^{-1} \Phi^T + \frac{\alpha}{\beta} \mathbf{1} \right)^{-1} \vec{m} \quad (4.47)$$

This means for the reconstructed current density distribution

$$\begin{aligned} \hat{j} &= L^{-1} (L^{-1})^T \Phi^T \left(\Phi (L^T L)^{-1} \Phi^T + \frac{\alpha}{\beta} \mathbf{1} \right)^{-1} \vec{m} \\ &= (L^T L)^{-1} \Phi^T \left(\Phi (L^T L)^{-1} \Phi^T + \frac{\alpha}{\beta} \mathbf{1} \right)^{-1} \vec{m} \end{aligned}$$

This corresponds to the description of the estimated current density distribution according to the weighted Minimum Norm solution (equation 2.14).

This new approach, which is an extended form of WROP, which includes a depth weighting, will be called *preweighted WROP* (pWROP) in the following. In the next sections SOFIA, WROP, and pWROP will be compared in the same framework, i.e. the reduction of contamination between signals originating from a predefined region of interest and the remaining source space.

4.3 Tests concerning the ability of brain region localization

In the preceding sections distributed source models have been presented which exploit an additional constraint compared to the methods shown in chapter 3. SOFIA tries to focus on a region of interest. This region of interest has to be predefined by the user. In practice this could be e.g. a brain region, which is objectively identified via *brain maps* [ZSPGA02]. These are anatomically separated areas of the brain which take different roles in complex tasks like visual signal processing, for example. In order to discriminate these roles with the aid of MEG experiments, it is very important to reduce artificial superposition of current densities from different regions induced by the reconstruction process.

A further important class of applications, which would benefit from this, are neurofeedback studies. Neurofeedback is the topic of interest in the following chapters. In such experiments activity from specific brain regions is fed back to the subject. For this it is highly of interest to produce reconstructed current densities which are contaminated as little as possible.

The idea in SOFIA is to reduce the mixing of signals from outside the region of interest into the ROI by using virtual sensors which are highly sensitive only inside the region of interest. In WROP, on the other hand, it is derived a linear inverse mapping between the original and reconstructed current density distribution from the minimum of a weighted cost function. This cost function measures the difference between the actual mapping and the identity function.

As SOFIA, WROP, and pWROP result in linear reconstruction methods, all these methods deliver a resolution matrix:

$$\hat{j}_i^r = \sum_{k,s=1}^{N_s,3} R_{ik}^{rs} j_k^s \quad (4.48)$$

The aim they have in common is building their resolution matrices in such a way that optimally reduces the mixing between specific voxels. For SOFIA this choice of voxels is done by the definition of the region of interest. Specifying WROP and pWROP by defining their associated weighting coefficients gives a much more general concept.

Because the separation of brain regions concerning the reconstructed current density distribution is of great practical relevance, WROP and pWROP will be specified with respect to this aim in the next section. In a joint benchmark based on numerical simulations all methods discussed in this section will be investigated concerning their ability to reduce the contamination between the predefined regions.

4.3.1 Adjusting methods

The head-sensor-configuration which underlies the simulations discussed in the following is identical to that already used in chapter 3. The source space again is given by a spherical segment fitted to the back of the head. Large parts of the cortex in this area can be activated by visual stimulation and are therefore belong to the *visual cortex* [ZSPGA02]. A region of interest has been predefined. This is a sphere inside the source space with a radius of 1.5 cm. The chosen sphere (see also figure 4.2) embraces the left visual cortex area 5 (V5) which is known to be an important current generator in the brain during visual signal processing [BAD⁺05].

For WROP as well as pWROP their weighting coefficients have been adjusted, in order to focus

on the region of interest, in the following way:

$$W_{ik}^{rs} = \begin{cases} 1 & : \text{ if ((voxel i and voxel k belong to the ROI) or} \\ & : \text{ (voxel i and voxel j are outside the ROI))} \\ \beta & : \text{ otherwise} \end{cases} \quad (4.49)$$

Here $\beta > 1$ is a parameter which determines the strength of the condition. By this constraint, in the cost functions 4.32 and 4.42 terms are stronger penalized for specific entries in the resolution matrix. Such entries that are responsible for the contamination of current densities originating from different areas, the ROI on the one hand and the remaining source space on the other hand, are stronger punished. This should result in a decreased mixing of these current densities in the reconstruction process. In other words, a better separation between activity inside the ROI and inside the rest of the source space is expected.

As explained in the preceding section, in a certain sense WROP and pWROP are based on the Minimum Norm and weighted Minimum Norm solutions. These are given by setting $\beta = 1$ in the definition of W_{ik}^{rs} in 4.49. In general, the purpose of the additional constraint in WROP and pWROP is to manipulate the resolution kernels (rows of the resolution matrix) in a way that reduces mixing effects. It can be shown that for $\beta > 1$ in equation 4.49 the diagonal of the resulting resolution matrix is not the same referring to the corresponding (weighted) Minimum Norm solutions, i.e. for $\beta = 1$. This has an undesired effect on the columns of the resolution matrix. These determine the reconstructed current density distribution for single current dipoles, which point in one of the three space directions. If constraint 4.49 is applied on its own for $\beta > 1$, single dipole reconstructions would exhibit an overemphasized activity outside the region of interest. Restoring the diagonal elements of the corresponding (weighted) Minimum Norm solutions (called $R_{ii,\beta=1}^{rr}$ in the following) by an appropriate normalization of each resolution kernel solves this problem. For the WROP method let $G_{il,\beta>1}^r$ denote the intermediate coefficients after applying the definition for W_{ik}^{rs} in 4.49 in equation 4.36 before the following normalization procedure. The intermediate coefficients for pWROP are given by the corresponding equation 4.43 together with $\tilde{G} = LG$. Furthermore $R_{ii,\beta>1}^{rr}$ are the diagonal elements of the intermediate resolution matrix without normalization, which are extracted from

$$R_{ik,\beta>1}^{rs} = \sum_{l=1}^{N_d} G_{il,\beta>1}^r \Phi_{lk}^s \quad (4.50)$$

The matrix G , which determines the inverse mapping according to equation 4.25 and equation 4.39, respectively, is defined as:

$$G_{il}^r = \frac{G_{il,\beta>1}^r}{R_{ii,\beta>1}^{rr}} R_{ii,\beta=1}^{rr} \quad (4.51)$$

After this normalization the diagonal elements of the final resolution matrix are equal to $R_{ii,\beta=1}^{rr}$. Its entries $R_{ik}^{rs} = \sum_{l=1}^{N_d} G_{il}^r \Phi_{lk}^s$ for a fixed row given by indices i and r are scaled by the same factor compared to the corresponding entries of the intermediate resolution matrix. Thus the shape of the profile of each resolution kernel, which had been constructed by exploiting constraint 4.49, is not affected by the normalization.

The same depth weighting defined by matrix L for SOFIA as well as pWROP has been chosen

as for the GaussMN method (section 3.1.1). This Gaussian profile delivered a convincing performance in the benchmark discussed in the preceding chapter, in order to recover also deeper sources. Thus, by this definition of their depth weighting SOFIA and pWROP are identical to the GaussMN method for their limit cases ($N_f = N_d$ for SOFIA and $\beta = 1$ for pWROP), if all these methods are used with the same regularization.

Concerning an appropriate regularization the results from the preceding chapter are again useful. Both SOFIA and pWROP are regularized by a fixed setting of their regularization parameter α in formula 4.43 and 4.23, respectively, whose values can be gathered from GaussMN in table 3.1. Analogous, the used setting of α for WROP in equation 4.36 is the one found in the tests of the MN method (also table 3.1).

In the following section, first the virtual lead fields in SOFIA are investigated for the introduced configuration. Afterwards, noise-free reconstructions of single current dipoles situated outside and inside the region of interest are shown for WROP, pWROP, SOFIA, and also in comparison for GaussMN. Moreover, the resulting resolution matrices of these methods are evaluated in a quantitative manner.

4.3.2 Results

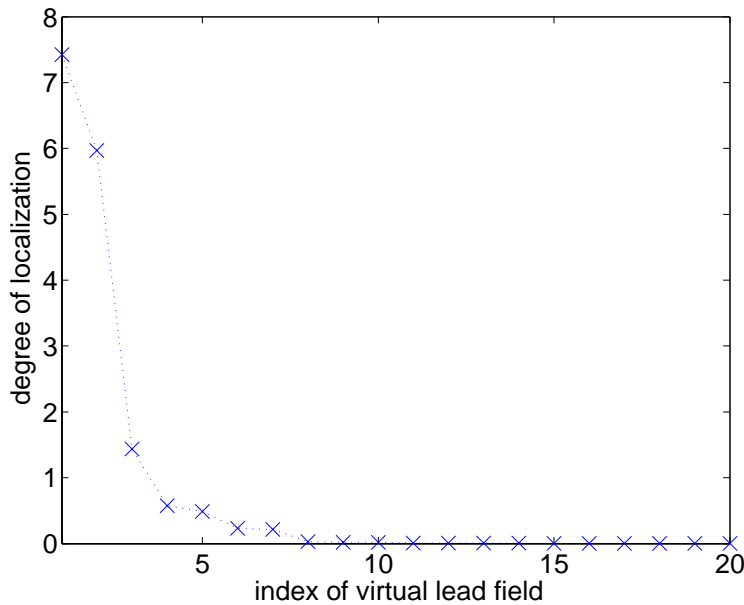


Figure 4.1: Degree of localization l_i of the virtual lead fields in SOFIA (equation 4.7). Only values for the first 20 virtual lead fields are shown. The remaining ones exhibited values close to 0.

For SOFIA in figure 4.1 the degree of localization is plotted for the twenty virtual lead fields which are localized strongest inside the ROI among all 90 virtual lead fields. Only three virtual lead fields show values larger than 1, i.e. only three virtual sensors have a larger mean sensitivity inside the region of interest than outside (formula 4.7). Most of them are much more sensitive outside the ROI. These relatively low values for the degree of localization have also been ob-

served for other choices of the ROI using different sizes and positions (not shown here). Thus, the concept of SOFIA of using only virtual sensors which are strongly localized inside the ROI is problematic in practice, in first place because its algorithm delivers only a few such sensors. But the less sensors are used for the reconstruction, the lower is the achieved localization of sources inside the ROI [BGLI99].

Exemplary reconstructions of a current dipole are presented in figure 4.2. The single source is situated inside the region of interest whose boundary is indicated by a green circle in the images. For all tested methods the strength, orientation, and position of the original current dipole is the same. For comparison, results from the GaussMN method are included. Its reconstructed current density distribution shows significant spreading of activity outside the ROI. In experiments, this effect would make it rather difficult to uniquely identify the ROI as the only activated brain region. Using only the 3 strongest localized virtual sensors in SOFIA, its reconstructed current density distribution exhibits a slightly lowered blurring compared to the GaussMN solution. Taking into account more than 5 virtual sensors for the reconstruction destroys this more focal reconstruction as other simulations have shown. This is understandable considering their degrees of localization, because in this case virtual sensors are used with very low sensitivity inside the region of interest (figure 4.1). For their associated virtual lead fields this means that they are very spreaded outside the region of interest. Because the reconstructed current distribution is a superposition of all applied virtual lead fields 4.11, it gets also more spreaded outside that region. Using fewer than 3 virtual sensors for SOFIA improves the effect of reducing the reconstructed activity outside the ROI, but not in a drastic manner. The reconstructed current density distribution is much more concentrated inside the ROI by using WROP or pWROP presented here for $\beta = 10$. The size of this effect can be tuned by the constraint parameter β (equation 4.49) as will be demonstrated at the end of the section. What can also be observed in figure 4.2 with respect to WROP is, that most of its reconstructed activity is present in the superficial area due to the lacking depth weighting in WROP.

Figure 4.3 shows representative results of single dipole reconstructions whereby the current dipole is placed outside the ROI this time. Again the same current dipole is reconstructed by SOFIA, GaussMN, WROP, and pWROP. As expected SOFIA is not able to localize the original position of the dipole. Its reconstructed current distribution, whose profile is very similar to that in figure 4.2 by SOFIA, is focused inside the region of interest. This is not surprising, because the three applied virtual lead fields are mainly concentrated inside the region of interest. In contrast to the implemented versions of WROP and pWROP, SOFIA is not designed for the purpose of giving sensible information about current dipoles situated outside the ROI. The current density distribution in figure 4.3 reconstructed by WROP demonstrates the need of a depth weighting: the main activity is focused superficially being far away from the actual position of the dipole. pWROP is the only method among the tested inverse techniques which is able to localize the current dipole accurately outside the ROI and simultaneously avoids undesired projections of activity inside the region of interest.

SOFIA, WROP, and pWROP produce a tradeoff between their localization accuracy and the reduction of cross-contamination in the reconstructed current density distribution between the predefined brain regions. In order to investigate the dependence of the setting of the constraint parameters on the localization error, single current dipoles with different positions and orientations as in the single dipole tests in section 3.3.1 have been reconstructed. For the same location

SOFIA		WROP		pWROP	
N_f	mean loc. error in cm	β	mean loc. error in cm	β	mean loc. error in cm
30	1.5	2	2.3	2	1.1
10	4	5	2.3	5	1.1
5	5.4	10	2.4	10	1.3
3	6.1	100	2.6	100	2.1
2	6.1				
1	6.1				

Table 4.1: Mean localization error of single dipole reconstructions for SOFIA, WROP, and pWROP in the absence of detector noise. The displacement has been averaged with respect to the entire source space.

and shape of the ROI described above the position of the single current dipole has been varied across the entire source space between the simulations. Three different orientations of the dipole have been tested for each grid point. The mean localization errors for different values of the number of used virtual lead fields N_f for SOFIA and different values of β for WROP and pWROP are presented in table 4.1. The mean displacement for the limit case of SOFIA ($N_f = N_d = 90$) and pWROP ($\beta = 1$) amounted to 1.0 cm (GaussMN results in table 3.1). Using many virtual sensors in SOFIA, most of which are not very sensitive inside the ROI (figure 4.1), means a significant increase of the localization error. It rises monotonically for decreasing values of N_f . The mean localization error for WROP exhibits a very large value for $\beta = 1$ (2.2 cm: see results for MN in table 3.1) due to the missing depth weighting. For $\beta \leq 10$ the increase of the mean localization error is not severe (≤ 2 mm). pWROP also shows just a slight increase of the displacement by increasing β , but its corresponding absolute values for the mean localization error are much lower due to the applied Gaussian weighting profile.

The purpose of the measures defined in the following is to quantify the degree of contamination between voxels inside and outside the ROI introduced by each reconstruction method. They refer to the amount of mixing given by the resolution kernels (rows of the resolution matrix) on one hand and given by the point spread functions (columns of the resolution matrix) on the other hand. The final set of measures derived in the following paragraphs will take into account the complete resolution matrix for each reconstruction method.

For this, first

$$I_i^r = \sum_{s,j}^{3,N_{ROI}} \frac{|R_{ij}^{rs}|}{3N_{ROI}} \quad (4.52)$$

gives the average absolute value over all voxels inside the ROI of each resolution kernel responsible for an arbitrary voxel i and direction r . The summation via index j runs over all grid points inside the region of interest (N_{ROI} : number of grid points inside ROI). Analogous

$$O_i^r = \sum_{s,j}^{3,N_{SS/ROI}} \frac{|R_{ij}^{rs}|}{3N_{SS/ROI}} \quad (4.53)$$

measures the mean sensitivity of this resolution kernel with respect to the area outside the region of interest which is denoted by SS/ROI ($N_{SS/ROI}$: number of grid points outside ROI).

For all resolution kernels which are responsible for the reconstructed current density in voxels i of the ROI, their mean relative sensitivity is defined by

$$k_{ROI} = \frac{1}{3N_{ROI}} \sum_{r,i}^{3,N_{ROI}} \frac{\mathcal{I}_i^r}{\mathcal{O}_i^r} \quad (4.54)$$

This measure gives the mean sensitivity inside the ROI compared to the mean sensitivity outside, which is averaged over all resolution kernels for voxels inside the region of interest. Reconstruction methods with kernels which exhibit a strong reduction of the contamination inside the ROI from voxels outside give large values for k_{ROI} . A strong mixing produces lower values.

For the resolution kernels which are responsible for the reconstructed current density in voxels i outside the ROI an analogous measure is defined via

$$k_{SS/ROI} = \frac{1}{3N_{SS/ROI}} \sum_{r,i}^{3,N_{SS/ROI}} \frac{\mathcal{O}_i^r}{\mathcal{I}_i^r} \quad (4.55)$$

If the kernels for voxels outside the ROI are strongly contaminated with respect to voxels inside the region of interest, this measure shows lower values than for such kernels with reduced mixing between these areas.

These measures enable to discriminate the reconstruction methods with respect to their degree of contamination in their kernels between the ROI and rest of the source space. Corresponding quantities are useful to measure the quality of the pointspread functions. What has to be changed compared to definitions 4.52 and 4.53, is summing over the rows of the resolution matrix instead of the columns. Please let us consider a pointspread function which determines the reconstructed current density distribution induced by a point source in voxel i with current density larger than 0 only in its r -th component. For this, the following measures are obtained:

$$\mathcal{J}_i^r = \sum_{s,j}^{3,ROI} \frac{|R_{ji}^{sr}|}{3N_{ROI}} \quad (4.56)$$

$$\mathcal{P}_i^r = \sum_{s,j}^{3,SS/ROI} \frac{|R_{ji}^{sr}|}{3N_{SS/ROI}} \quad (4.57)$$

For reconstructed current density distributions of point sources inside the ROI like in figure 4.2, which exhibit low spreading outside the region of interest, the ratio of \mathcal{J}_i^r and \mathcal{P}_i^r is large. If the point source is situated outside the ROI like in figure 4.3 and few activity is projected inside the region of interest, in this case the ratio of its corresponding quantities \mathcal{P}_i^r and \mathcal{J}_i^r is large.

These sensitivity measures for a specific column of the resolution matrix are analogous summarized across all point spread functions for voxels i belonging to the ROI by applying

$$p_{ROI} = \frac{1}{3N_{ROI}} \sum_{r,i}^{3,N_{ROI}} \frac{\mathcal{J}_i^r}{\mathcal{P}_i^r} \quad (4.58)$$

and for voxels i belonging to the remaining source space by

$$p_{SS/ROI} = \frac{1}{3N_{SS/ROI}} \sum_{r,i}^{3,N_{SS/ROI}} \frac{\mathcal{P}_i^r}{\mathcal{J}_i^r} \quad (4.59)$$

In table 4.2 the resulting values for the measures k_{ROI} , $k_{SS/ROI}$, p_{ROI} , and $p_{SS/ROI}$ are presented.

	k_{ROI}	$k_{SS/ROI}$		p_{ROI}	$p_{SS/ROI}$
GaussMN	3.72	2.46	GaussMN	3.42	2.57
SOFIA			SOFIA		
$N_f=30$	3.72	1.65	$N_f=30$	3.42	1.77
10	3.73	0.68	10	3.42	0.75
5	3.87	0.32	5	3.55	0.34
3	3.98	0.27	3	3.64	0.29
2	4.16	0.24	2	3.78	0.26
1	4.46	0.22	1	4.17	0.24
WROP			WROP		
$\beta=2$	3.63	2.33	$\beta=2$	3.67	2.50
5	3.97	2.93	5	4.57	3.09
10	4.17	3.58	10	5.59	3.50
100	4.50	6.19	100	9.52	4.71
pWROP			pWROP		
$\beta=2$	4.03	2.84	$\beta=2$	3.92	2.98
5	4.35	3.70	5	5.10	3.56
10	4.52	4.61	10	6.39	4.00
100	4.85	8.09	100	11.49	5.18

Table 4.2: Values for the degree of mixing between voxels inside and outside the ROI for different reconstruction methods and settings of their constraint parameter. The measures refer to the resolution kernels (left table) and to the point spread functions (right table), respectively.

For all measures larger values show a reduced contamination. SOFIA, WROP, and pWROP have been tested with the same settings of their constraint parameters N_f and β as in the investigations of the mean localization error (table 4.1). In addition, the GaussMN method has been included in the test.

With respect to its resolution kernels as well as its point spread functions SOFIA exhibits a decreased mixing of activity from outside the ROI in the region of interest. These mixing effects, indicated by the measures k_{ROI} and p_{ROI} , are reduced monotonically with a decreasing number of applied virtual lead fields. As expected the values for $k_{SS/ROI}$ and $p_{SS/ROI}$ confirm that the current density distribution outside the region of interest is not reconstructed in a sensible manner by SOFIA.

The WROP method gives better values for all measures as compared to GaussMN for $\beta \geq 5$. This indicates that the constraint of WROP in combination with the applied normalization of its kernels introduced in the preceding section is able to reduce mixing effects between a region of interest and the rest of the source space. Please note that in contrast to SOFIA this refers to both directions, i.e. the reconstructed current density inside the ROI is less contaminated by activity outside and vice versa.

pWROP is able to improve this effect significantly due to its depth weighting. For example a setting of $\beta = 10$ which induces only a small increase of the mean localization error compared to $\beta = 1$ (3 mm) improves k_{ROI} by more than 10 %, and $k_{SS/ROI}$ by more than 85 % compared to GaussMN. With respect to the point spread functions this means an increase of 87 % found for p_{ROI} and 56 % found for $p_{SS/ROI}$. These values are larger than those found for WROP as well as all corresponding values found for SOFIA. The mixing between activity inside and outside the ROI by the reconstruction process monotonically increases for larger values of β .

The shape of that resolution kernel is exemplarily presented in figure 4.4 which determines the current density in y -direction reconstructed in the ROI sphere center by different methods. The applied methods are GaussMN, SOFIA ($N_f = 1$), WROP ($\beta = 100$), and pWROP ($\beta = 100$). The graphs look very irregular because of the anisotropic shape of the resolution kernels.

The resolution kernel shows the significance of the mixing effect induced by the reconstruction. Most voxels affect the reconstructed current density at the ROI sphere center severely. Even the position of the maximum of the curve is not at the center of the sphere where it would be for an ideal resolution kernel. Its distance to the center of the ROI sphere is shifted by more than 1.5 cm for the resolution kernel produced by GaussMN, so that the maximum is actually situated outside the region of interest. Using SOFIA with only that virtual sensor, whose degree of localization is largest (equation 4.7), even enhances the mixing effect in this example. This is shown by the increased spreading of its resolution kernel outside the ROI in figure 4.4. This example demonstrates in an extreme way, that SOFIA cannot be recommended for usage. WROP and pWROP however are able to reduce the mixing for $\beta = 100$ considerably: The integral over the region of interest (distance smaller or equal than 1.5 cm) under their curves relative to the integral outside the ROI is significantly larger than the corresponding ratio for GaussMN. In this example this ratio for pWROP is 1.4 larger than for GaussMN.

Among the tested distributed source models that try to reduce the mixing between predefined brain regions with respect to the reconstructed current densities, pWROP shows the best performance. The tradeoff between the localization accuracy and the separation of the regions is set by the constraint parameter β . A significant decrease of the cross-contamination is given already for $\beta = 10$ which costs only an increase of 3 mm concerning the mean displacement error for single sources. Other tested region of interests than shown here gave similar results. pWROP is a considerable improvement compared to WROP. Not only are deeper sources reconstructed in a better way resulting in an increased localization accuracy on average. The additional depth weighting chosen by the user also helps to reduce the contamination effects compared to WROP for the same setting of their constraint parameter β . This refers to the resolution kernels as well as to the point spread functions. pWROP should also be extended in tests by using the standardization of sLORETA (equation 3.6). Moreover detector noise should be taken into account. Concerning applications pWROP is very useful in the tested setup, if brain regions are predefined with the aid of brain maps [ZSPGA02]. Its concept is very flexible with respect to the choice of its depth weighting as well as its own weighting coefficients used in the cost function 4.42. Using SOFIA to improve the reconstructed signals inside the region of interest is very questionable in the light of the obtained results.

In the next chapter an application of realtime MEG is studied first in a theoretical manner. Feedback techniques to desynchronize ensembles of neural oscillators are investigated. The special-

ized distributed source models introduced in this chapter are tested concerning their benefit in such a scenario in section 5.2.

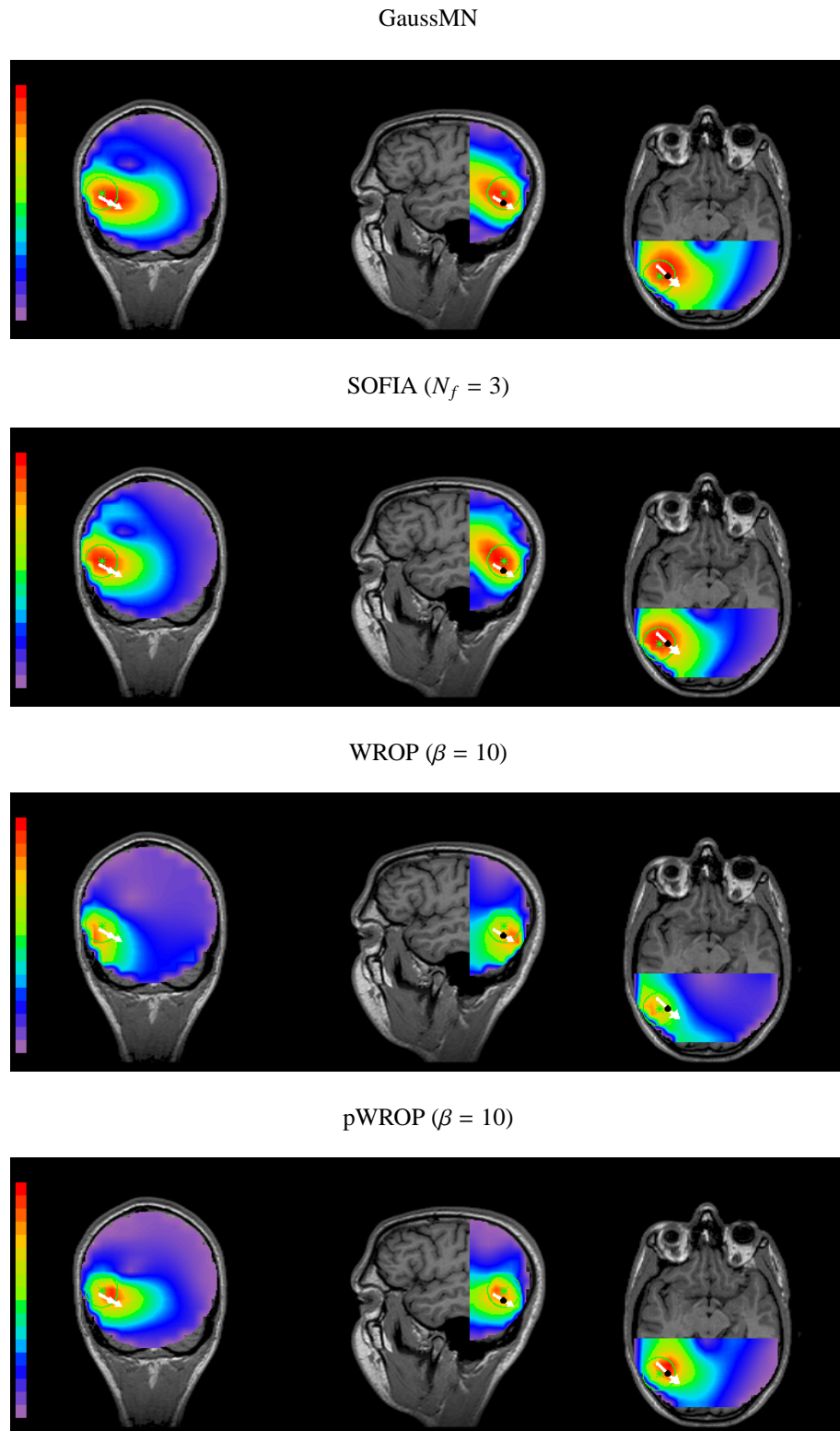


Figure 4.2: Exemplary reconstructions of a single current dipole situated *inside* the ROI (green circle) in the absence of detector noise. Used reconstruction method from top to bottom: GaussMN, SOFIA with the aid of 3 virtual sensors, WROP for $\beta = 10$, and pWROP for $\beta = 10$. The joint intersection point of the presented slices for each method is the center of the ROI sphere at $[-7.0 \text{ cm}, -4.4 \text{ cm}, 0.6 \text{ cm}]$. Values range from 0 (purple) to the maximum of the modulus of the current density in each reconstruction (red).

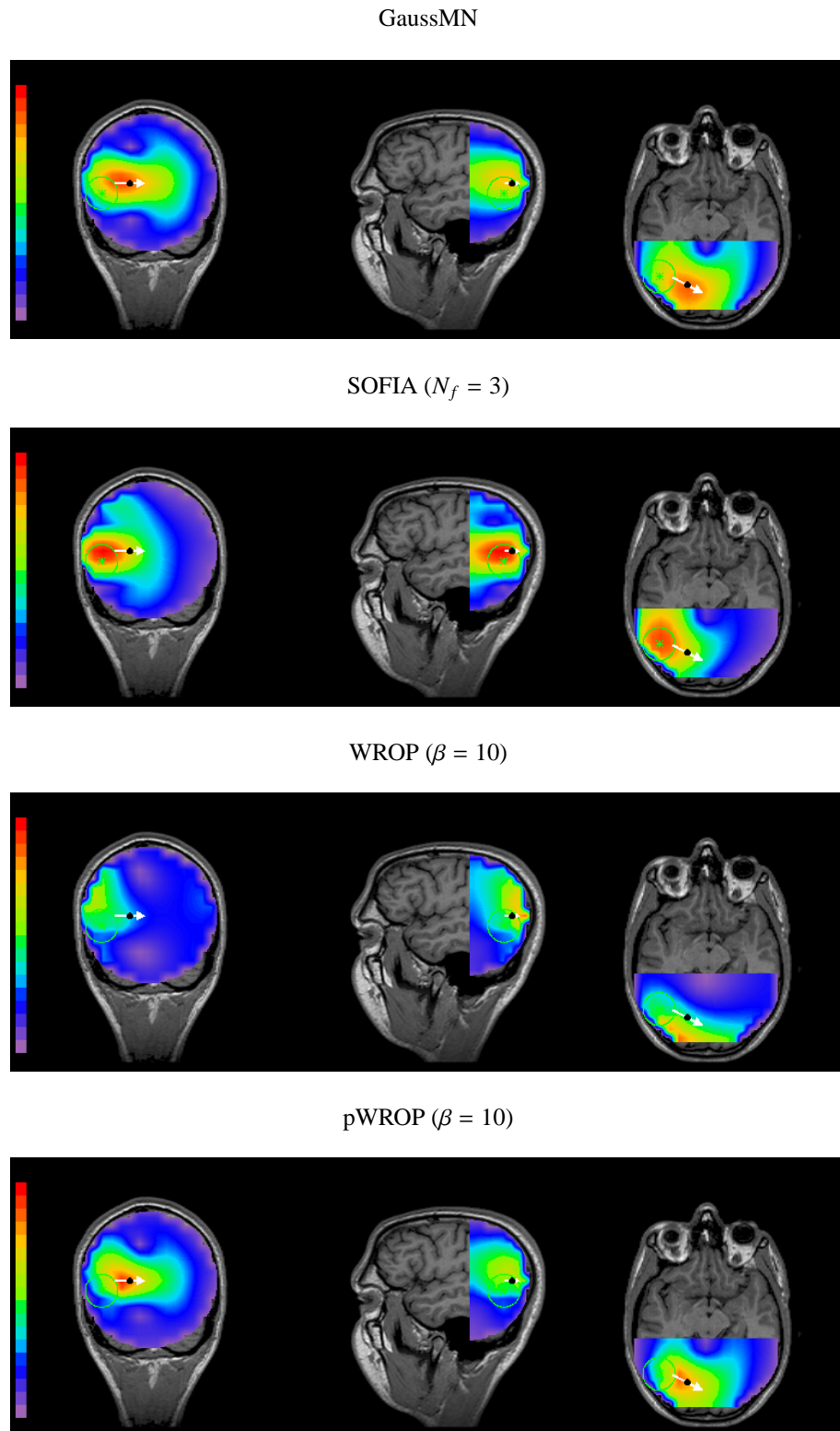


Figure 4.3: Exemplary reconstructions of a single current dipole situated *outside* the ROI (green circle) in the absence of noise. Used reconstruction method from top to bottom: GaussMN, SOFIA with the aid of 3 virtual sensors, WROP for $\beta = 10$, and pWROP for $\beta = 10$. The joint intersection point of the presented slices for each method is the center of the ROI sphere at $[-7.0 \text{ cm}, -4.4 \text{ cm}, 0.6 \text{ cm}]$.

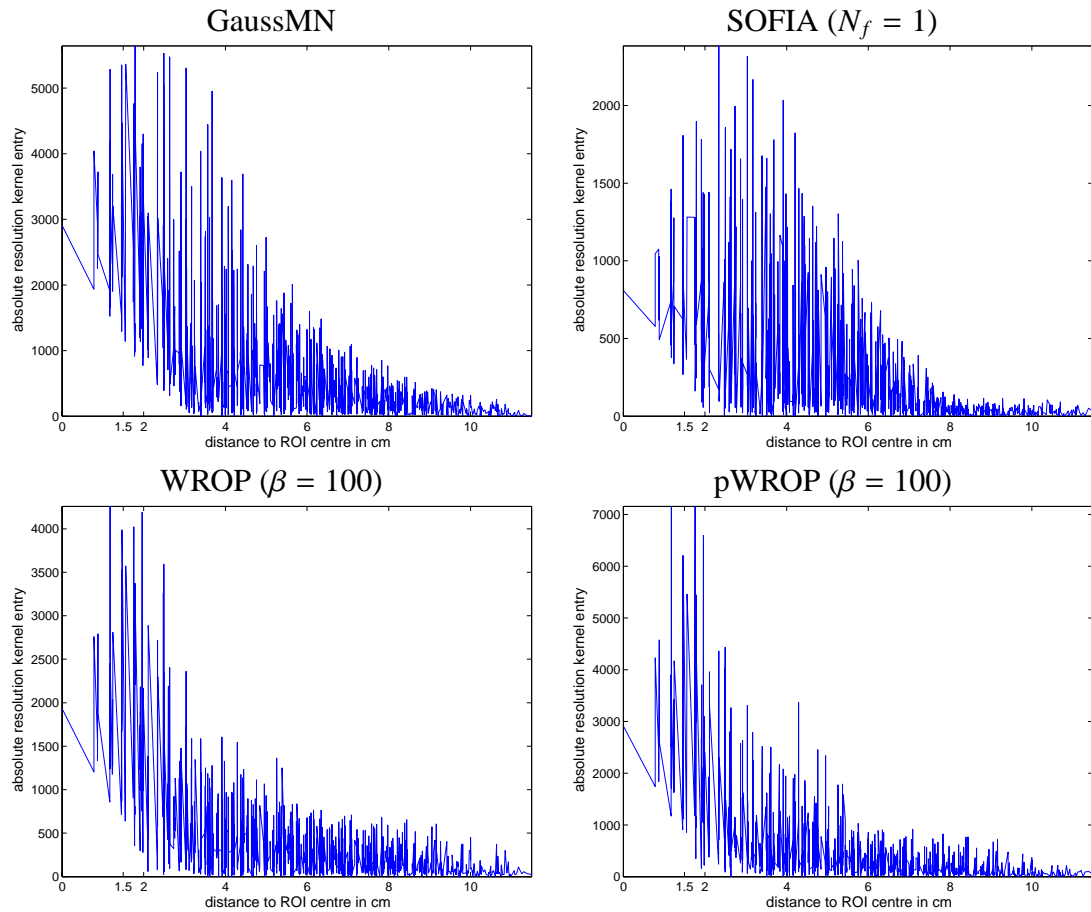


Figure 4.4: Exemplary resolution kernel for GaussMN (top left), SOFIA with only one virtual sensor (top right), WROP with $\beta = 100$ (bottom left), and pWROP also with $\beta = 100$ (bottom right). In all cases the shown kernel determines the reconstructed current density in the ROI center in y -direction. Absolute values of the components of the resolution kernel are plotted versus the distance to the ROI sphere center (radius: 1.5 cm) of the corresponding grid points. The absolute values give the contamination of each grid point in the source space regarding to the reconstructed current density in the sphere center. Only the components which determine the mixing of current densities in the y -direction are presented.

Chapter 5

Desynchronization of neural populations by delayed feedback

So far this work focused on the search for an MEG reconstruction algorithm which makes it possible to acquire information in realtime about the cerebral current densities as accurate as possible. In chapter 3 state-of-the-art candidates have been studied. In the preceding chapter the best linear method from this study, the GaussMN method, has been adjusted in building methods which focus on a region of interest. The most promising technique among these proved to be the pWROP approach. A very relevant application for realtime reconstruction methods is neurofeedback. In the following, the idea is to control synchrony in ensembles of coupled neurons. For this a stimulation signal is constructed with the aid of the measured mean field of the ensemble.

In the field of nonlinear dynamics the impact of delay on oscillating systems led to a number of control protocols [SW89, Pyr92, RJ00, JBS04, BJS04, BJS05, SPA⁺05, PAS05, HS05]. In [BAS⁺02] a systematic comparison of time-delayed feedback schemes is presented for stabilizing time periodic spatial patterns in a reaction-diffusion system with global coupling. See [Sch04] for a review with respect to the stabilization of chaotic spatio-temporal patterns by different delayed feedback techniques in semiconductor models. Delayed feedback control proved also to be useful to shape the regularity of noise-induced oscillations in spatially extended systems with diffusive coupling [SBS06].

Rosenblum et al. [RP04a, RP04b] presented linear feedback control using a stimulation signal

$$S(t) = K\bar{Z}(t - \tau) \quad (5.1)$$

Here K is a parameter which determines the feedback strength, \bar{Z} denotes the analytic (complex) form of the measured mean field of the ensemble of oscillators [PRK01] and τ the time delay of the protocol. Recently Popovych et al. [PHT05b, PHT05a, PHT06a, THP06, PHT06b] constructed a new delayed feedback method by combining nonlinearly the instantaneous analytic signal $\bar{Z}(t)$ with the time delayed analytic signal $\bar{Z}(t - \tau)$

$$S(t) = K\bar{Z}^2(t)\bar{Z}^*(t - \tau) \quad (5.2)$$

whereby the asterisk denotes complex conjugacy. Both techniques are proposed for the suppression of brain rhythms based on physical models of the neural populations. This concept is

pioneered by Tass [Tas01b, Tas01c, Tas01a, Tas02, Tas03, THP06]. As a part of this thesis both protocols have been applied for the first time as neurofeedback in a human subject. This MEG experiment with visual stimulation will be described in the next chapter.

In this chapter the nonlinear delayed feedback method is theoretically studied. First, the ability of the feedback method to desynchronize coupled oscillators is presented with a new aspect which is the influence of a phase shift on the stimulation signal. With respect to applying nonlinear delayed feedback with the aid of MEG data, the mixing of brain signals from different brain areas in the stimulation signal has to be taken into account. Its influence on the feedback performance is investigated in models of coupled limit cycle oscillators. For this, the reconstruction methods introduced in the preceding chapter are used. At the end of this chapter a modified nonlinear delayed feedback protocol, which has been developed as a part of this work, is presented. This method uses the mixing of mean fields from different ensembles, which is unavoidable in MEG data, in a constructive manner. A specific degree of mixing for the calculation of the stimulation signal enhances the desynchronization effect in two interacting ensembles of oscillators, as can be explained.

5.1 Phase shift in nonlinear delayed feedback

Please consider the following ensemble of N globally coupled limit-cycle oscillators:

$$\dot{Z}_j(t) = (a_j + i\omega_j - |Z_j(t)|^2)Z_j(t) + C\bar{Z}(t) + S(t) \quad (5.3)$$

Here $Z_j = x_j + iy_j$ are the complex variables of the individual oscillators and the mean field of the ensemble is given by

$$\bar{Z}(t) := \frac{1}{N} \sum_{j=1}^N Z_j(t) \quad (5.4)$$

Without stimulation ($S = 0$) and without coupling ($C = 0$) each oscillator rotates independently on its limit cycle with its radius $\sqrt{a_j}$ and natural frequency ω_j emerging in a Hopf bifurcation [Str00]. In this case the variance of the mean field fluctuations is of order $N^{-\frac{1}{2}}$ [PRK01]. For increasing coupling strength C all oscillators start to synchronize, i.e. they start to rotate with the same frequency whereby all mutual phase differences decay (mod 2π) [PHT05b].

A global stimulation affecting all oscillators with the same signal and instantaneously is administered by

$$S(t) = Ke^{i\vartheta} \bar{Z}^2(t) \bar{Z}^*(t - \tau) \quad (5.5)$$

With respect to the nonlinear delayed feedback in equation 5.2 an additional factor $e^{i\vartheta}$ is taken into account. The parameter ϑ describes the phase shift of the stimulation signal before acting on each oscillator which in general is non-zero for neural ensembles [RP04b]. Moreover it is an important and well-controllable parameter for feedback in technical applications like Laser systems [HFE01, HFE03]. An appropriate phase shift has proved to even increase the control performance in other time-delayed feedback schemes [BASJ02, JPA⁺03]. For $\vartheta = 0$ the desynchronizing effect of the nonlinear delayed feedback protocol is extensively studied [PHT05b]. In this work analytical solutions analogous to the approach in the original work are derived but for

an arbitrary phase shift.

In order to understand analytically the influence of the stimulation on the ensemble, the dynamics of the normalized mean field of the strongly synchronized and stimulated ensemble $W(t) = N^{-1} \sum_{j=1}^N |Z_j(t)|^{-1} Z_j(t) =: R(t)e^{i\theta(t)}$ is modeled by a single limit-cycle oscillator [PHT05b] with

$$\dot{W}(t) = \frac{C}{2}(1 - |W(t)|^2)W(t) + i\Omega_0 W(t) + \frac{K}{2}e^{i\vartheta} W^2(t)W^*(t - \tau) \quad (5.6)$$

For $K = 0$ and $C > 0$ the oscillator rotates on a stable limit cycle with radius 1 and frequency Ω_0 . Looking for solutions of the differential equation 5.6 the ansatz $W(t) = Re^{i\Omega t}$ with constant amplitude R leads to

$$Ri\Omega e^{i\Omega t} = \frac{C}{2}(1 - R^2)Re^{i\Omega t} + i\Omega_0 Re^{i\Omega t} + \frac{K}{2}R^3 e^{i\vartheta} e^{2i\Omega t} e^{-i\Omega(t-\tau)} \quad (5.7)$$

Multiplication with $R^{-1}e^{-i\Omega t}$ gives

$$i\Omega = \frac{C}{2}(1 - R^2) + i\Omega_0 + \frac{K}{2}R^2 e^{i\vartheta} e^{i\Omega t} e^{-i\Omega(t-\tau)} \quad (5.8)$$

Separating the preceding equation into real and imaginary part gives the following two equations

$$\Omega - \Omega_0 = R^2 \frac{K}{2} \sin(\Omega\tau + \vartheta) \quad (5.9)$$

$$\wedge \frac{C}{2}(1 - R^2) = -R^2 \frac{K}{2} \cos(\Omega\tau + \vartheta) \quad (5.10)$$

which can be written as

$$\Omega = \Omega_0 + \frac{KC \sin(\Omega\tau + \vartheta)}{2C - 2K \cos(\Omega\tau + \vartheta)} \quad (5.11)$$

$$\wedge R^2 = \frac{C}{C - K \cos(\Omega\tau + \vartheta)} \quad (5.12)$$

With respect to a maximum suppression of R by stimulating the ensemble, optimal solutions of equation 5.11 are given by

$$\Omega = \Omega_0, \quad R = \sqrt{\frac{C}{C - K}} \quad (5.13)$$

which is realized by $\Omega_0\tau + \vartheta = 2n\pi$ with $K \leq 0$ and

$$\Omega = \Omega_0, \quad R = \sqrt{\frac{C}{C + K}} \quad (5.14)$$

for $\Omega_0\tau + \vartheta = (2n + 1)\pi$ with $K \geq 0$, respectively. For n it holds $n \in \mathbb{N}_0$ (\mathbb{N}_0 : natural numbers including zero) in both cases. For $\vartheta = 0$ the solutions are known to be stable which can be shown using linear stability theory [PHT05b].

In figure 5.1 function $R(K)$ according to equation 5.14 is plotted. Also shown is the order parameter of the ensemble

$$\langle R(t) \rangle_{T_S} = \left\langle \left| \frac{1}{N} \sum_{j=1}^N |Z_j(t)|^{-1} Z_j(t) \right| \right\rangle_{T_S} \quad (5.15)$$

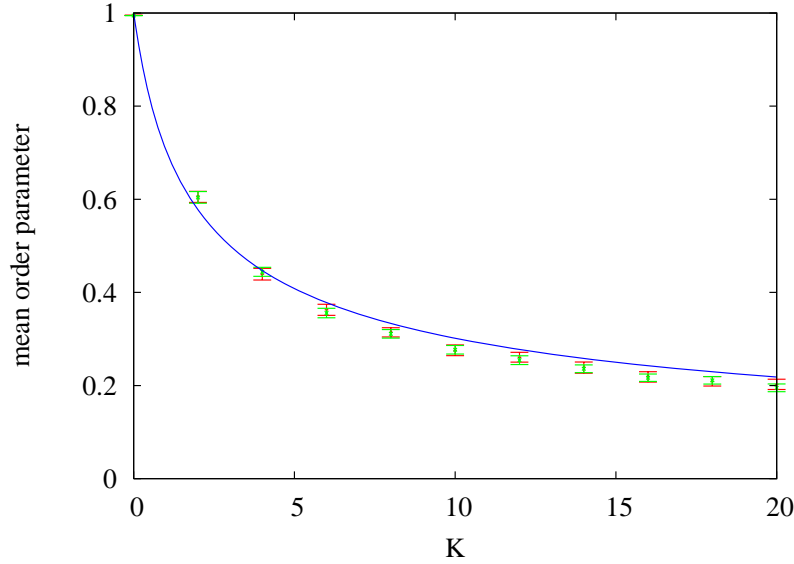


Figure 5.1: Order parameter in dependence of the feedback strength K . Blue: R according to equation 5.14 for the optimal solutions. Red: order parameter $\langle R(t) \rangle_{T_S}$ averaged over stimulation time ($T_S = 2000$) from numerical simulations with an ensemble of 200 limit cycle oscillators ($a_i \equiv 1.0$), $\tau = 2.5$, and $\vartheta = 0.0$. The error bars indicate the standard deviation of the order parameters averaged. Green: mean order parameter $\langle R(t) \rangle_{T_S}$ from numerical solutions with the same ensemble but with different values of τ and ϑ for each tested K . In order to investigate the predicted optimal solutions, the dependence has been $\vartheta = \frac{K}{20}2\pi$ together with $\tau = \frac{3\pi}{\Omega_0} - \frac{\vartheta}{\Omega_0}$ for the green values. The global coupling strength C has been set to 1.0 and the mean period to $T = 5.0$ ($\Omega_0 = \frac{2\pi}{T} \approx 1.3$) in all three cases. For the ensembles the frequency deviation has been $\sigma_\omega = 0.1$.

averaged over stimulation time in dependence of the feedback strength K . The stimulation time was $T_S = 2000$ after a transient epoch of 200 in all calculations with nonlinear delayed feedback in this chapter. Simulations have been performed with an ensemble of $N = 200$ limit cycle oscillators. The coupling strength has been set to $C = 1$ whereas the mean natural period of the oscillators is equal to 5. The standard deviation of the distribution of natural frequencies has been set to $\sigma_\omega = 0.1$ with individual radii of all oscillators $a_i = 1$. The green crosses in figure 5.1 refer to numerical simulations with $\vartheta = 0.0$ and $\tau = 2.5$ for all tested values of K . The dependence of $\langle R(t) \rangle_{T_S}$ on K for these simulations are in good agreement with the predicted function (blue curve). For phase oscillators the agreement is even better as shown in figure 3 in [PHT05b].

The red crosses in figure 5.1 present results for varying values of τ and ϑ . For each tested value of K these parameters are given by $\vartheta = \frac{K}{20}2\pi$ and $\tau = \frac{3\pi}{\Omega_0} - \frac{\vartheta}{\Omega_0}$, respectively. Thus ϑ has been varied from 0 to 2π in the tested regime of K and τ has been adjusted for each value of ϑ in a way that the condition $\Omega_0\tau + \vartheta = 3\pi$ holds with respect to the desired optimal solution. In figure 5.1 corresponding red and green crosses for the same value of K do not differ. Hence the analytical prediction is valid that an additional phase shift of the feedback signal can be corrected by an appropriate change of the time delay (and vice versa), in order to assure an optimal solution.

Because in the next chapter the linear and nonlinear delayed feedback protocols are tested in an experiment, some results in [THP06] concerning their performance are shortly summarized in this paragraph. Figure 5.2 taken from [THP06] shows the degree of synchronization for different

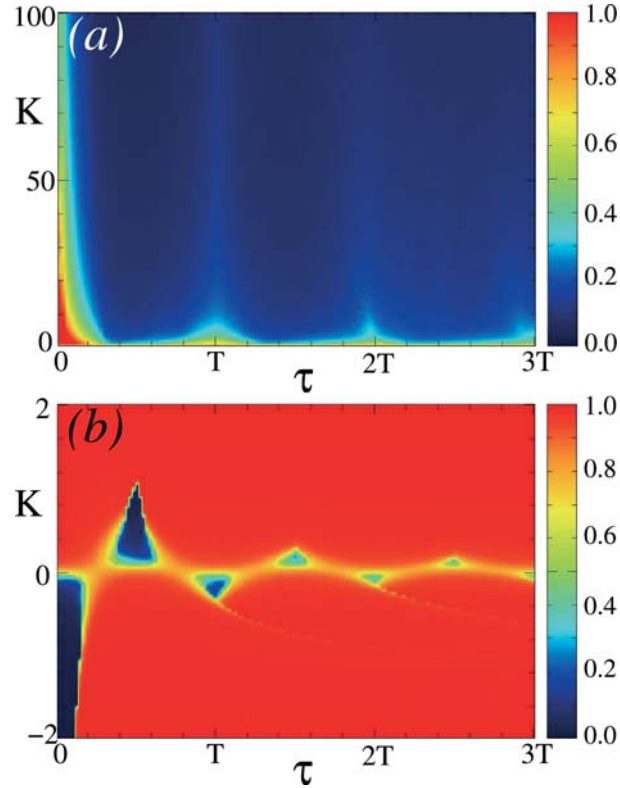


Figure 5.2: Color coded order parameter in dependence of the stimulation strength K and the time delay τ for different feedback methods (from: [THP06]). Top: nonlinear delayed feedback by Popovych et al. [PHT05b], bottom: linear delayed feedback by Rosenblum et al. [RP04a]. The values of the averaged order parameter result from a simulation of $N = 100$ globally coupled phase oscillators ($C=0.25$). The mean natural period of the ensemble has been $T = 5$ (mean natural frequency $\Omega_0 = \frac{2\pi}{T} \approx 1.3$), the individual natural frequencies have been Gaussian distributed with deviation $\sigma = 0.1$ [THP06].

values of K and τ including also non-optimal solutions. For this plot no phase shift has been taken into account ($\vartheta = 0$). Please note that desynchronization can always be achieved for the nonlinear delayed feedback protocol by an adequate choice of K , even if $\Omega_0\tau = (2n+1)\pi$ does not hold. This characteristic favors this method drastically compared to the linear delayed feedback (equation 5.1) whose results are also shown in figure 5.2. The linear delayed feedback exhibits only *islands* of desynchronization around $\tau = \frac{n}{2}T$ with bounded regimes for the associated values of K .

5.2 Distributed source models in a nonlinear delayed feedback scenario

Since one specific aim of this work is to realize an MEG feedback for the manipulation of brain rhythms, it is of interest to test the performance of inverse routines with respect to the desynchronization of neural populations by feedback. For this, the influence of a *perturbing current source*

on the desynchronization of a neural ensemble will be quantified. The perturbing current source in a specific voxel, whose position will be varied across the entire source space, is modeled by the mean field of a strongly synchronized ensemble 1 of N_1 limit cycle oscillators. Ensemble 2 situated in another fixed voxel is stimulated by nonlinear delayed feedback, in order to desynchronize its N_2 strongly coupled oscillators. For the modeling of the mean field $\bar{Z}_1(t)$ of the perturbing ensemble and of the mean field $\bar{Z}_2(t)$ of the population to be desynchronized, consider two ensembles of globally coupled limited oscillators obeying

$$\dot{Z}_{j,1}(t) = (a_{j,1} + i\omega_{j,1} - |Z_{j,1}(t)|^2)Z_{j,1}(t) + C_1\bar{Z}_1(t) \quad (5.16)$$

$$\dot{Z}_{j,2}(t) = (a_{j,2} + i\omega_{j,2} - |Z_{j,2}(t)|^2)Z_{j,2}(t) + C_2\bar{Z}_2(t) + S(t) \quad (5.17)$$

There is no coupling between both ensembles. The mean fields of both ensembles are defined analogous to equation 5.4, i.e.

$$\bar{Z}_1(t) := \frac{1}{N_1} \sum_{j=1}^{N_1} Z_{j,1}(t) \quad (5.18)$$

and

$$\bar{Z}_2(t) := \frac{1}{N_2} \sum_{j=1}^{N_2} Z_{j,2}(t) \quad (5.19)$$

The following scenario is investigated. The current density inside a specific voxel of interest with index i is reconstructed, in order to stimulate population 2 situated there. It is assumed that two components of the three-dimensional current density are 0 for all times. The third component j_i^r is proportional to mean field 2 with a proportionality factor set to 1. Let us further assume that only one more voxel with index k inside the source space is active due to a perturbing source. One component (j_k^s) of its associated current density is equal to $\bar{Z}_1(t)$. Ensemble 2 will be stimulated by the reconstructed current density belonging to voxel i and direction r . The perturbing source disturbs the desired desynchronization of ensemble 2, because the feedback signal exhibits mixed information of both ensembles. Because inverse routines act as spatial filters, feedback signals that are defined by the reconstructed current density are expected to deliver a significantly better stimulation performance than using just the detected magnetic fluxes for feedback. The results of simulations for this will be shown in this section. The distributed source models introduced in chapter 4 will be further contrasted in these tests regarding this highly relevant new aspect.

The reconstructed component of the current density in the voxel of interest \hat{j}_i^r is given by

$$\hat{j}_i^r = R_{ii}^{rr} j_i^r + R_{ik}^{rs} j_k^s \quad (5.20)$$

As in the preceding chapters R denotes the resolution matrix which maps the original current density distribution \vec{j} on the reconstructed current density distribution \hat{j} depending on the applied linear inverse routine. The plan is to desynchronize the source of interest j_i^r by nonlinear delayed feedback of the reconstructed current density \hat{j}_i^r . The difference to the stimulation signal of the nonlinear delayed feedback protocol discussed so far in this chapter is given by the mixing of mean fields belonging to two different ensembles. For the general case, this mixing, whose actual degree depends on the components of the resolution matrix R_{ii}^{rr} and R_{ik}^{rs} , can be described by

$$\bar{Z}(t) = (1 - \epsilon)\bar{Z}_2(t) + \epsilon\bar{Z}_1(t) \quad (5.21)$$

The mixing of these fields results in mean field $\bar{Z}(t)$ which is used to build the stimulation signal for nonlinear delayed feedback (equation 5.2). The degree of the superposition of the mean fields is tuned by the *mixing parameter* ϵ with $0 < \epsilon \leq 1$. For $\epsilon \approx 1$ the stimulation signal is mostly determined by the mean field of the perturbing source. For small values of ϵ the stimulation signal is mainly built by the mean field of the source to be desynchronized resulting in a suppression of its rhythm as described in the preceding chapter.

For given values of R_{ii}^{rr} and R_{ik}^{rs} the parameter ϵ is determined by their ratio

$$\frac{1 - \epsilon}{\epsilon} = \frac{R_{ii}^{rr}}{R_{ij}^{rs}} \quad (5.22)$$

which gives the following condition for ϵ

$$\epsilon = \frac{R_{ij}^{rs}}{R_{ij}^{rs} + R_{ii}^{rr}} \quad (5.23)$$

This connects the superposition of mean fields according to equation 5.21, which is used for building the stimulation signal, with equation 5.20, in order to quantify how the actual mixing due to the MEG reconstruction process affects the feedback performance.

If R_{ii}^{rr} and R_{ij}^{rs} have opposite signs, ϵ in equation 5.22 is not within the predefined range $0 < \epsilon \leq 1$. For these cases, the mixing is modeled by

$$\bar{Z}(t) = (1 - \epsilon)\bar{Z}_2(t) - \epsilon\bar{Z}_1(t) \quad (5.24)$$

For given R_{ii}^{rr} and R_{ik}^{rs} , ϵ is then obtained by $(1 - \epsilon)/(-\epsilon) = R_{ii}^{rr}/R_{ij}^{rs}$ leading to

$$\epsilon = \frac{R_{ij}^{rs}}{R_{ij}^{rs} - R_{ii}^{rr}} \quad (5.25)$$

again with $0 < \epsilon \leq 1$. Next feedback via a detector signal directly is considered, i.e without applying a current density reconstruction. For the output of detector l holds, if only the two current density components j_i^r and j_k^s are unequal to zero as before

$$m_l = \Phi_{li}^r j_i^r + \Phi_{lk}^s j_k^s \quad (5.26)$$

In this equation Φ_{li}^r is the entry in the lead field matrix which denotes the sensitivity of the l -th detector with respect to the r -th component of the current density in voxel i (analogous: Φ_{lk}^s). Thus, concerning the degree of mixing in sensor feedback Φ_{li}^r takes the role of R_{ii}^{rr} in voxel feedback and Φ_{lk}^s that of R_{ij}^{rs} . Hence the corresponding value of ϵ in equation 5.21 for sensor feedback is given by $\epsilon = \Phi_{lk}^s / (\Phi_{lk}^s + \Phi_{li}^r)$, if Φ_{li}^r and Φ_{lk}^s have the same signs. Otherwise, for ϵ it holds $\epsilon = \Phi_{lk}^s / (\Phi_{lk}^s - \Phi_{li}^r)$ ($0 < \epsilon \leq 1$).

$N_1 = N_2 = 200$ oscillators have been taken into account for the simulations in each case. All individual radii $a_{j,1}$ and $a_{j,2}$ are set to 1. The mean natural frequencies of both ensembles are Gaussian distributed with each mean frequency equal to $\frac{2\pi}{5} \approx 1.3$ and with a standard deviation σ equal to 10% of the mean. The global coupling strengths in the populations have been set to

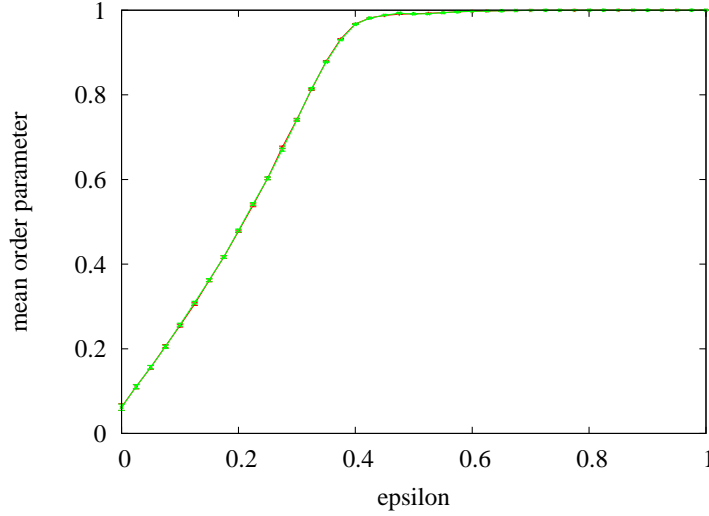


Figure 5.3: Mean order parameter $\langle R_2(t) \rangle_{T_s}$ together with its standard deviation in dependence on the mixing parameter ϵ for the nonlinear delayed feedback protocol with $S(t) = K \bar{Z}^2(t) \bar{Z}^*(t - \tau)$. Green curve: mean field used for feedback given by $\bar{Z}(t) = (1 - \epsilon) \bar{Z}_2(t) + \epsilon \bar{Z}_1(t)$. Red curve (mostly covered by the green one): mean field used for feedback obeys $\bar{Z}(t) = (1 - \epsilon) \bar{Z}_2(t) - \epsilon \bar{Z}_1(t)$

$C_1 = C_2 = 1$ which delivers strongly synchronized ensembles in the absence of stimulation. In figure 5.3 the order parameter of the ensemble of interest

$$\langle R_2(t) \rangle_{T_s} = \left\langle \left| \frac{1}{N_2} \sum_{j=1}^{N_2} |Z_{j,2}^{-1}(t)| Z_{j,2}(t) \right| \right\rangle_{T_s} \quad (5.27)$$

averaged over stimulation time is plotted in dependence of the mixing parameter ϵ . The applied stimulation strength was $K = 200$, the time delay for the stimulation signal in equation 5.2 was set to $\tau = 2.5$. The green curve belongs to results from simulations with a mean field used for the stimulation signal, which obeys equation 5.21. The strong desynchronization by stimulating via mean field $\bar{Z}_2(t)$, i.e. $\epsilon = 0$, is visible. For increasing ϵ the mixing of both mean fields leads to a driving of ensemble 2, as ensemble 1 is strongly synchronized and not affected by the stimulation. In figure 5.3 a red curve is hidden by the green curve which belongs to simulations with a mean field used for the stimulation signal obeying equation 5.24. Hence both forms of the stimulation have the same effect on the degree of synchronization of the second ensemble.

The mappings of ϵ onto the resulting mean order parameter $\langle R_2(t) \rangle_{T_s}$ shown in figure 5.3 in combination with equations 5.23 and 5.25 are used in order to evaluate the degree of mixing for different resolution matrices. For this, intermediate values of $\langle R_2(t) \rangle(\epsilon)$ have been interpolated linearly. The investigated inverse routines are the spatial filter systems SOFIA, WROP, and pWROP again for different settings of their constraint parameter together with GaussMN as in chapter 4. The applied head-sensor-configuration and the setup of the source space for the calculation of each resolution matrix can be gathered from the preceding chapters. The same region of interest as in chapter 4, i.e. a sphere with a radius of 1.5 cm around visual cortex area V5, has been chosen. Voxel i and the component of the current density of interest r is fixed in all results

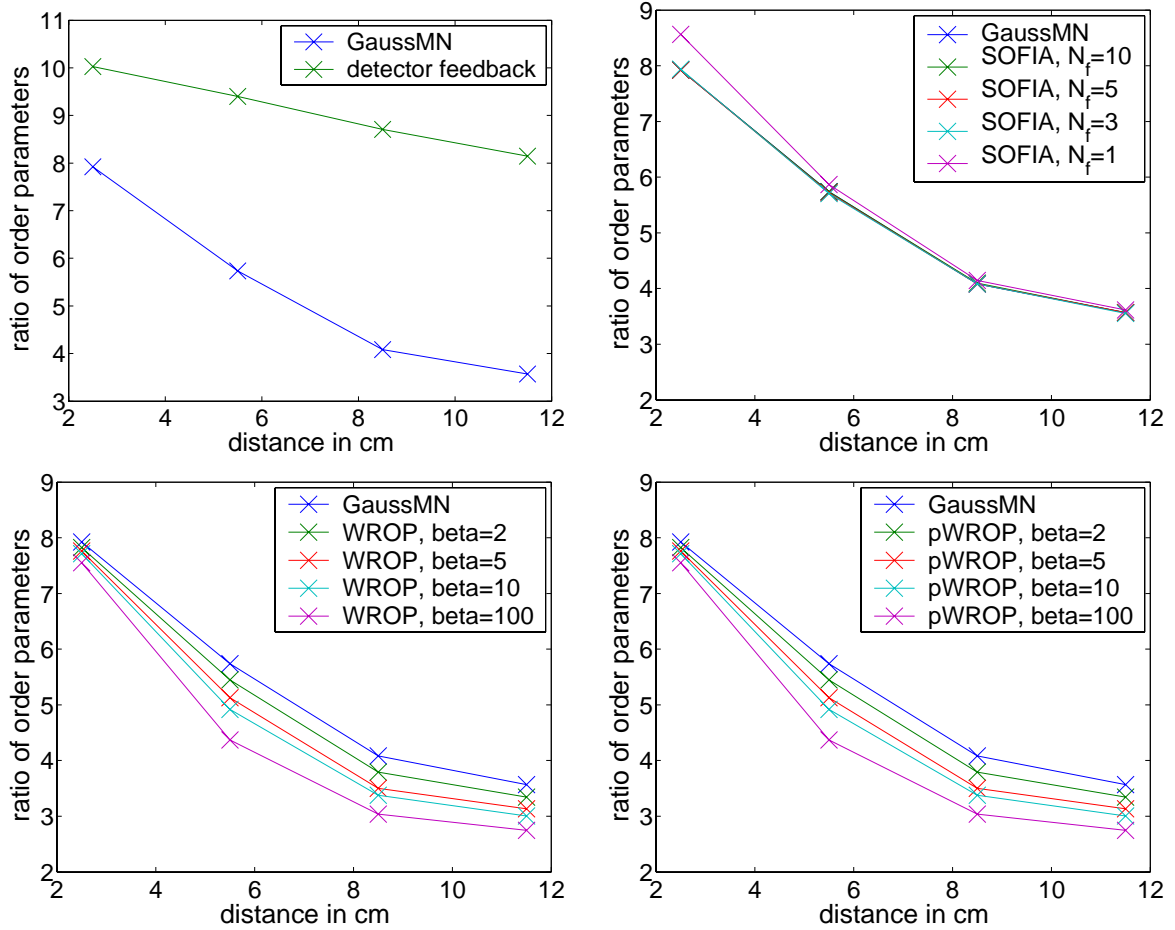


Figure 5.4: Averaged order parameters of the stimulated ensemble 2 for different areas of the perturbing ensemble 1 and different inverse methods used for feedback. The plotted order parameters $\langle R_2(t) \rangle(\epsilon)$ are averaged for distances between ensemble 1 and 2 in the source space being smaller or equal than 2.5 cm, 5.5 cm, 8.8 cm, and 11.5 cm, respectively. They are furthermore divided by the order parameter without any perturbing source ($\langle R_2(t) \rangle(0) = 0.062$). Top left: results for the GaussMN inverse method compared to sensor feedback, top right: GaussMN and SOFIA for different number of used virtual sensors, bottom left: GaussMN and WROP for different settings of β , bottom right: GaussMN and pWROP.

discussed in the following, which belong to a grid point in the center of the region of interest for a current dipole pointing the z-direction. This position is indicated by a green cross in figure 4.4. For each tested inverse routine this choice of i and r gives the resolution matrix entry R_{ii}^{rr} used in equations 5.23 and 5.25.

The position (voxel k) and active current density component (s -th component) of the perturbing source, which is represented by R_{ik}^{rs} in these equations, is varied across the source space grid and all three spatial directions. Positions for the perturbing source inside the ROI sphere have been omitted, because the investigated spatial filter systems SOFIA, pWROP, and WROP are used to reduce the mixing between the predefined region of interest and the remaining source space but not inside both regions. In other words, for the chosen resolution kernel identified by i and r all entries R_{ik}^{rs} have been taken into account, except for voxels k belonging to the region of interest.

The specific value of the mixing parameter ϵ for each pair of R_{ii}^{rr} and R_{ik}^{rs} according to equation 5.23 and 5.25, gives the degree of synchronization $\langle R_2(t) \rangle (\epsilon)$ shown in figure 5.3.

In order to summarize results, for each investigated resolution matrix R these order parameters have been averaged across subareas in the source space. For this, values for perturbing sources exhibiting a distance smaller or equal than 2.5 cm, 5.5 cm, 8.5 cm, and 11.5 cm, respectively, to the source of interest have been averaged. For the case of 11.5 cm all tested positions of ensemble 2 are taken into account. Moreover, the averaged order parameters presented in figure 5.3 are divided by the degree of synchronization in ensemble 2, if the stimulation signal is constructed purely by its own mean field ($\langle R_2(t) \rangle (0)$). For the detector feedback (see equation 5.26) the sensor signal was used that showed the largest sensitivity for ensemble 2, i.e. the largest value of Φ_{li}^r among all l whereby $1 \leq l \leq 90$.

The drastic influence of the perturbing source on the feedback gain can be gathered from figure 5.4. For distances between both ensembles less or equal than 2.5 cm the tested methods produce an increase of the average order parameter of ensemble 2 by a factor of 7 and more compared to the undisturbed case ($\epsilon = 0$). Note that in all cases the detector feedback is not drastically, i.e. by orders of magnitude, less effective than feedback with the aid of the reconstruction techniques. As expected the averaged degree of synchronization decreases monotonically with an increase of the considered distances and the detector feedback exhibits the worst performance in all subareas. The graphs derived from applying the inverse routines show a more negative gradient than the curve of the detector feedback due to their behavior as a spatial filter. SOFIA shows no significant difference compared to GaussMN for the tested resolution kernel except for the case of $N_f = 1$ where its performance is even worse for distances smaller or equal than 8.5 cm. The graphs for WROP and pWROP are practically identical. They are distinctly superior to GaussMN for distances around 4 cm depending on the setting of the constraint parameter β .

5.3 Mixed nonlinear delayed feedback

In the rest of this chapter a new effect regarding the nonlinear delayed feedback technique is presented. In the last section two ensembles of limit cycle oscillators have been considered with a strong coupling inside the populations but without a coupling between the ensembles. A mixture of both mean fields in applying the nonlinear delayed feedback had been investigated, because this superposition of signals is an unavoidable and significant characteristic in MEG. Using this modified nonlinear delayed feedback protocol hinders the desynchronization of the stimulated ensemble. In the following it will be shown that the mixing of mean fields is able to improve the feedback gain drastically under certain conditions, if there is a coupling between both ensembles. First, the effects of nonlinear delayed feedback in two ensembles with a back and forward coupling, as introduced in [PHT06b], are shortly summarized. Starting from this point the enhanced desynchronization and decoupling of oscillators by using the mixed mean fields for the feedback will be demonstrated. The effect is explained qualitatively and a modeling approach on the way to an analytical understanding is given.

5.3.1 Desynchronization and decoupling of interacting populations

Consider the following situation of two ensembles of coupled limit cycle oscillators:

$$\begin{aligned}\dot{Z}_{j,1}(t) &= (a_{j,1} + i\omega_{j,1} - |Z_{j,1}(t)|^2)Z_{j,1}(t) \\ &\quad + C_1\bar{Z}_1(t) + C_{21}\bar{Z}_2(t)\end{aligned}\quad (5.28)$$

$$\begin{aligned}\dot{Z}_{j,2}(t) &= (a_{j,2} + i\omega_{j,2} - |Z_{j,2}(t)|^2)Z_{j,2}(t) \\ &\quad + C_2\bar{Z}_2(t) + C_{12}\bar{Z}_1(t) + S(t)\end{aligned}\quad (5.29)$$

The only difference to the scenario described in equations 5.16 and 5.17 is that both populations are now interacting via a back and forward coupling. Again only the second ensemble is stimulated directly. The situation is sketched in figure 5.5. Ensemble 2 is stimulated by

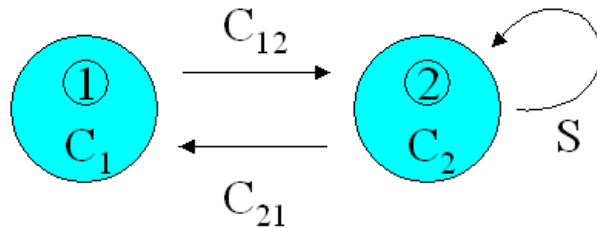


Figure 5.5: Sketch of the coupled ensembles with delayed feedback stimulation in ensemble 2.

$$S(t) = K\bar{Z}^2(t)\bar{Z}^*(t - \tau)\quad (5.30)$$

First the unmixed feedback with

$$\bar{Z}(t) = \bar{Z}_2(t)\quad (5.31)$$

is considered. The desynchronizing and decoupling effect due to this form of nonlinear delay feedback has been studied extensively [PHT05b, PHT06b]. It will be illustrated in this section, since it is the starting point of the mixed nonlinear delayed feedback presented in section 5.3.2.

Figure 5.6 shows the time courses of the mean fields of both ensembles before and during stimulation. The values of the global coupling strengths inside each network are $C_1 = 1$ and $C_2 = 0.01$ in this example. The individual radii $a_{j,k}$ are 1 for all j and k . Numerical simulations have been performed with 200 limit cycle oscillators in each ensemble ($N_1 = N_2 = 200$). The natural frequencies of the oscillators are Gaussian distributed in both networks around mean values $\omega_1 = \frac{2\pi}{6} = 1.047$ for population 1 and $\omega_2 = \frac{2\pi}{4} = 1.571$ for population 2, whereby both frequency distributions exhibited a standard deviation of $\sigma_\omega = 0.1$. For $C_{21} = C_{12} = K = 0$ a strongly synchronized ensemble 1 is induced with an averaged order parameter

$$\langle R_1(t) \rangle_{T_S} = \left\langle \left| \frac{1}{N_1} \sum_{j=1}^{N_1} \frac{Z_{j,1}(t)}{|Z_{j,1}(t)|} \right| \right\rangle_{T_S}\quad (5.32)$$

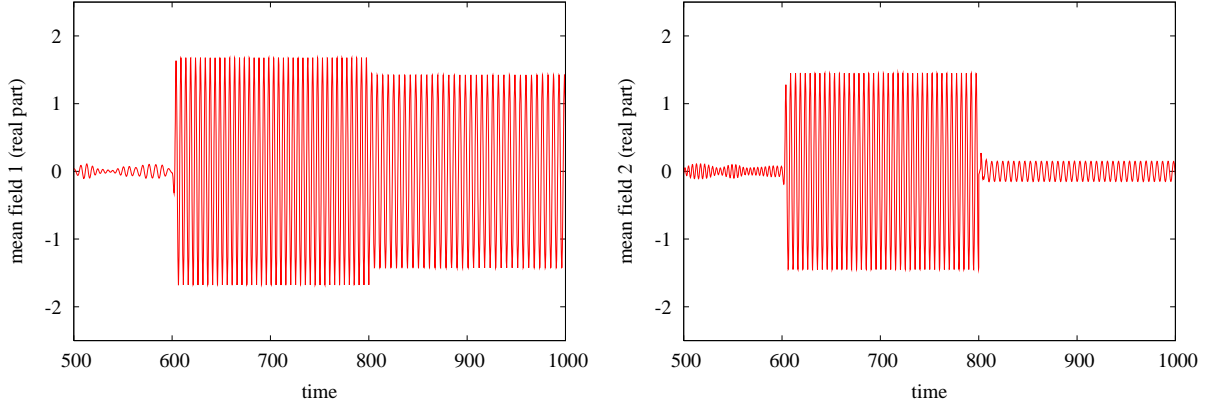


Figure 5.6: Mean fields (real part) of ensemble 1 (left) and ensemble 2 (right panel) under the influence of stimulation with $S(t) = K\bar{Z}_2^2(t)\bar{Z}_2^*(t - \tau)$: all coupling terms are switched on at $t = 600$, at $t = 800$ the stimulation becomes active ($K = 400$).

equal to 0.995. Ensemble 2 however is in a desynchronized state with an averaged order parameter

$$\langle R_2(t) \rangle_{T_S} = \left\langle \left| \frac{1}{N_2} \sum_{j=1}^{N_2} \frac{Z_{j,2}(t)}{|Z_{j,2}(t)|} \right| \right\rangle_{T_S} \quad (5.33)$$

equal to 0.068 which is equal to zero for $N_2 \rightarrow \infty$, since C_2 is smaller than the critical coupling strength

$$C_{crit} = \sqrt{\frac{8}{\pi}} \sigma_\omega = 0.16 \quad (5.34)$$

characterizing the onset of synchronization [PR99, Kur84].

If a strong interaction between both ensembles is initiated ($C_{21} = C_{12} = 1$ in the following), but the stimulation term is still zero, ensemble 1 induces synchronization in ensemble 2 in a driving sense. Then the order parameters are $\langle R_1(t) \rangle_{T_S} = 0.998$ and $\langle R_2(t) \rangle_{T_S} = 0.996$, respectively. A stimulation given by equations 5.30 and 5.31 with $K = 400$ and $\tau = 2.0$ desynchronizes the driven population, which is observed by $\langle R_2(t) \rangle_{T_S} = 0.141$ in this setup. The driving population is only slightly affected (figure 5.6) with $\langle R_1(t) \rangle_{T_S} = 0.996$.

Another drastic consequence of the applied stimulation is given by the fact that the individual natural frequencies inside population 2 are restored during stimulation [PHT05b, PHT06b]. This can be interpreted as an effective decoupling of the oscillators in the driven ensemble. In figure 5.7 two exemplary trajectories of oscillators in population 1 and population 2, respectively, are shown with the same parameter settings as described above. The amplitude of both oscillators are increased by the coupling terms compared to the uncoupled state, but only the amplitude of the oscillator in the driven ensemble is nearly restored when the stimulation is switched on. The decoupling effect can be quantified by the average difference between the natural frequency of

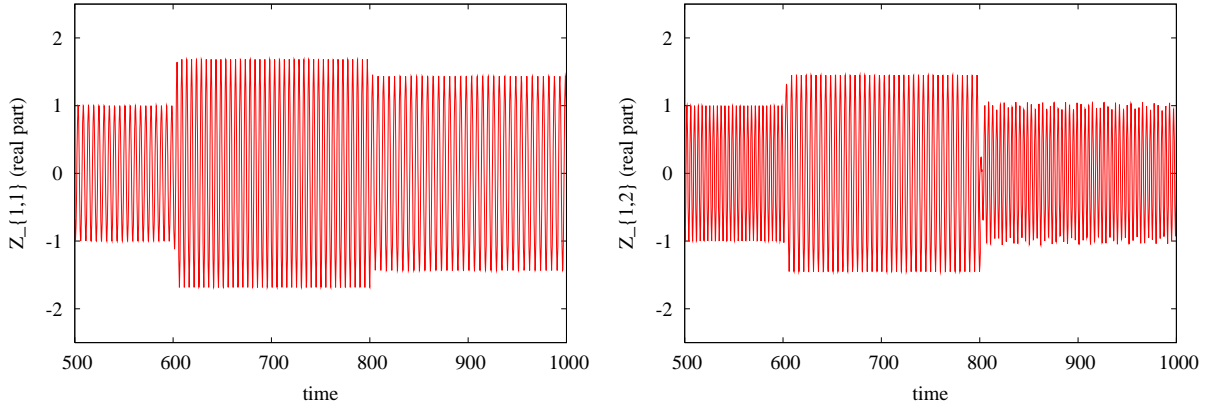


Figure 5.7: Exemplary trajectories (real part) of an oscillator in ensemble 1 (left panel) and in ensemble 2 (right panel) under the influence of stimulation with $S(t) = K\bar{Z}_2^2(t)\bar{Z}_2^*(t - \tau)$: all coupling terms are switched on at $t = 600$, at $t = 800$ the stimulation becomes active ($K = 400$).

each oscillator $\omega_{j,k}$ and its mean frequency $\langle \omega_{j,k} \rangle_{S_{stim}}$ during the stimulation epoch

$$\Delta\omega_k^{S_{stim}} = \sqrt{\frac{1}{N_k} \sum_{j=1}^{N_k} (\omega_{j,k} - \langle \omega_{j,k} \rangle_{S_{stim}})^2} \quad (5.35)$$

with $k = 1, 2$ indicating the considered ensemble. As a reference, analogous measures are defined for the stimulation-free case

$$\Delta\omega_k^{Coup} = \sqrt{\frac{1}{N_k} \sum_{j=1}^{N_k} (\omega_{j,k} - \langle \omega_{j,k} \rangle_{Coup})^2} \quad (5.36)$$

describing the average difference between the natural frequency of each oscillator and its mean frequency $\langle \omega_{j,k} \rangle_{Coup}$ during coupling but before stimulating. In the chosen configuration the values are $\Delta\omega_2^{S_{stim}} = 0.017$ and $\Delta\omega_2^{Coup} = 0.321$, respectively, for the driven ensemble. This shows the relatively strong rebuilding of the natural frequencies due to the nonlinear feedback in ensemble 2. In contrast the propagated decoupling in the driving ensemble is much smaller. Here $\Delta\omega_1^{S_{stim}}$ is equal to 0.125 and $\Delta\omega_1^{Coup} = 0.240$.

5.3.2 Mixing the mean fields for the stimulation of interacting populations

The stimulation signal in equation 5.30 is now defined by

$$\bar{Z}(t) = (1 - \epsilon)\bar{Z}_2(t) + \epsilon\bar{Z}_1(t) \quad (5.37)$$

Again the mixing parameter ϵ ($0 \leq \epsilon \leq 1$) tunes the degree of mixing of mean fields for the stimulation. For $\epsilon = 0$ the stimulation signal is only determined by the mean field of ensemble 2 as discussed in the previous section, for $\epsilon = 1$ only the mean field of the first population is taken

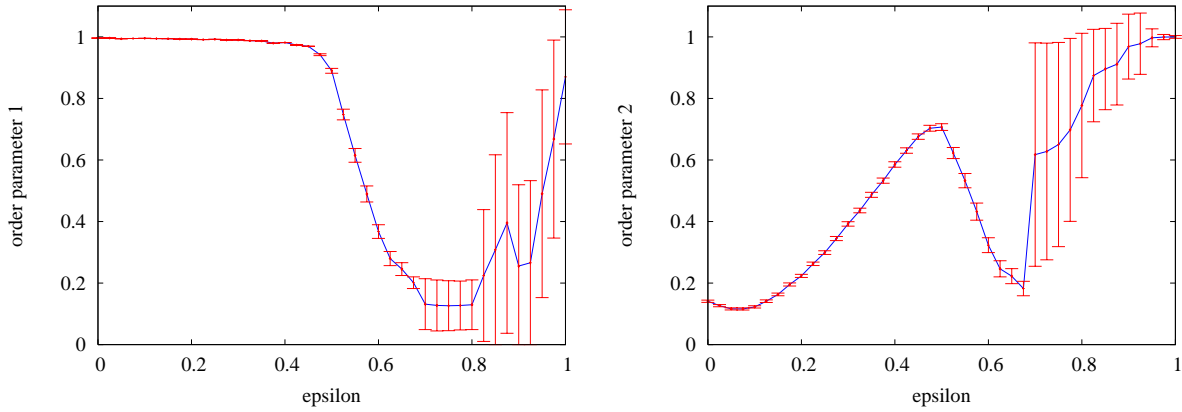


Figure 5.8: Order parameters with standard deviations for population 1 ($\langle R_1(t) \rangle_{T_S}$, left image) and population 2 ($\langle R_2(t) \rangle_{T_S}$, right) versus mixing parameter ϵ .

into account for the stimulation signal. The simulations have been performed with a fixed setting of ϵ , which has been varied with a step size of 0.025 between the simulations. In figure 5.8 the order parameters averaged over stimulation time for both ensembles are plotted in dependence of ϵ . For the driven population (ensemble 2) a slight increase of ϵ gives a further decrease of $\langle R_2(t) \rangle_{T_S}$. For the parameter settings in the previous section the absolute minimum of $\langle R_2(t) \rangle_{T_S}$ is found near $\epsilon = 0.075$. A further increase of ϵ destroys the desynchronization in the driven ensemble, until around $\epsilon = 0.5$ the order parameter decreases again. A second local minimum of $\langle R_2(t) \rangle_{T_S}$ is found at about $\epsilon = 0.675$. Increasing ϵ further leads to a sharp rise of the order parameter with a very irregular corresponding trajectory for mean field 2 indicated by the large standard deviations. The impact of ϵ on $\langle R_1(t) \rangle_{T_S}$ is even more drastic. Starting from a very strong synchronization in ensemble 1 ($\langle R_1(t) \rangle_{T_S} \approx 1$) for $\epsilon < 0.4$, the driving population strongly desynchronizes for $0.4 < \epsilon < 0.6$. For larger values of ϵ , $\langle R_1(t) \rangle_{T_S}$ increases again. Please note that for $\epsilon > 0.675$, the time-dependent order parameters of both ensembles undergo strong fluctuations. The graphs for $\Delta\omega_1^{stim}(\epsilon)$ and $\Delta\omega_2^{stim}(\epsilon)$ (figure 5.9) show qualitatively the same results leading to the assumption that both measures may display the same mechanism.

For the critical value of $\epsilon = 0.675$, where both order parameters $\langle R_1(t) \rangle_{T_S}$ and $\langle R_2(t) \rangle_{T_S}$ reach their minimum but where a further increase of ϵ would destroy the desynchronization, the trajectories of the mean fields are shown in figure 5.10. After a short transient epoch, the stimulation strongly suppresses the amplitudes of both mean fields. This is a distinctly different influence of the feedback signal on the networks as compared to the case $\epsilon = 0$ (figure 5.6) where the driver is barely affected by the stimulation. In figure 5.11 two exemplary trajectories of oscillators are shown for $\epsilon = 0.675$. After switching on the stimulation there is a short transient epoch with an increase of the amplitudes in ensemble 2, until the steady state is reached (see also figure 5.10). The amplitude of oscillators in both ensembles is nearly 1 which is the radius of their undisturbed limit cycle ($a_{j,k} = 1$ for all j and $k = 1, 2$). This illustrates the enhanced decoupling effect by mixed nonlinear delayed feedback in both ensembles.

The individual oscillators behave nearly like uncoupled, if the order parameter of their ensemble reaches a minimum. For ensemble 1 this means that the sum of the internal coupling and the

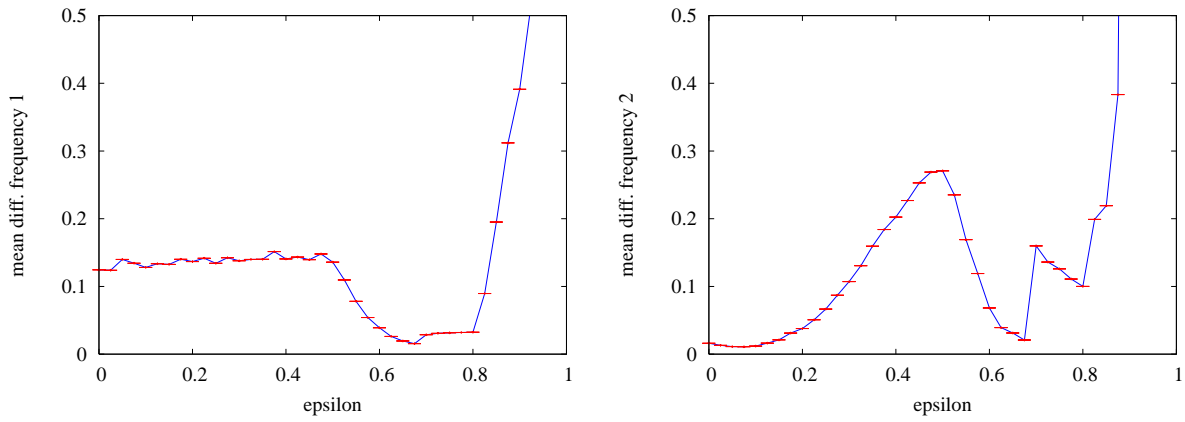


Figure 5.9: $\Delta\omega_1^{stim}$ (left) and $\Delta\omega_2^{stim}$ (right) versus mixing parameter ϵ .

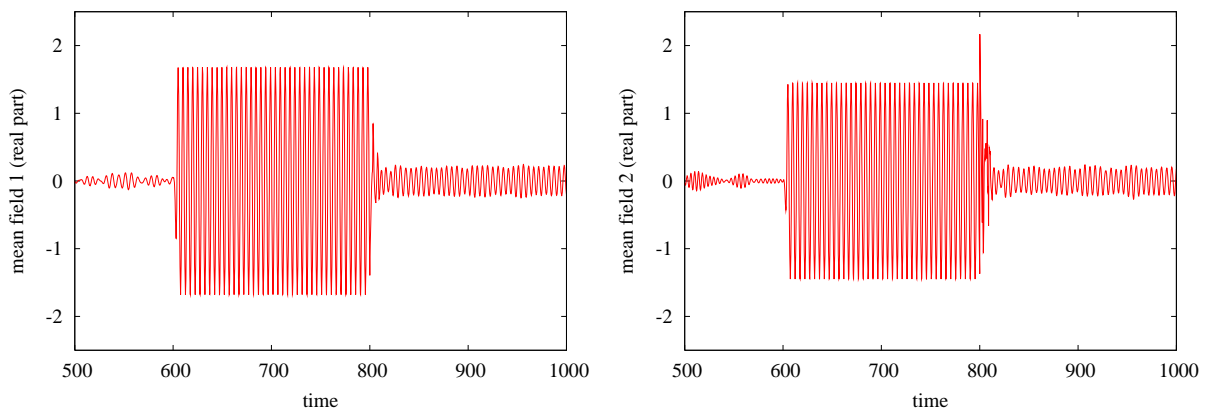


Figure 5.10: Mean fields (real part) of ensemble 1 (left) and ensemble 2 (right panel) stimulated with mixed nonlinear delayed feedback ($\epsilon = 0.675$): all coupling terms are switched on at $t = 600$, at $t = 800$ the stimulation becomes active ($K = 400$).

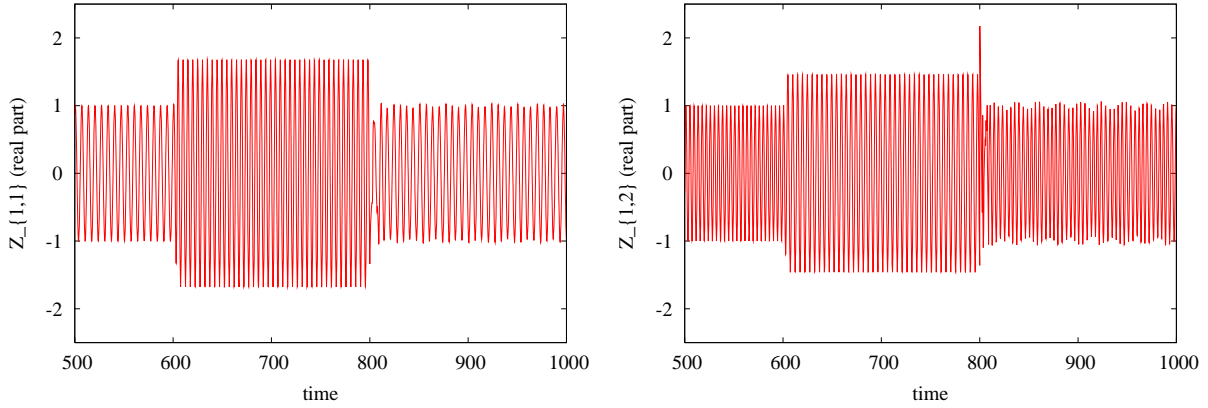


Figure 5.11: Exemplary trajectories (real part) of an oscillator in ensemble 1 (left panel) and in ensemble 2 (right panel) stimulated with mixed nonlinear delayed feedback. The mixing parameter ϵ is set to 0.675. The timing of switching on coupling and stimulation terms is the same as used for figure 5.10.

backward coupling to ensemble 2 (see equation 5.29) should also reach a minimum for $\epsilon = 0.675$. For the minima of $\langle R_2(t) \rangle_{T_S}$ all three contributions given by the global coupling to the mean field 2, the forward coupling of ensemble 1, and the stimulation signal have to be taken into account. In order to understand their interplay, these signals are investigated for synchronization in the following. As all signals considered here are complex, they can be represented by a phase and an amplitude at each point in time. For mean field 1 with $\bar{Z}_1(t) = \bar{X}_1(t) + \bar{Y}_1(t)$, mean field 2 with $\bar{Z}_2(t) = \bar{X}_2(t) + \bar{Y}_2(t)$, and the stimulation signal with $S(t) = \bar{X}_S(t) + \bar{Y}_S(t)$ these are given by

$$A_1(t)e^{i\Psi_1(t)} := \bar{X}_1(t) + \bar{Y}_1(t) \quad (5.38)$$

$$A_2(t)e^{i\Psi_2(t)} := \bar{X}_2(t) + \bar{Y}_2(t) \quad (5.39)$$

$$A_S(t)e^{i\Psi_S(t)} := \bar{X}_S(t) + \bar{Y}_S(t) \quad (5.40)$$

The phase differences between these signals are defined by

$$\varphi_{1,2}(t) = \Psi_1(t) - \Psi_2(t) \quad (5.41)$$

$$\varphi_{S,1}(t) = \Psi_S(t) - \Psi_1(t) \quad (5.42)$$

$$\varphi_{S,2}(t) = \Psi_S(t) - \Psi_2(t) \quad (5.43)$$

$$(5.44)$$

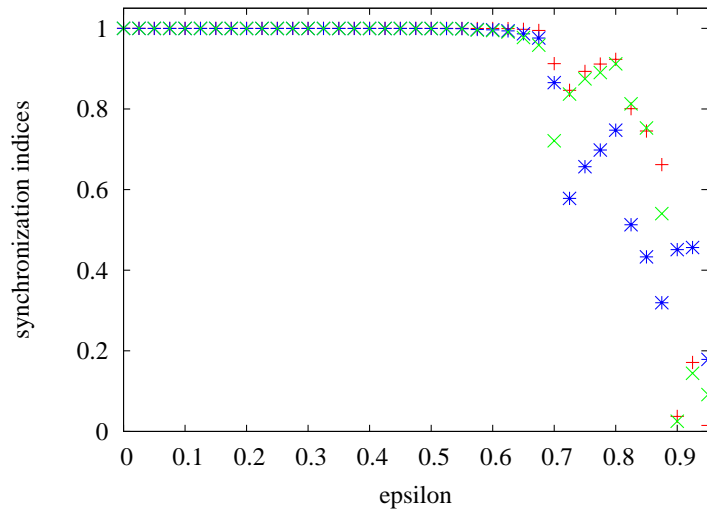


Figure 5.12: Red: synchronization index $R_{1,2}$ between the mean fields, blue: $R_{S,1}$, green: $R_{S,2}$

Finally, the *synchronization indices* $R_{1,2}$, $R_{S,1}$, and $R_{S,2}$ and the *mean phase differences* $\bar{\varphi}_{1,2}$, $\bar{\varphi}_{S,1}$, $\bar{\varphi}_{S,2}$ are defined by [Tas04]

$$R_{1,2}e^{i\bar{\varphi}_{1,2}} := \frac{1}{N_S} \sum_{j=1}^{N_S} e^{i\varphi_{1,2}(t_j)} \quad (5.45)$$

$$R_{S,1}e^{i\bar{\varphi}_{S,1}} := \frac{1}{N_S} \sum_{j=1}^{N_S} e^{i\varphi_{S,1}(t_j)} \quad (5.46)$$

$$R_{S,2}e^{i\bar{\varphi}_{S,2}} := \frac{1}{N_S} \sum_{j=1}^{N_S} e^{i\varphi_{S,2}(t_j)} \quad (5.47)$$

In the last equations N_S denotes the number of discrete time steps (step size: 0.1) considered during stimulation after the transient epoch. The synchronization indices, which are real numbers, are close to 1, if the associated phase differences do not change much over time around their means. The indices vanish provided the phase differences (modulo 2π) are uniformly distributed. Note that the mean phase differences are only well-defined, if their associated synchronization indices are larger than 0. In figure 5.12 the synchronization indices are plotted in dependence of ϵ . Both mean fields are strongly synchronized for $\epsilon \leq 0.675$, which is also the case for the stimulation signal relative to each mean field. For $0.7 \leq \epsilon \leq 0.8$ for the tested values of ϵ mean field 1 and mean field 2 as well as the stimulation signal and mean field 2 are also synchronized but to a lower degree than for $\epsilon \leq 0.675$. For $\epsilon \geq 0.9$ the mean fields are strongly desynchronized.

In the case of strong synchronization, the mean phase differences show the phase shift between signals (figure 5.13). These measures explain the dependence of the desynchronization of both mean fields on ϵ , as will be shown in the following. For $\epsilon = 0.075$ the mean phase difference $\bar{\varphi}_{S,1}$ is closest to π . This means for the oscillators in ensemble 2 that the main global influences (equation 5.29), the feedback stimulation and the forward coupling of ensemble 1, are nearly in

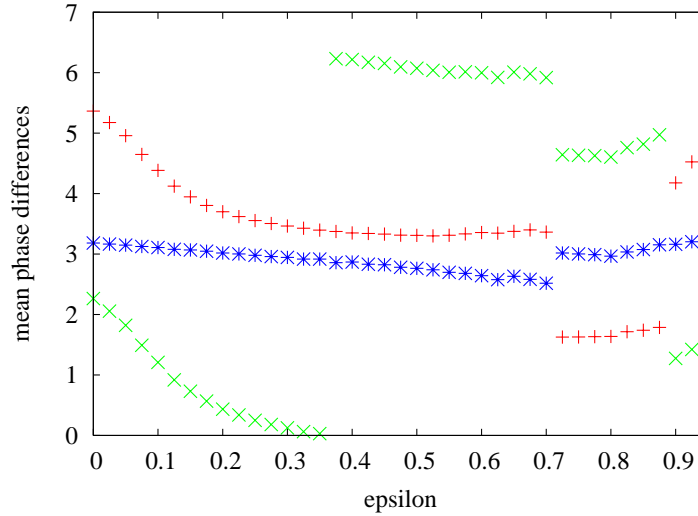


Figure 5.13: Mean phase differences. Red: $\bar{\varphi}_{1,2}$, blue: $\bar{\varphi}_{S,1}$, green: $\bar{\varphi}_{S,2}$

antiphase. The trajectories of $\bar{Z}_1(t)$, $\bar{Z}_2(t)$, and $S(t)$ are shown in figure 5.14 for this value of ϵ . The green curve displays the oscillation of mean field 2, whose amplitude is much smaller than for the other signals. Moreover, since the global coupling strength C_2 in ensemble 2 is 0.01 in this setup, the influence of the global coupling inside ensemble 2 is negligible for $\epsilon = 0.075$. The trajectories of the stimulation signal and mean field 1 exhibit a phase shift close to π . In general the amplitudes of $S(t)$ and $\bar{Z}(t)$ also depend on ϵ and have also to be taken into account, in order to quantify that value of ϵ where the sum of both signals is smallest. Here their amplitudes are nearly the same. For the oscillators in ensemble 2 this means that the global influences by the stimulation signal and the forward coupling ($C_{12} = 1$) cancel out for $\epsilon = 0.075$. This explains the first local minimum of $\langle R_2(t) \rangle_{T_S}$ (figure 5.8) as well as of $\Delta\omega_2^{S^{tim}}$ (figure 5.9). At this value of ϵ ensemble 2 is not driven by the first population due to the antiphase nonlinear delayed feedback. Its own global coupling is too small to induce a significant effect on its individual oscillators. Thus, these oscillators behave like uncoupled, i.e. they rotate on their own individual limit cycle with their individual natural frequency.

In order to understand the collapse of the driver around $\epsilon = 0.675$, the behavior of the mean phase difference between the mean fields, $\bar{\varphi}_{1,2}$, is important. They determine the global influences on the individual oscillators in ensemble 1 (equation 5.28). In figure 5.13 also the graph of $\bar{\varphi}_{1,2}(\epsilon)$ is given (red curve). Near $\epsilon = 0.675$ the mean phase difference is close to π which gives the analogous explanation for the collapse of the driver as for the first local minimum of $\langle R_2(t) \rangle_{T_S}$ discussed above. The oscillations of the mean fields for this value of the mixing parameter are displayed in figure 5.15. The signals are in antiphase and exhibit a similar amplitude. The coupling strengths for the global coupling of ensemble 1 and the backward coupling of population 2, C_1 and C_{21} , had been set 1 in this configuration. Hence the coupling terms in the equations for the individual oscillators in population 1 (equation 5.28) almost annihilate each other near $\epsilon = 0.675$. Oscillators in ensemble 1 are decoupled and desynchronized. Therefore ensemble 1 is not able to drive population 2 any more. The amplitude of mean field 2 also becomes small. Please note

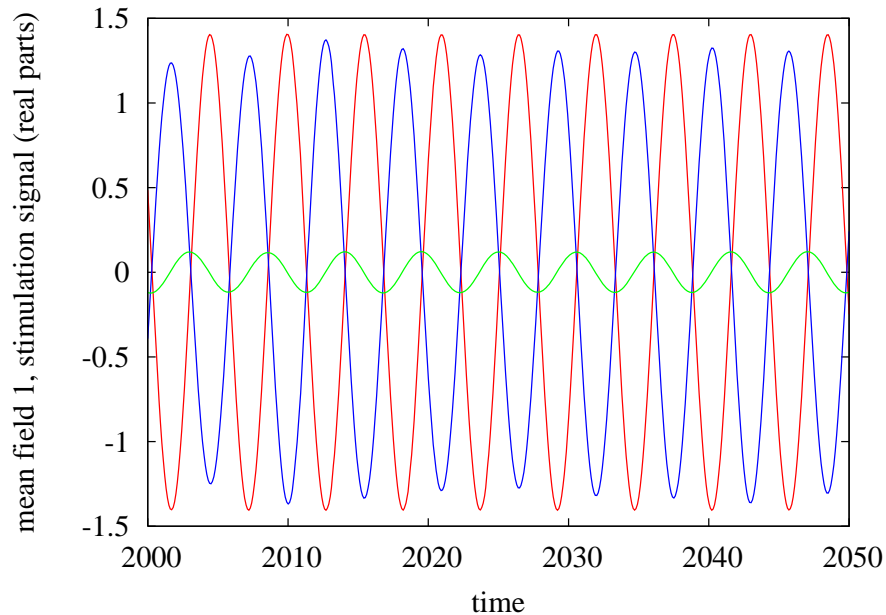


Figure 5.14: Trajectories of the stimulation signal (blue) and the mean fields (red: ensemble 1, green: ensemble 2) with mixed nonlinear delayed feedback ($\epsilon = 0.075$).

the different scaling in figure 5.15 compare to figure 5.14. Moreover the phase shift between the stimulation signal (blue curve in figure 5.15) and mean field 1 is still close to π for $\epsilon = 0.675$ which favors the desynchronization in ensemble 2.

To summarize the following can be concluded about the desynchronization and decoupling effects observed in both ensembles presented in figure 5.8 and figure 5.9. A slight increase of ϵ optimizes the nonlinear delayed feedback protocol for two interacting populations [PHT06b], because this leads to an antiphase setting of mean field 1 and the stimulation signal. A further increase of ϵ until 0.675 does not destroy the synchronization between both mean fields, but destroys the favorable phase shift between mean field 1 and the stimulation signal. For $0.5 \leq \epsilon \leq 0.675$ a second, dominating effect occurs: now the mean phase difference between the mean fields is close to π which makes oscillators in ensemble 1 decoupled. This leads to a desynchronization in this population and furthermore in ensemble 2, which is not driven by ensemble 1 any more.

5.3.3 Modeling ensembles by macroscopic oscillators

In order to understand the global behavior of both ensembles under the influence of mixed nonlinear delayed feedback, their mean fields are modeled by macroscopic oscillators. This should lead to an explicit description for the optimal values for ϵ in dependence of the parameters settings in

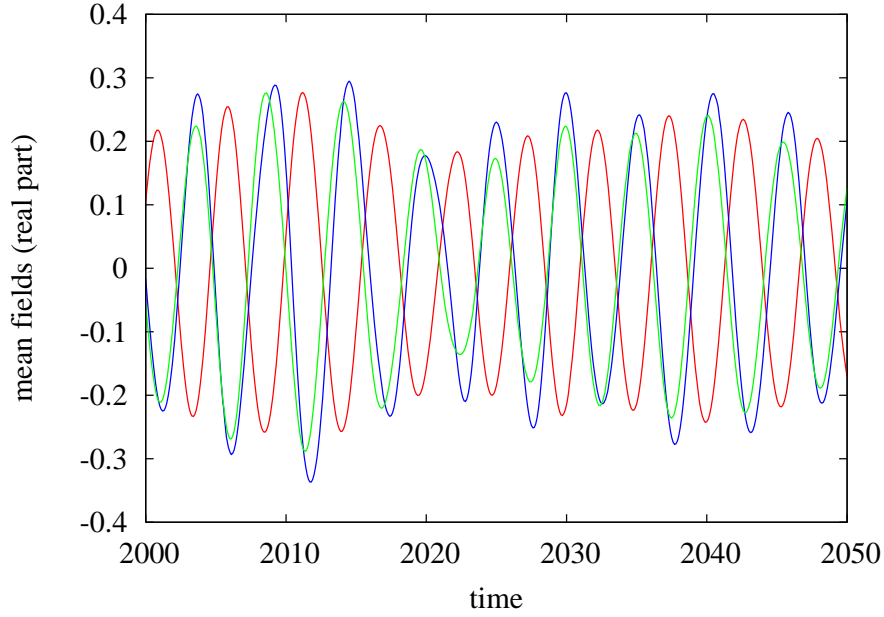


Figure 5.15: Trajectories of the stimulation signal (blue) and the mean fields (red: ensemble 1, green: ensemble 2) with mixed nonlinear delayed feedback ($\epsilon = 0.675$).

both ensembles. Two alternative approaches are studied here. The first one

$$\begin{aligned}
 \dot{\mathcal{Z}}_1(t) &= (C_1 - C_{crit} + i\Omega_{0,1} - |\mathcal{Z}_1(t)|^2)\mathcal{Z}_1(t) \\
 &\quad + C_{21}\mathcal{Z}_2(t) \\
 \dot{\mathcal{Z}}_2(t) &= (C_2 - C_{crit} + i\Omega_{0,2} - |\mathcal{Z}_2(t)|^2)\mathcal{Z}_2(t) \\
 &\quad + C_{12}\mathcal{Z}_1(t) + S(t)
 \end{aligned} \tag{5.48}$$

models the mean fields $\bar{\mathcal{Z}}_1$ and $\bar{\mathcal{Z}}_2$ at the onset of synchronization by the oscillators \mathcal{Z}_1 and \mathcal{Z}_2 , respectively, with C_{crit} according to equation 5.34 [RP04b, Kur84]. $\Omega_{0,1}$ and $\Omega_{0,2}$ denote the mean natural frequency of the individual oscillators in ensemble 1 and ensemble 2, respectively.

For the second model, it is assumed that in the driving ensemble 1 the individual oscillators do not differ much concerning amplitude and phase, which is true for a strongly synchronized ensemble. Mean field 1 is then described by a single representative oscillator of the first ensemble. In this case it holds

$$\mathcal{Z}_1(t) = \frac{1}{N_1} \sum_{j=1}^{N_1} Z_{j,1}(t) \approx Z_{j,1}(t) \tag{5.49}$$

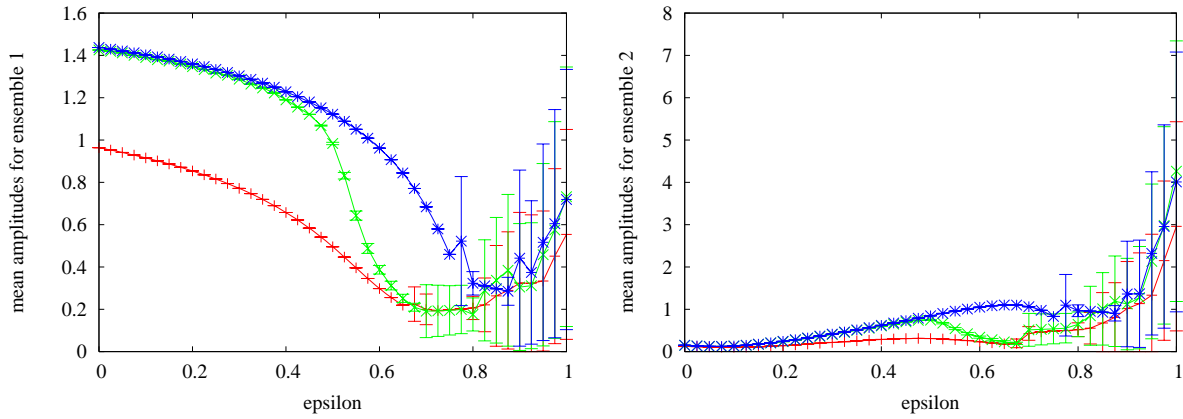


Figure 5.16: Mean field amplitudes with standard deviations from numerical simulations with mixed nonlinear delay feedback. Left: for ensemble 1, right: for ensemble 2. Red: according to the macroscopic approximations given by equations 5.48. Blue: according to the macroscopic approximations given by equations 5.51. Green: results from 200 microscopic oscillators in each ensemble obeying equations 5.28 and 5.29.

for all j . The mean field equation of ensemble 1 (see also equation 5.28) without backward coupling to the second ensemble becomes

$$\begin{aligned}\dot{\mathcal{Z}}_1 &= \frac{1}{N_1} \sum_{j=1}^{N_1} \dot{Z}_{j,1}(t) = \frac{1}{N_1} \sum_{j=1}^{N_1} (a_{j,1} + i\omega_{j,1} - |Z_{j,1}(t)|^2)Z_{j,1}(t) + C_1 \mathcal{Z}_1 \\ &= \left(\frac{1}{N_1} \sum_{j=1}^{N_1} a_{j,1} + i\Omega_{0,1} - |\mathcal{Z}_1(t)|^2 \right) \mathcal{Z}_1(t) + C_1 \mathcal{Z}_1\end{aligned}\quad (5.50)$$

The differential equations for the model of interacting populations are then given by

$$\begin{aligned}\dot{\mathcal{Z}}_1(t) &= (C_1 + \mathcal{A}_1 + i\Omega_{0,1} - |\mathcal{Z}_1(t)|^2)\mathcal{Z}_1(t) \\ &\quad + C_{21}\mathcal{Z}_2(t) \\ \dot{\mathcal{Z}}_2(t) &= (C_2 - C_{crit} + i\Omega_{0,2} - |\mathcal{Z}_2(t)|^2)\mathcal{Z}_2(t) \\ &\quad + C_{12}\mathcal{Z}_1(t) + S(t)\end{aligned}\quad (5.51)$$

with the same mean field approximation of the driven population as in the first model. Here $\mathcal{A}_1 := \frac{1}{N_1} \sum_{j=1}^{N_1} a_{j,1}$, which is equal to 1 for the tested parameter settings defined in the previous section. In both modeling approaches the stimulation signal is given by equation 5.30 whereby \bar{Z} obeys

$$\bar{Z}(t) = (1 - \epsilon)\mathcal{Z}_2(t) + \epsilon\mathcal{Z}_1(t)\quad (5.52)$$

In order to check the validity of the different approximations, the amplitudes for the interacting macroscopic oscillators in equations 5.48 and 5.51, respectively, with mixed nonlinear delayed feedback have been calculated in numerical simulations. In figure 5.16 the values are plotted together with the mean field amplitudes of the simulations with 200 microscopic oscillators in each ensemble (equations 5.48). For $\epsilon \leq 0.4$ the approximations according to equations 5.51 predict

the mean field amplitudes of the ensembles in an appropriate manner. In this range the driving ensemble is strongly synchronized. For the collapsed driver and the desynchronized population 2 ($0.6 \leq \epsilon \leq 0.8$) equations 5.48 can serve as a model. For larger values of ϵ the first model seems to be the better approximation, but the strong fluctuations of the mean fields in this range do not allow further conclusions. For the whole range of ϵ both models are not applicable.

In this section an enhanced desynchronization of interacting limit cycle oscillators by mixed nonlinear delayed feedback has been presented. Two effects for different regimes of ϵ are qualitatively understood. For small values of ϵ the driving ensemble is nearly untouched but the driven ensemble can be stronger desynchronized than for $\epsilon = 0$. For $0.6 \leq \epsilon \leq 0.8$ the antiphase shift of the mean fields leads to a breakdown of the driver and to a second local minimum with respect to the synchronization in ensemble 2. In this range of ϵ the desynchronization of both populations has also been observed for different settings of the delay τ , the individual radii $a_{j,k}$, and the mean natural periods of both ensembles (not shown here). Moreover, the protocol gives similar results in ensembles of phase oscillators, as used e.g. in [THP06]. This protocol shows the benefit of mixing the mean fields for the stimulation of interacting populations of oscillators. In applications, the mixing parameter could be used to allow a stronger desynchronization of the driven population only. The mixing parameter can also be tuned in a way that the oscillators in both ensembles are decoupled, even without direct stimulation of the driving population.

Some open questions require further investigations. The increase of the mean order parameters, the fluctuation of the mean fields, and their loss of synchronization for large values of ϵ has to be understood. This is critical for applications. The modeling of the interaction of both mean fields has to be improved, in order to understand quantitatively the mechanism of mixed nonlinear delayed feedback.

In the next chapter the linear delayed feedback and the nonlinear delayed feedback protocol without mixing is exploited in an MEG experiment. For this, the realtime MEG system implemented at Jülich, which features the possibility to use the reconstructed current density distribution in the brain for neurofeedback, will also be described.

Chapter 6

Realtime MEG

In this work the Gaussian weighted Minimum Norm method proved the best linear method with respect to localization accuracy in a test of state-of-the-art distributed source models. It has been implemented in a realtime MEG system at the Research Center Center Jülich. A first benefit of this approach is to deliver the reconstructed current density distribution to the experimenter and physician, respectively, online to enable calibration of stimulation parameters during the experiments. A further feature is to exploit the reconstructed current density in selected voxels for neurofeedback. This offers a wide range of new feedback experiments which are based on physical models.

The tested linear and nonlinear delayed feedback protocols are hypothesized to enable new forms of therapies for neurological diseases [RP04b, PHT06a, THP06]. Brain lesions, for example, are frequently accompanied by abnormal low frequency magnetic activity [BdJS⁺03]. A suppression of such oscillations could result in a more functional regeneration of the brain tissue.

The aim of the presented experiment is the downregulation of a physiological brain rhythm. This would enable to test the functional meaning of such brain rhythm [Tas02] in future experiments. For example the brain rhythm around 40 Hz seems to be responsible for the binding of discrete stimulus components into coherent wholes during visual object perception [EM98]. In the experiment described at the end of this chapter the *alpha rhythm* (8 – 12 Hz) is investigated, because it can be manipulated by relatively simple visual stimulation setups.

In the following section the workflow of the realtime system as well as its implementation is shortly described. Its correctness will be shown with the aid of phantom experiments, i.e. via measurements of a brain dummy with a known and controllable current density distribution.

6.1 Implementation

The aim is to calculate the current density distribution via the solution of the Tikhonov regularization in equation 2.14 which is repeated here

$$\vec{j} = (L^T L)^{-1} \Phi^T (\Phi (L^T L)^{-1} \Phi^T + \alpha 1)^{-1} \vec{m} \quad (6.1)$$

For a fixed lead field matrix Φ , a fixed weighting matrix L and a constant setting of the regularization parameter α this gives a fixed linear mapping

$$A = (L^T L)^{-1} \Phi^T (\Phi (L^T L)^{-1} \Phi^T + \alpha 1)^{-1} \quad (6.2)$$

between the currently acquired signals \vec{m} and the desired reconstructed current density distribution. According to the benchmark of inverse methods in this thesis the used weighting matrix L is defined according to the Gaussian weighted Minimum Norm solution (see section 3.1.1). The regularization parameter α has to be set by the experimenter. Before the calculation of matrix A a preliminary configuration has to take place in the experiment, in order to define the position of the source space and to calculate the lead field matrix. This is described in the next paragraph. The implementation of this routine with respect to an online usage has been an essential part of this work.

Before the MEG experiment an MRT measurement of the brain of interest is performed. With the aid of the MRT image a sphere for the model of the electrical volume conductor is fitted to the head (see section 2.2). The user of the realtime MEG system has to decide for one of four spherical segments fitted to the head, which defines four alternative positions of the source space (for a back source space see e.g. figure 3.4). The choice depends on the specific experiment. Moreover the number of used sensors is set by the experimenter. In a next step reference coils are fixed at the surface of the head of the subject. Their positions in the associated coordinate system of the MRT image and the source space, respectively, is determined by matching the surface of the head to the MRT image. Magnetic fluxes are generated in the reference coils with the aid of small electrical currents which are detected by the MEG sensors. This gives their positions relative to the source space. Afterwards the source space grid is generated as well as the forward solution, i.e. the lead field matrix giving the sensitivity of each applied detector with respect to the source space grid points. Finally, matrix A can be calculated according to equation 6.2. During the experiments this matrix can be updated in order to correct for head movements of the subject, which changes the position of the sensors relative to the source space. This update of matrix A takes only a few minutes during which no further data is being acquired.

The inverse mapping A given by GaussMN is plugged into the online and realtime MEG system whose workflow is sketched in figure 6.1. This work contributed the inverse mapping and the specification of the feedback protocols for the experiments. For details about the hardware implementation and the user interface see [Ron06]. In order to describe the usage of the reconstructed current densities, the workflow of the system is shortly described in the next paragraph.

Each scanned set of binary MEG signals, read from the MEG system, is fed into a *Field Programmable Gate Array* (FPGA). In order to achieve the same physical unit for each sensor, signals are scaled here appropriately and parsed into a suitable format for the succeeding *Digital Signal Processor* (DSP). A DSP enables a parallel and very fast calculation of algebraic operations. With this device the reconstruction of the current densities by multiplying matrix A with the magnetic fluxes can be performed in a time less than one millisecond for a limited number of voxels (of the order of 10). This makes it possible to reconstruct the current densities with the same high rate (≈ 1 kHz) that is used for the detection of the magnetic fluxes and with a fixed latency. No incoming signals are lost or ignored. Therefore this process is considered as *realtime*. The fixed latency between the measurement of the magnetic fluxes and the entry in the FPGA has been determined to be around 30 ms [Ron06]. The realtime calculated signals can be used for

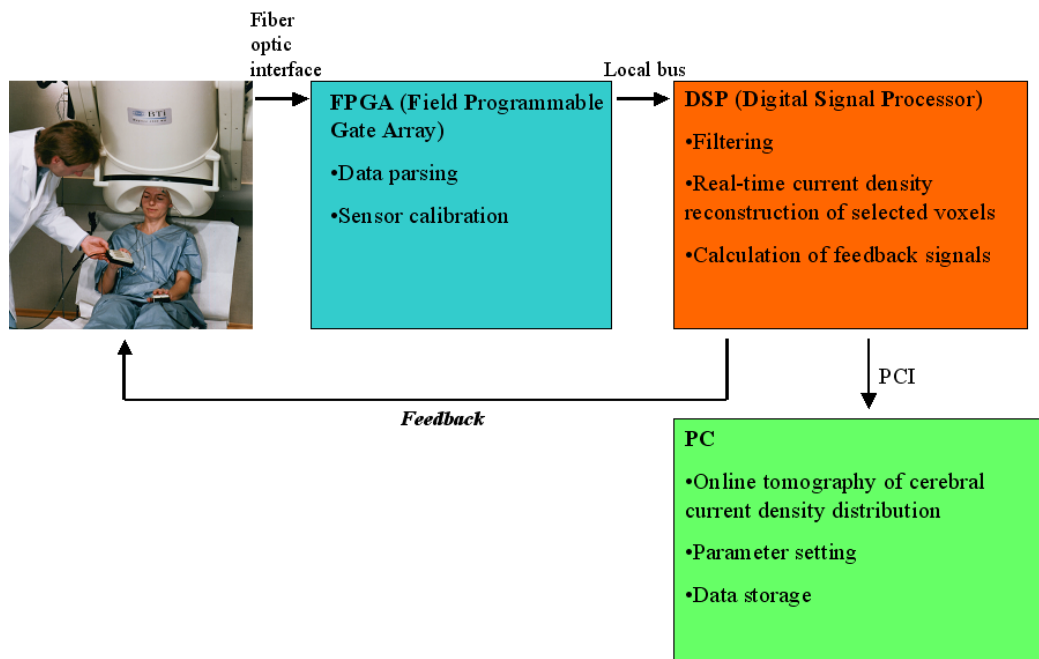


Figure 6.1: Sketch of the workflow of the online and realtime MEG system

feedback which will be demonstrated in an experiment in section 6.3 of this chapter. Furthermore, the MEG signals are sent to a Personal Computer where the current density distribution is reconstructed with respect to the entire source space approximately four times per second which is called *online* in this work. This three-dimensional online tomography of the current density distribution has been tested in phantom experiments described in the next section.

6.2 Phantom tests

The correctness of the implementation of the online MEG system and the accuracy of the Gaussian Weighted Minimum Norm method has been tested experimentally with the aid of a phantom (figure 6.2). Inside the non-metallic shell of the phantom five current dipoles at different positions can be switched on independently. The strength of each dipole is a sine whereby the amplitude and the frequency can be set outside the shielding room. In figure 6.3 the visualization of the current density distribution inside the source space is shown during the online reconstruction of one of the current dipoles. In this figure important information for the experimenter is emphasized with purple arrows. The time course of a selected sensor as well as of the current density in a selected voxel can be gathered with a temporal resolution of 1 ms. Also presented is the current position of maximum activity inside the source space.

Each single dipole has been reconstructed with the aid of the online system using 100 detectors. The resulting localization errors are displayed in table 6.1. Each original position can be reconstructed relatively precisely. The mean displacement is 0.9 cm, which is in the same range of the results from the numerical simulations (chapter 3). Note that the magnetic fluxes in the sensors



Figure 6.2: The phantom before the measurement in the MEG system. Reference coils are fixed to the *head* of the phantom in order to measure the positions of the MEG sensors relative to the head.

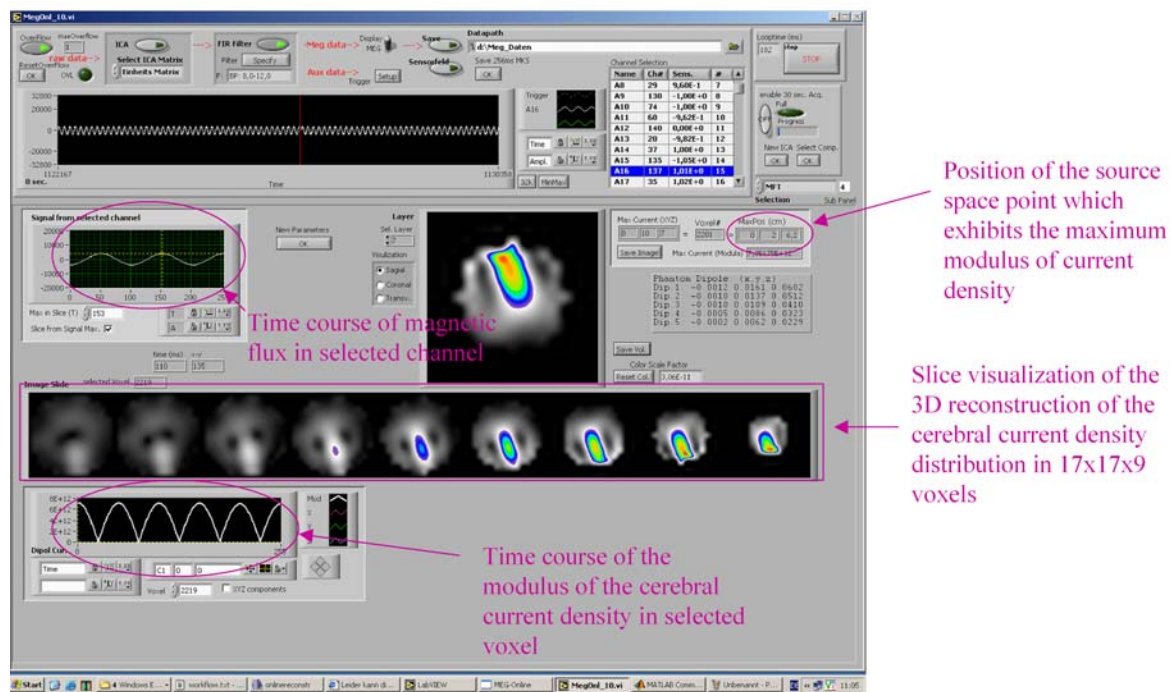


Figure 6.3: Graphical user interface for the online tomography of the reconstructed current density distribution. The screen shot has been taken during a phantom experiment. In the slice visualization of the interpolated source space a red color indicates large activity, i.e. a large amplitude of the current density vector in the associated voxel. Dark-gray colored voxels show relative low values of activity.

	coordinates (cm)			reconstructed position (cm)			localization error (cm)
	x	y	z	x	y	z	
<i>Dipole no. 1</i>	-0.1	1.6	6.0	0.0	2.0	6.2	0.4
<i>Dipole no. 2</i>	-0.1	1.4	5.1	0.0	2.0	5.3	0.7
<i>Dipole no. 3</i>	-0.1	1.1	4.1	0.0	2.0	4.4	1.0
<i>Dipole no. 4</i>	-0.1	0.9	3.2	0.0	2.0	3.6	1.2
<i>Dipole no. 5</i>	0.0	0.6	2.3	0.0	1.0	3.6	1.4
						<i>average:</i>	<u>0.9</u>

Table 6.1: Displacement results of a phantom experiment. Left column: actual position of the single current dipoles in source space coordinates given by the manufacturer, middle column: positions of maximum activity during online reconstruction of each dipole, right column: euclidian distance between the actual positions and the reconstructed ones. The regularization parameter of the Gaussian weighted Minimum Norm method has been set to $\alpha = 10^{-15}$.

generated with the aid of the phantom have been orders of magnitude larger than those observed in experiments with human subjects. The dipoles in the table are ordered increasingly concerning their depth inside the source space, i.e. concerning their mean distance to the sensors. As expected from the simulations the localization accuracy decreases with increasing source depth.

6.3 Visual delayed feedback in an MEG experiment

In this section a first application of the realtime MEG system in form of a neurofeedback experiment is presented. For the calculation of the feedback signals in the experiment the linear and nonlinear delayed feedback methods [RP04a, PHT05b] presented in the preceding chapter are applied.

The alpha rhythm is defined as the brain rhythm between 8 – 12 Hz (see e.g. [EM98]). It is observed in EEG and MEG measurements during wakefulness of the subjects over occipital brain areas with large amplitudes at the visual cortex due to strongly synchronized neural populations [dSI05]. The aim of the presented experiment is to regulate the synchronization of neurons involved in the alpha rhythm with the aid of linear and nonlinear delayed feedback, respectively. For this, the measured magnetic field around the head of the subject is processed according to each specific protocol (see below) with the aid of the realtime MEG system. The feedback signal is coded into a visible light signal whereby the intensity of the white light depends proportionally on the value of the calculated feedback signal for each time step. Because the alpha rhythm shows large amplitudes in the visual cortex, signals are measured in this area and fed back by visual stimulation. The light signal is displayed to the subject by special glasses coupled to the realtime MEG system (see figures 6.1 and 6.4). Both eyes are stimulated with the same signal. The realtime MEG system guarantees a constant latency between the generation of the magnetic fluxes in the sensors and the display of the feedback signals in the glasses. Before the stimulation in a preliminary measurement the reconstructed current density distribution inside the visual cortex area V1 has been investigated with the aid of the online tomography. This area is defined by an extrapolation of the associated brain map [ZSPGA02] onto the back source space grid. A voxel inside this region has been chosen which exhibited large power in the alpha band. In the next step a *Principal Component Analysis* (PCA) of the time course of the reconstructed current



Figure 6.4: Glasses worn by the subject during the feedback experiment. The feedback signals, coded as white light with time-varying intensities, are fed into both glasses by fiber optic cables and shielding plastic tubes (black cable fixed to the front of the right tube). The light is displayed to the subject with the aid of diffusing screens at the back of the tubes.

density in this voxel of interest was performed. With the aid of this PCA the main direction of the three-dimensional current density vector has been calculated. From the lead field matrix the detector (in the following called sensor of interest) was identified that showed the strongest sensitivity along the main direction of the current density in the voxel of interest. For this, the maximum of the projection of the corresponding lead field vectors onto the main direction has been determined. For the feedback protocols, all detector signals have been bandpass-filtered between 8 – 13 Hz with the online system [Ron06].

In the following paragraphs the tested stimulation protocols will be introduced. The latency, which depends on the applied bandpass-filtering, is a crucial parameter for the performance of feedback methods [HS05]. In addition to the already described consumed time between the generation of the magnetic fluxes and the entry in the FPGA, for each applied feedback protocol a specified amount of latency occurs (for details see [Ron06]).

Linear delayed sensor feedback The signal of the detector of interest has been taken as the base of this protocol. The magnetic flux measured at a time τ before the actual time $m_f(t - \tau)$ (see also equation 5.1) was coded into the light intensities. For this, first a constant positive offset was added to the measured fluxes, in order to get a positive range of values. Finally the magnetic fluxes were scaled into the values for the light intensities for feedback by an appropriately chosen proportionality factor, which determined the strength of the stimulation. An additional latency for the feedback has to be taken into account which has been approximately 30 ms.

Nonlinear delayed sensor feedback Again the detector of interest is considered. Its signal $m_f(t)$ is preprocessed according to appendix D. The variable $X(t)$ in appendix D corresponds to $m_f(t)$ for this protocol. The preprocessed signal (equation D.7 with $X(t) \equiv m_f(t)$) is shifted to a

positive range and scaled to the light intensities like in the linear sensor feedback. An additional latency of also 30 ms occurs for this protocol.

Linear delayed voxel feedback In this case, the current density $j_f(t)$ along the main direction in the voxel of interest is used. Otherwise the stimulation signal is built analogous to the linear sensor feedback, i.e. the current density $j_f(t-\tau)$ was coded into the light intensities by shifting it to a positive range and scaling it to the light intensities. Note that for both voxel feedback protocols an additional latency of about 500 ms has to be considered for technical reasons [Ron06].

Nonlinear delayed voxel feedback Current density $j_f(t)$ is processed for the feedback signal like $m_f(t)$ in the nonlinear delayed sensor feedback. Thus $X(t)$ in appendix D corresponds to $j_f(t)$ for this protocol. The preprocessed signal according to equation D.7 with $X(t) \equiv j_f(t)$ is shifted to a positive range and scaled to the light intensities.

Control stimulation For each feedback protocol it is important to check, if each specific correlation between the current stimulation signal and the brain activity shortly before (< 1 s), is actually responsible for the result of the stimulations. Hence a control protocol is necessary. For this, the time series of light intensities displayed to the subject is stored for each feedback experiment (see figure 6.9 for examples). Several minutes after the feedback protocol, the subject is stimulated by the same time course of light intensities as before without knowing, that this time the current brain activity is not taken into account for the stimulation. In other words, as a control the subject is presented a *replay* of the flickering movie watched during the feedback experiment. The subject has been measured and stimulated in a lying position. Their eyes have been opened during the whole runs. A damped background lighting has been present inside the cabin. For the tested stimulation protocols each run consisted of five stimulation sequences. Between them the stimulation has been switched off. The length of each on- and off-period, respectively, has been randomly chosen between 9 and 11 sec. The attention of the subject has been drawn by short flashes (see e.g. figure 6.5) with a randomly chosen interflash-interval between 10 and 25 sec.

The results for one healthy subject (male, 31 years old), who showed a strong alpha rhythm with open eyes, will be presented in the following. The delay in all presented feedback results was $\tau = 30$ ms. For each protocol four runs have been performed. In figure 6.5 the course of the power spectral densities for the current density in the voxel of interest is given exemplarily during one run with linear delayed sensor feedback. The current density is reconstructed by GaussMN using the band-pass filtered (8 – 13 Hz) detector signals. Furthermore the main direction of the current density, estimated by the PCA before the stimulation protocol, is used. The spectrograms have been calculated via a sliding-window Fourier transform (Hanning windows with 50 % overlap) with 4096 time points for each window which gives a length of about 4 s for the applied scanning frequency of 1017 Hz. Sequences where the stimulation was switched on (*on-sequences*) are indicated by black rectangles. The narrow black bars along the spectrogram indicate the attention flashes. A suppression of the alpha rhythm by the stimulation can be observed especially at the beginning of the run. At the bottom of this figure power spectral densities are averaged over the on- and off-sequences, respectively. For this, the Welch method with Hanning windows was ap-

plied [SM97] with the same setting for the window length and overlap between time windows as mentioned before. The sharp drop-off of the power spectral densities at 20 Hz in this plot has its reason in a minimum of the transfer function of the applied online filter at this frequency. Around 10 Hz the mean power densities show a decrease during stimulation. The peak in the alpha band for this subject has been at about 11 Hz without stimulation. The power spectrum densities of the associated replay experiment are given in figure 6.6. No significant difference between the results of both protocols can be stated. For this subject both stimulation forms, the linear delayed sensor feedback and its control, evoke a suppression of the alpha rhythm in the voxel of interest.

In contrast the nonlinear delayed sensor feedback (figures 6.7 and 6.8) exhibits a difference between the actual feedback and the control protocol. Especially the power at frequencies between 10 Hz and 11 Hz is decreased by the feedback. Moreover the position of the peak of the spectrum is shifted to circa 12 Hz. In contrast the replay stimulation does not produce a change compared to the off-sequences. Please note that the suppression of the alpha rhythm is enhanced by the nonlinear delayed sensor feedback compared to the linear one (figures 6.5 and 6.7), although the mean power of the stimulation signal for the nonlinear delayed sensor feedback is much smaller than for the linear delayed sensor feedback (figures 6.9). Due to the nonlinearity of the underlying feedback method the time course in the right image of this figure looks much more irregular.

The voxel feedback protocols compared to the corresponding sensor feedback produced qualitatively very similar results. The linear delayed voxel feedback did not show a difference compared to its control stimulation. For the nonlinear delayed voxel feedback and its replay the power spectral densities of the current density in the voxel of interest along the main direction are plotted in figure 6.10. With the Welch method the data have been averaged again over the on- and off-sequences, respectively, of all four performed runs of each protocol. The suppression of the alpha rhythm due to the feedback can be gathered. In contrast this effect is much less pronounced, if the replay is applied.

Comparing the nonlinear delayed voxel feedback and the nonlinear delayed sensor feedback concerning their performance in suppressing the alpha rhythm favors the voxel feedback. To show this, in figure 6.11 for both protocols a single representative run is taken. In the presented maps the power spectral densities between 9 and 11 Hz during the on- and off-sequences, respectively, are averaged for the signals of each sensor. In the right images the difference of the mean power spectral densities between the sequences with and without stimulation are given. They are shown in a normalized manner with respect to the amplitude of the undisturbed alpha rhythm.

Concerning the off-sequences, sensors near the top of the head show the lowest values of the averaged power spectral densities. The MEG system in Jülich uses magnetometers as sensors for detecting the magnetic field (section 2.1). These detectors are least sensitive to current dipoles, which are situated directly below the sensor. (see figure 27 on page 446 in [HHR⁺93]). Because of this complicated shape of the lead fields, please note that the location of the alpha rhythm generators cannot be easily gathered from figure 6.11.

The maps show that the power in all sensors is considerably reduced by both nonlinear delayed feedback protocols. The suppression relative to the unstimulated state (right images in figure 6.11) measured in sensors near the top of the head is lower than for the remaining detectors. The voxel feedback exhibits an enhanced suppression compared to the sensor feedback in all detectors.

In the visual experiment discussed here also delays between 10 – 100 ms other than 30 ms have

been tested, but the results had no obvious dependence on this setting. Varying also the stimulation strength, no boosting of the oscillations has been observed in contrast to the simulations with linear delayed feedback (figure 5.2).

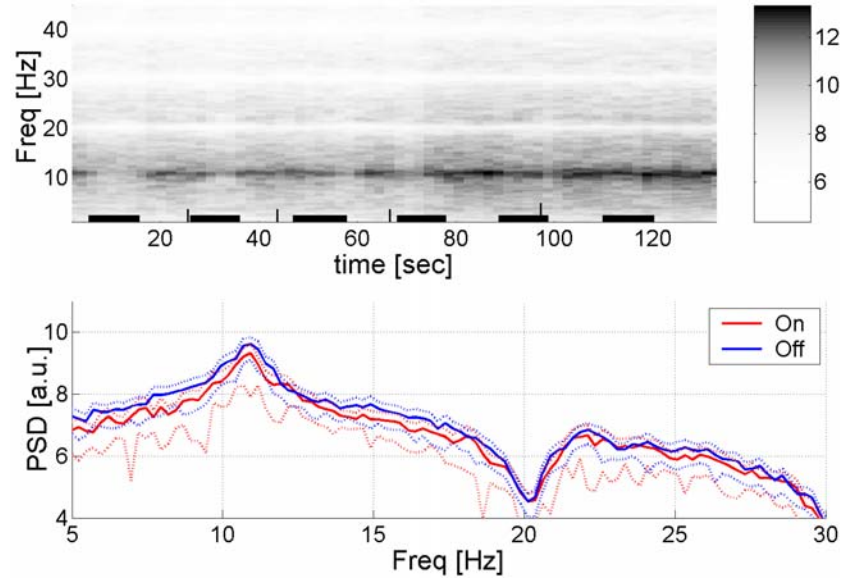


Figure 6.5: *Linear delayed sensor feedback*. Top: spectrograms (a.u.) of the current density in the voxel of interest for one run with logarithmic scaling. The black rectangles show the stimulation sequences whereas the narrow black bars indicate the attention pulses. Bottom: power spectral density (PSD, logarithmic scaling) distributions along with standard deviations (dotted lines) averaged over the sequences with and without stimulation, respectively.

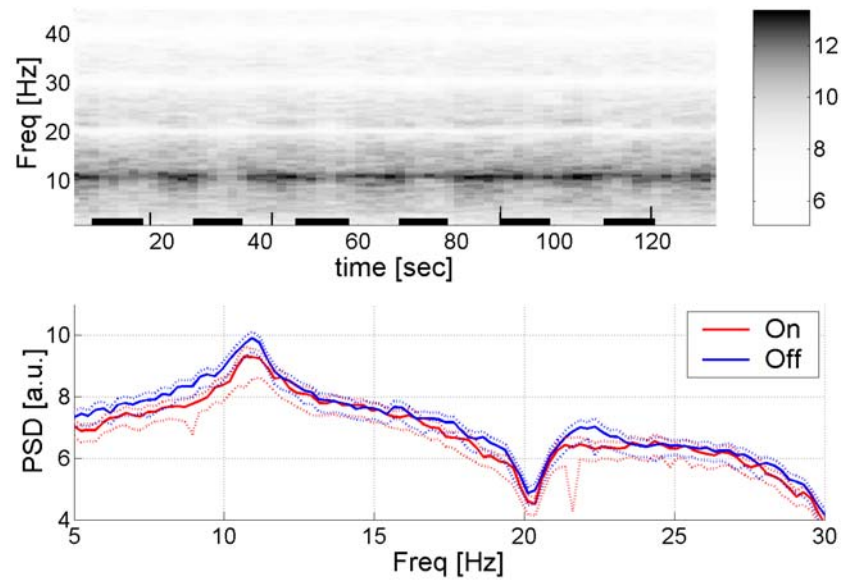


Figure 6.6: *Replay of the linear delayed sensor feedback*. Top: spectrograms of the current density in the voxel of interest during the run. Bottom: mean power spectral density distributions for the on- and off-sequences, respectively.

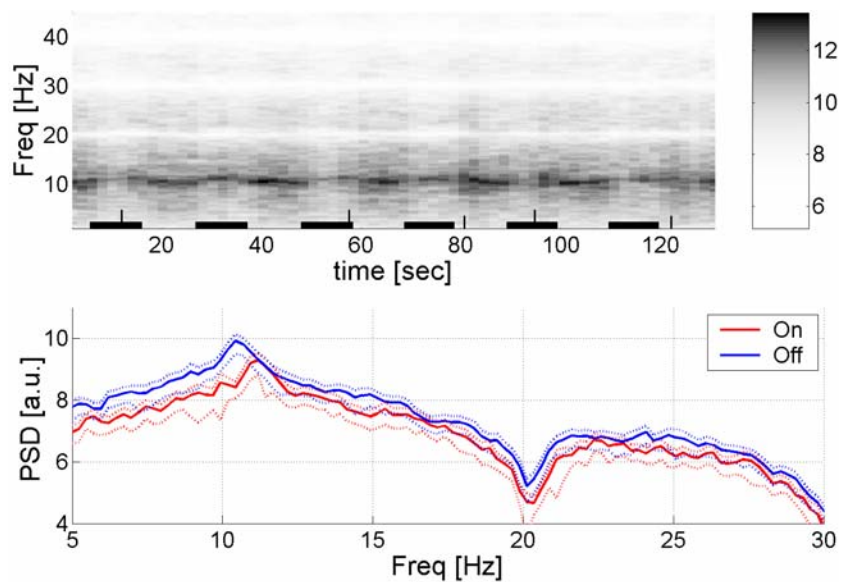


Figure 6.7: *Nonlinear delayed sensor feedback*. Top: spectrograms of the current density in the voxel of interest during one run. Bottom: mean power density distributions for the on- and off-sequences, respectively.

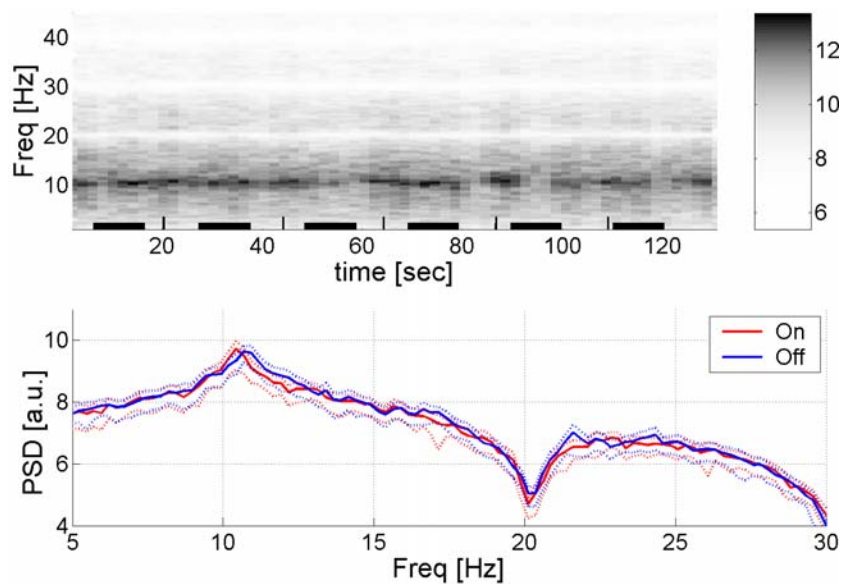


Figure 6.8: *Replay of the nonlinear delayed sensor feedback*. Top: spectrograms of the current density in the voxel of interest during one run. Bottom: mean power density distributions for the on- and off-sequences, respectively.

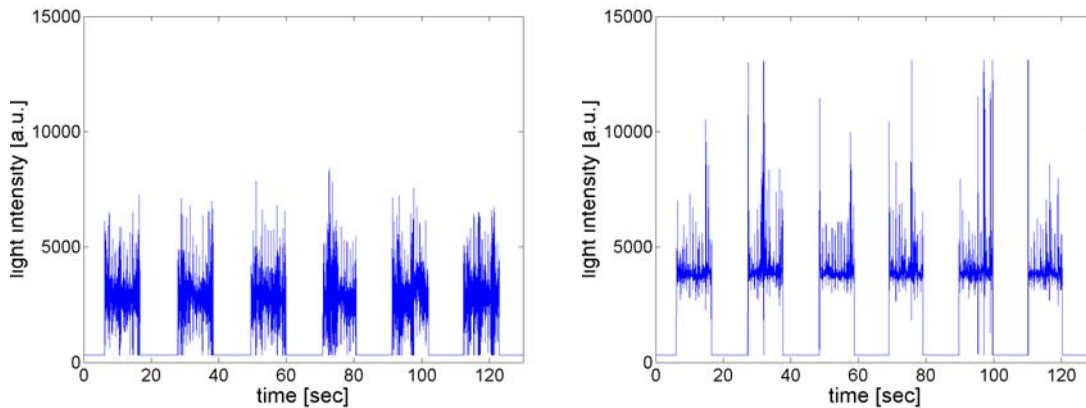


Figure 6.9: Left: time course of the intensities of the stimulation signal for a run with a linear delayed sensor feedback protocol. Right: time course for nonlinear delayed sensor feedback. In this example the mean power of the time series during stimulation for the linear feedback is about 2.5 times larger than for the nonlinear feedback.

In drawing conclusions from the results of the presented experiment, the small amount of data has to be taken into account. Even in a single subject the variability is considerable, as the large standard deviations in the plots show. To reduce them, longer runs than shown here have also been tested, but the degree of the suppression has been significantly reduced in the course of these runs (see top image in figure 6.5). Subjects are necessary which show a strong alpha rhythm in the unstimulated state for this kind of experiment to observe significant effects.

Ensembles of globally coupled limit cycle oscillators and phase oscillators, respectively, which motivated the usage of the linear and nonlinear feedback for the regulation of brain rhythms [RP04b, PHT05b], serve as a starting point for modelling the neural system under consideration. In fact, the human visual system, which processes stimulations of the retina into cerebral currents, is extremely complicated. It consists of networks of neural populations. Distinct neural pathways, involving also other parts of the cortex besides the visual cortex, are responsible for different aspects of vision, like spatial and object information. The visual cortex itself has feed-forward connections that relay information from lower to higher visual cortical areas, but there are also horizontal, within-area and feedback connections. Moreover the degree of attention of the subject plays a key role in the processing of visual stimulations (see [LR00] for a review).

The nonlinear delayed feedback shows a difference in the results for the real feedback and for its associated control protocol. The replay of the nonlinear delayed feedback slightly suppresses the brain oscillations, but to a lower degree than the other protocols. For each of the feedback runs there was a control run whose stimulation signal was exactly the same. Therefore, concerning the nonlinear protocols the suppression phenomenon cannot appear just due to an arbitrary flickering drawing the subject's attention. But it strongly supports the conclusion that the nonlinear delayed feedback protocol, i.e. this special shape of correlation between the stimulation signal and the brain activity measured shortly before, actually is the reason for the large suppression of the alpha rhythm in this subject. The weaker but still present effect evoked by the replay of the nonlinear delayed feedback is not surprising. The flickering may also lead to a suppression of the rhythm in the subject, but to a lower degree than the linear delayed feedback, if one considers the

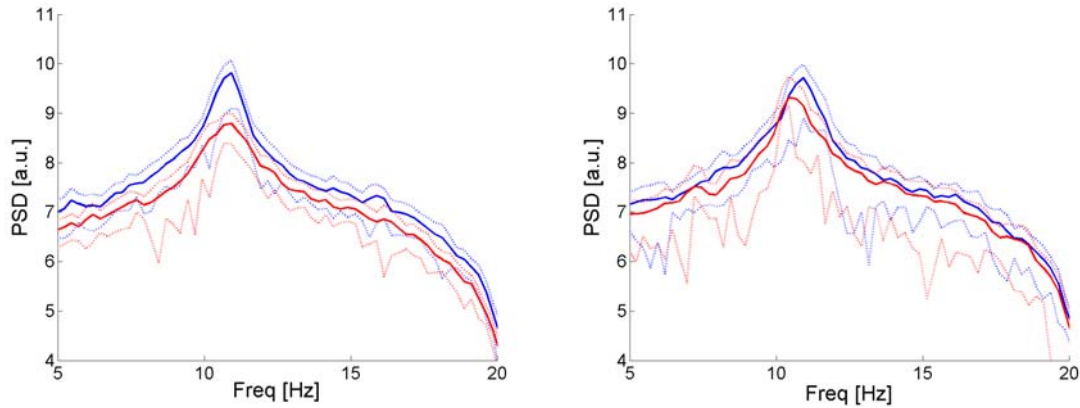


Figure 6.10: Left: *nonlinear delayed voxel feedback*. The mean power spectral densities of the current density (main direction) in the voxel of interest are shown for the on- (red) and off-sequences (blue). Values are averaged over the on- and off-sequences, respectively, of four runs with the same stimulation protocol. Right: Corresponding results from the *replay of the nonlinear delayed voxel feedback*. The current densities are reconstructed with the GaussMN method using the online bandpass-filtered sensor signals.

mean power in the stimulation signals (figure 6.9).

Using the reconstructed current density in the voxel of interest for the feedback enhances the desynchronization. It has been shown in the previous chapters that inverse methods can be understood as spatial filters, which try to reduce the mixing of signals coming from different brain areas (figure 5.4 and table 4.2). In spite of the complicated spatial structure of the alpha rhythm (see left images in figure 6.11), the improved suppression can be understood qualitatively by a reduced influence of perturbing sources on the feedback procedure. This has been demonstrated in section 5.2 in numerical simulations.

Compared to the linear delayed feedback, the nonlinear one seems to enable a strong suppression of the alpha-rhythm while needing much less mean power for the stimulation. It is a minimal-invasive method in the sense that the flickering stops, if the rhythm disappears. In order to improve the performance for future experiments, more detailed information concerning the location of generators could be of relevance. The reconstructed current density distribution enables to use activity for the feedback coming from more specific brain areas, e.g. by the integration of brain maps as done in this experiment. The location dependent effects of the stimulation have to be studied. The restricted accuracy of the inverse techniques, which has been quantified in chapter 3 for a set of distributed source models, has to be kept in mind for the interpretation of results. More subjects have to be investigated to increase the significance of the conclusions. Brain rhythms in other frequency regimes, which may have the advantage to be more robust with respect to an appropriate control condition, should be tested.

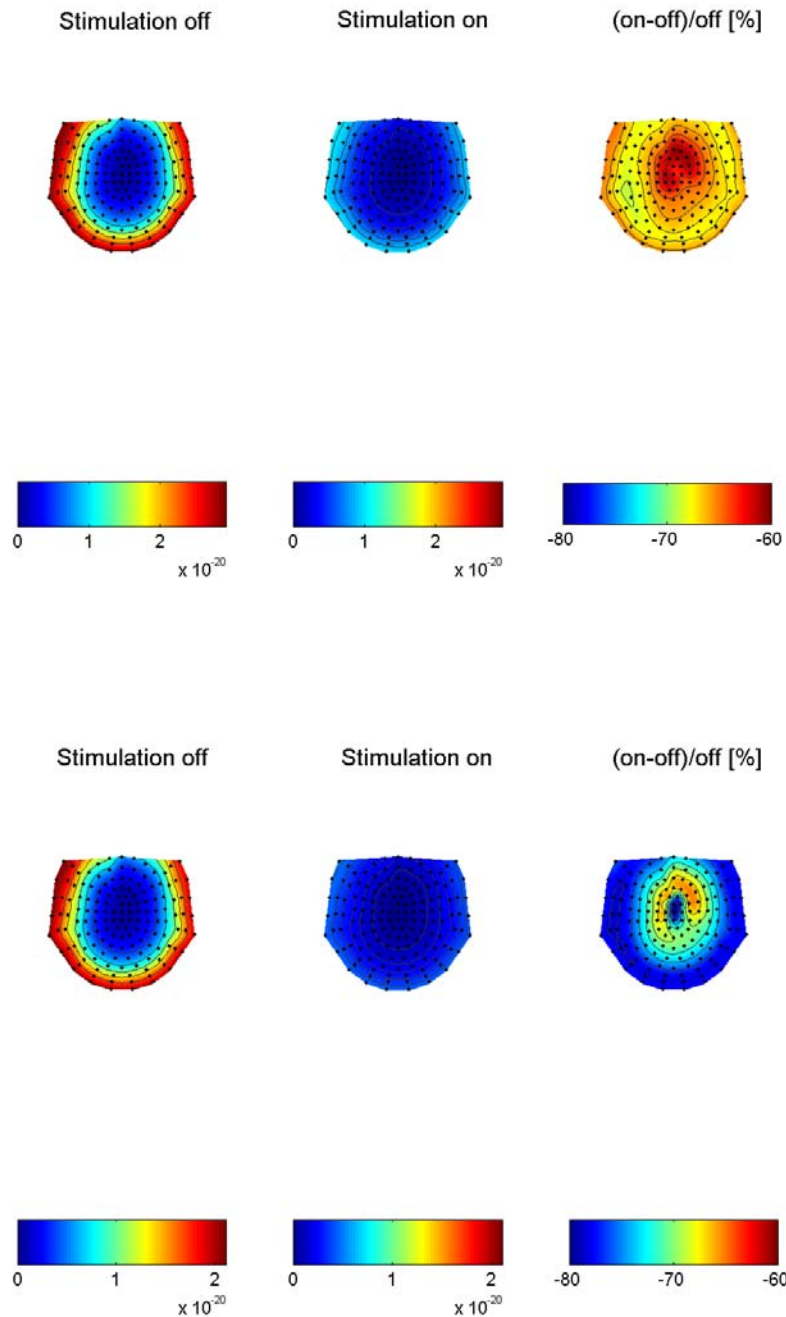


Figure 6.11: Color coded power spectral densities of the MEG sensor signals projected on two-dimensional maps (topview). In each map the bottom corresponds to the back of the sensor helmet. The maps are interpolated between the sensor positions which are indicated by black dots. Top: results from a run with *nonlinear delayed sensor feedback*. Bottom: results from a run with *nonlinear delayed voxel feedback*. Left pictures: the power spectral densities between 9 and 11 Hz are averaged and color coded for each sensor for the off-sequences. Middle pictures: corresponding maps for the on-sequences. Right pictures: the values of the middle maps are subtracted by the corresponding values in the maps shown left. In percentage of the off-values, the difference is presented again with the aid of a colored and interpolated map.

Chapter 7

Conclusions and outlook

In order to enable neurofeedback experiments, a study of competing distributed source models based on numerical simulations has been performed in the first part of this work. A weighted Minimum Norm called GaussMN, which exploits the empirical weighting function from the Magnetic Field Tomography, showed the best results regarding to realtime applications. If realistic detector noise is taken into account, GaussMN exhibits a significantly better performance than the popular sLORETA technique. These methods and the MFT, which is also common in many studies, have been compared here for the first time. For strong detector noise, single current dipoles can be reconstructed with an average localization error between 1.5 cm and 1.8 cm by GaussMN. The crucial regularization of inverse techniques has been handled by using a fixed value of the corresponding parameter in the Tikhonov regularization. As demonstrated here for the first time, this approach gives a better reconstruction accuracy than other regularization techniques in use.

The applied regularization moreover delivers a linear mapping between the MEG signals and the desired current density distribution in the human brain, which can be used in an online MEG system. This makes a tomography of the reconstructed cerebral current densities available to the physician within a second after generation of the MEG signals. In phantom experiments the correctness of the implementation of the reconstruction routine has been proved.

The realtime MEG system in combination with the GaussMN method has been successfully applied in a neurofeedback experiment using one subject. The realtime system uniquely guarantees a constant latency between the generation of the magnetic fluxes in the sensors and the stimulation of the volunteer. A linear delayed feedback protocol [RP04a] and a novel nonlinear delayed feedback technique introduced in [PHT05b] have been applied for processing the measured brain signals into a visual stimulation. For the nonlinear protocol it could be demonstrated with the aid of a control stimulation, that the sophisticated correlation between the stimulation signal and the realtime measured neural activity is the reason for a strong suppression of the alpha rhythm in the brain. This result proves the relevance of the realtime MEG system. The voxel feedback, i.e. using the reconstructed current densities in selected voxels for feedback, showed an enhanced effect compared to sensor feedback. This stresses the importance of the reconstruction of the current density distribution in the brain for feeding back activity from selective brain regions.

As the detailed multiple-dipole simulations have shown, the usefulness of three-dimensional tomographies to identify active brain regions is very questionable. Ghost sources and very blurred estimated current density distributions have been observed even for relatively simple source con-

figurations. The bottom line is that the accuracy of any biomagnetic inverse technique is limited by the underdetermination of the ill-posed problem. In order to reconstruct the current densities, the lead field matrix has to be inverted, whose number of rows is orders of magnitude larger than its number of columns in general. A compromise has been proposed in this work by the development of a spatial filter system called pWROP. In contrast to the SOFIA method, it proved to be useful in reducing considerably the contamination between predefined brain regions with respect to the reconstructed current density distribution. The costs of its application, which are unavoidable regarding to the ill-posed problem, are a decreased resolution of sources inside each region. This tradeoff can be tuned by a constraint parameter. pWROP should also be tested in the presence of detector noise. It could be very useful with respect to the realtime MEG system: much more localized brain signals would be fed back being less contaminated by other functional or anatomical different areas. Its benefit for the feedback gain has also been demonstrated in this work with the aid of numerical simulations.

The observed suppression of a brain rhythm by nonlinear delayed feedback stresses the relevance of this protocol. There is need to invest more efforts in continuative experiments. The phenomenon motivates a more physiologically appropriate modeling of the involved brain areas, especially regarding a potential application for the therapy of neurological diseases proposed in [PHT05b, THP06]. An extension of the nonlinear delayed feedback protocol in the framework of two interacting ensembles of oscillators [PHT05b] has been developed. Mixing the mean fields of populations exhibited an enhanced desynchronization and decoupling effect in simulations. By mixing the mean fields for the stimulation signal in the simulations, not only the driven ensemble can be stronger desynchronized. An appropriate setting of the mixing parameter also desynchronizes the driving population, although it is not directly affected by the stimulation. The modeling of the mean fields by macroscopic oscillators has to be improved for a deeper understanding.

Appendix A

Equivalent descriptions of the current density distribution in the Tikhonov regularization

The following identity will be shown:

$$(\Phi^T \Phi + \alpha L^T L)^{-1} \Phi^T = (L^T L)^{-1} \Phi^T (\Phi (L^T L)^{-1} \Phi^T + \alpha 1)^{-1} \quad (\text{A.1})$$

First it is:

$$\begin{aligned} \Phi^T (\Phi (L^T L)^{-1} \Phi^T + \alpha 1) &= \Phi^T \Phi (L^T L)^{-1} \Phi^T + \alpha \Phi^T \\ &= \Phi^T \Phi (L^T L)^{-1} \Phi^T + \alpha (L^T L) (L^T L)^{-1} \Phi^T \\ &= (\Phi^T \Phi + \alpha L^T L) (L^T L)^{-1} \Phi^T \end{aligned}$$

This gives

$$\Phi^T = (\Phi^T \Phi + \alpha L^T L) (L^T L)^{-1} \Phi^T (\Phi (L^T L)^{-1} \Phi^T + \alpha 1)^{-1} \quad (\text{A.2})$$

and finally

$$(\Phi^T \Phi + \alpha L^T L)^{-1} \Phi^T = (L^T L)^{-1} \Phi^T (\Phi (L^T L)^{-1} \Phi^T + \alpha 1)^{-1} \quad (\text{A.3})$$

Appendix B

Covariance matrices of multi-dimensional Gaussian distributions

In the following section it will be shown that for a multi-dimensional Gaussian distributed probability density function

$$p(\vec{x}) \propto e^{-\frac{1}{2}(\vec{x}^T A \vec{x})} \quad (\text{B.1})$$

the connection between matrix A (dimension: $n \times n$) and the covariance matrix V of the distribution is given by

$$A = V^{-1} \quad (\text{B.2})$$

Matrix A is supposed to be symmetric.

First let A be a diagonal matrix with diagonal elements A_{ii} so that:

$$p(\vec{x}) \propto \prod_{i=1}^n e^{-\frac{A_{ii}x_i^2}{2}} \quad (\text{B.3})$$

For this Gaussian distribution of independent components \vec{x}_i it follows for their variances: $\sigma_i^2 := \mathcal{E}((x_i - \mathcal{E}(x_i))^2)$ (\mathcal{E} : expectation value):

$$\sigma_i^2 = \frac{1}{A_{ii}} \quad (\text{B.4})$$

and $A = V^{-1}$, respectively. From this the more general situation of non-diagonal matrices A (but still symmetric ones) will be considered. With the aid of a singular-value-decomposition matrix, A can be written as

$$A' = UAU^T \quad (\text{B.5})$$

whereby A' is diagonal and for matrix U it holds:

$$UU^T = 1 \quad (\text{B.6})$$

Let y be defined as

$$\vec{y} = U\vec{x} \quad (\text{B.7})$$

With the transposed vector

$$\vec{y}^T = \vec{x}^T U^T \quad (\text{B.8})$$

the argument of the exponential function in equation B.1 is described by:

$$\vec{x}^T A \vec{x} = \vec{x}^T U^T U A U^T U \vec{x} = \vec{y}^T A' \vec{y} \quad (\text{B.9})$$

From this it follows for the covariance matrix V' of the distribution

$$p(\vec{y}) \propto e^{-\frac{1}{2}(\vec{y}^T A' \vec{y})} \quad (\text{B.10})$$

that

$$\begin{aligned} V' &= A'^{-1} \\ &= (U A U^T)^{-1} \\ &= U A^{-1} U^T \end{aligned}$$

Between two parameter sets \vec{y} and \vec{x} which are connected by a linear transformation U it can be shown with respect to their associated covariance matrices V and V' [Bar99]:

$$V = U^T V' U \quad (\text{B.11})$$

From this it follows finally

$$\begin{aligned} V &= U^T U A^{-1} U^T U \\ &= A^{-1} \end{aligned}$$

which had to be demonstrated.

Appendix C

Physical meaning of the Laplacian operator

The Laplacian gives the *smoothness* of a function. It measures the difference between the value of a function Ψ at a point and the mean value of surrounding points. A little to the left of

$$\Psi(x - a) = \Psi(x) - a \frac{\partial \Psi}{\partial x} + \frac{a^2}{2} \frac{\partial^2 \Psi}{\partial x^2} + \dots \quad (\text{C.1})$$

while a little to the right

$$\Psi(x + a) = \Psi(x) + a \frac{\partial \Psi}{\partial x} + \frac{a^2}{2} \frac{\partial^2 \Psi}{\partial x^2} + \dots \quad (\text{C.2})$$

On taking the average

$$\bar{\Psi} = \frac{1}{2} (\Psi(x - a) + \Psi(x + a)) = \Psi(x) + \frac{a^2}{2} \frac{\partial^2 \Psi}{\partial x^2} \quad (\text{C.3})$$

it follows

$$\bar{\Psi} - \Psi(x) = \frac{a^2}{2} \frac{\partial^2 \Psi}{\partial x^2} \quad (\text{C.4})$$

This argument can be extended to dimensions larger than 1. Thus the deviation from the value of Ψ at a point and its mean value in the surrounding region is proportional to $\Delta \Psi$.

Appendix D

Implementation of the nonlinear delayed feedback in the experiment

For the implementation of a delayed feedback in the experiment with the stimulation signal having the shape [PHT05b]

$$S(t) = K\bar{Z}^2(t)\bar{Z}^*(t - \tau) \quad (\text{D.1})$$

first the analytical form $\bar{Z}(t) = X(t) + iY(t)$ of the measured signal $X(t)$ has to be constructed (K : stimulation strength). As the considered frequencies in the performed visual experiment are situated near $10 \text{ Hz} = \frac{1}{100 \text{ ms}} =: T_\alpha^{-1}$, the imaginary part $Y(t)$ is approximated by $X(t - \tau_\alpha)$, whereby $\tau_\alpha := 0.25 \cdot T_\alpha$. For $S(t)$ this means

$$S(t) = K(X(t) + iX(t - \tau_\alpha))^2(X(t - \tau) - iX(t - \tau - \tau_\alpha)) \quad (\text{D.2})$$

$$= K(X(t)^2 + i2X(t)X(t - \tau_\alpha) - X(t - \tau_\alpha)^2)(X(t - \tau) - iX(t - \tau - \tau_\alpha)) \quad (\text{D.3})$$

$$= K(X(t)^2X(t - \tau) + i2X(t)X(t - \tau_\alpha)X(t - \tau) - X(t - \tau_\alpha)X(t - \tau) \quad (\text{D.4})$$

$$- iX(t - \tau - \tau_\alpha)X(t)^2 + 2X(t)X(t - \tau_\alpha)X(t - \tau - \tau_\alpha) \quad (\text{D.5})$$

$$+ iX(t - \tau - \tau_\alpha)X(t - \tau_\alpha)) \quad (\text{D.6})$$

The real part of $S(t)$ is used for the feedback signal, for which it holds

$$\text{real}(S(t)) = K(X(t)^2X(t - \tau) - X(t - \tau_\alpha)X(t - \tau) + 2X(t)X(t - \tau_\alpha)X(t - \tau - \tau_\alpha)) \quad (\text{D.7})$$

Bibliography

- [ADTG⁺04] L. Angelini, M. De Tommaso, M. Guido, K. Hu, P. Ivanov, D. Marinazzo, G. Nardulli, L. Nitti, M. Pellicoro, C. Pierro, and S. Stramaglia. Steady-state visual evoked potentials and phase synchronization in migraine patients. *Phys. Rev. Lett.*, 93(038103), 2004.
- [BAD⁺05] U. B. Barnikol, K. Amunts, J. Dammers, H. Mohlberg, T. Fieseler, A. Malikovic, K. Zilles, M. Niedeggen, and P.A. Tass. Pattern reversal visual evoked responses of V1/V2 and V5/MT as revealed by MEG combined with probabilistic cytoarchitectonic maps. *Neuroimage*, in press, 2005.
- [Bar99] R.J. Barlow. *Statistics - a guide to the use of statistical methods in the physical sciences*. John Wiley and Sons, West Sussex, UK, 1999.
- [BAS⁺02] O. Beck, A. Amann, E. Schöll, J.E.S. Socolar, and W. Just. Comparison of time-delayed feedback schemes for spatio-temporal control of chaos in a reaction-diffusion system with global coupling. *Phys. Rev. E*, 66(016213), 2002.
- [BASJ02] N. Baba, A. Amann, E. Schöll, and W. Just. Giant improvement of time-delayed feedback control by spatio-temporal filtering. *Phys. Rev. Lett.*, 89(074101), 2002.
- [BdJS⁺03] J.C Baayen, A. de Jongh, C.J. Stam, J.C. de Munck, J.J. Jonkman, D.G. Trenite, H.W. Berendse, A.M. van Walsum, J.J. Heimans, M. Puligheddu, J.A. Castelijns, and W.P. Vandertop. Localization of slow wave activity in patients with tumor-associated epilepsy. *Brain Topogr.*, 16(2):85–93, 2003.
- [BG68] G.E. Backus and J.F. Gilbert. The resolving power of gross earth data. *Geophys. J. R. Astron. Soc.*, 13:247–276, 1968.
- [BGLI99] J.P.R. Bolton, J. Gross, L.C. Liu, and A.A. Ioannides. SOFIA: Spatially optimal fast initial analysis of biomagnetic signals. *Phys. Med. Biol.*, 44:87–103, 1999.
- [BJS04] A.G. Balanov, N.B. Janson, and E. Schöll. Control of noise-induced oscillations by delayed feedback. *Physica D*, 199:1–12, 2004.
- [BJS05] A.G. Balanov, N.B. Janson, and E. Schöll. Delayed feedback control of chaos: Bifurcation analysis. *Phys. Rev. E*, 71(016222), 2005.

- [BML01] S. Baillet, J.C. Mosher, and R.M. Leahy. Electromagnetic brain mapping. *IEEE Signal Proc. Mag.*, 18(6):14–30, 2001.
- [Dö0] O. Dössel. *Bildgebende Verfahren in der Medizin*. Springer, Berlin, Germany, 2000.
- [Dam00] J. Dammers. Localisation and time courses of CMV generators from MFT analysis of average MEG signals, Phd thesis. *Reports of the Research Center Juelich, Germany*, 3808, 2000.
- [DI00] J. Dammers and A. Ioannides. Neuromagnetic localization of CMV generators using incomplete and full-head biomagnetometer. *Neuroimage*, 11(3):167–178, 2000.
- [DN02] K. Dolan and A. Neiman. Surrogate analysis of coherent multichannel data. *Phys. Rev. E*, 65(15):3291–3294, 2002.
- [dPMA99] R.G. de Peralta Menendez and S.G. Andino. Backus and Gilbert method for vector fields. *Hum. Brain Mapp.*, 7(161-165), 1999.
- [dPMA00a] R.G. de Peralta Menendez and S. Andino. Discussing the capabilities of Laplacian minimization. *Brain Topogr.*, 13(2):97–104, 2000.
- [dPMA00b] R.G. de Peralta Menendez and S.G. Andino. Discussing the capabilities of Laplacian minimization. *Brain Topogr.*, 13(2):97–104, 2000.
- [dPMHA⁺97] R.G. de Peralta Menendez, O. Hauk, S.G. Andino, H. Vogt, and C. Michel. Linear inverse solutions with optimal resolution kernels applied to electromagnetic tomography. *Hum. Brain Mapp.*, 5:454–467, 1997.
- [dSI05] A. de Sa and A. Infantosi. Evaluating the entrainment of the alpha rhythm during stroboscopic flash stimulation by means of coherence analysis. *Med. Eng. and Phys.*, 27:167–173, 2005.
- [EM98] M. Elliott and H. Müller. Synchronous information presented in 40-Hz flicker enhances visual feature binding. *Psychol. Sci.*, 9(4):277–283, 1998.
- [EWRKM83] S. Ed.: Williamson, G. Romani, L. Kaufman, and I. Modena. *Biomagnetism: an interdisciplinary approach*. Plenum Press, New York, USA, 1983.
- [FB05] C. Fox and D. Bryant. Inverse problems. at <http://www.math.auckland.ac.nz/phy707/>, 2005.
- [Fie00] T. Fieseler. *Analytic Source and Volume Conductor Models for biomagnetic fields*. Shaker Verlag, Aachen, Germany, 2000.
- [FWKW99] M. Fuchs, M. Wagner, T. Köhler, and H. Wischmann. Linear and nonlinear current density reconstructions. *J. Clin. Neurophysiol.*, 16(3):267–295, 1999.

- [GA99] J. Gross and Ioannides. A.A. Linear transformations of data space in MEG. *Phys.Med.Biol.*, 44:2081–2097, 1999.
- [GHW79] G. Golub, M. Heath, and G. Wahba. Generalized cross-validation as a method for choosing a good ridge parameter. *Technometrics*, 21(2):215–223, 1979.
- [GOP05] R.E. Greenblatt, A. Ossatdchi, and M.E. Pflieger. Local linear estimators for the bioelectromagnetic inverse problem. *IEEE Trans. Signal Processing*, 53:3403–3412, 2005.
- [Hel53] H. Helmholtz. Ueber einige Gesetze der Vertheilung elektrischer Ströme in körperlichen Leitern mit Anwendung auf die thierisch-elektrischen Versuche. *Ann. Physik und Chemie*, 9:211–33, 1853.
- [HFE01] T. Heil, I. Fischer, and W. Elsässer. Dynamics of semiconductor lasers subject to delayed optical feedback: the short cavity regime. *Phys. Rev. Lett.*, 87(243901), 2001.
- [HFE03] T. Heil, I. Fischer, and W. Elsässer. Delay dynamics of semiconductor lasers with short external cavities: bifurcation scenarios and mechanisms. *Phys. Rev. E*, 67(066214), 2003.
- [HHR⁺93] M.S. Hämäläinen, R. Hari, J. Risto, R.J. Ilmoniemi, J. Knuutila, and O.V. Lounasmaa. Magnetoencephalography - theory, instrumentation, and applications to non-invasive studies of the working human brain. *Rev. Mod. Phys.*, 65(2):413–497, 1993.
- [HI94] M.S. Hämäläinen and R.J. Ilmoniemi. Interpreting magnetic fields of the brain: minimum norm estimates. *Med. Biol. Eng. Comput.*, 32:35–42, 1994.
- [HS05] P. Hövel and E. Schöll. Control of unstable steady states by time-delayed feedback methods. *Phys. Rev. E*, 72(046203), 2005.
- [IBC90] A.A. Ioannides, J.P.R. Bolton, and C.J.S. Clarke. Continuous probabilistic solutions to the biomagnetic inverse problem. *Inverse Probl.*, 6:523–542, 1990.
- [JBS04] N.B. Janson, A.G. Balanov, and E. Schöll. Delayed feedback as a means of control of noise-induced motion. *Phys. Rev. Lett.*, 93(010601), 2004.
- [JPA⁺03] W. Just, S. Popovich, A. Amann, N. Baba, and E. Schöll. Improvement of time-delayed feedback control by periodic modulation: analytical theory of Floquet mode control scheme. *Phys. Rev. E*, 67(026222), 2003.
- [KSJ00] E. Kandel, J. Schwartz, and T. Jessell. *Principles of Neural Science*. McGraw-Hill Medical, New York, USA, 2000.
- [Kur84] Y. Kuramoto. *Chemical Oscillations, Waves and Turbulence*. Springer-Verlag, Berlin, Germany, 1984.

- [LHR96] M. Linden, T. Habib, and V. Radojevic. A controlled study of the effects of EEG biofeedback on cognition and behavior of children with attention deficit disorder and learning disabilities. *Biofeedback Self-Reg.*, 21(1):35–49, 1996.
- [LR00] V. Lamme and P. Roelfsema. The distinct modes of vision offered by feedforward and recurrent processing. *Trends Neurosci.*, 23:571–579, 2000.
- [LSH⁺05] T.N. Lal, M. Schröder, J. Hill, H. Preissl, T. Hinterberger, J. Mellinger, M. Bogdan, W. Rosenstiel, T. Hofmann, N. Birbaumer, and B. Schölkopf. A brain computer interface with online feedback based on magnetoencephalography. *Proceedings of the 22nd International Conference on Machine Learning*, pages 465–472, 2005.
- [Lub97] J.F. Lubar. Neocortical dynamics: implications for understanding the role of neurofeedback and related techniques for the enhancement of attention. *Appl. Psychophys. Biof.*, 22(2):111–126, 1997.
- [MIY92] H. Matsuba, D. Irisawa, and A. Yahara. *Superconducting shield for biomagnetism measurements coupled with ferro-magnetic*. In: Hoke, M. and Erne, S. and Okada, Y. and Romani, G. (Eds.) *Biomagnetism: Clinical Aspects*. Elsevier, Amsterdam, The Netherlands, 1992.
- [MLC⁺03] F. Moradi, L.C. Liu, K. Cheng, R.A. Waggoner, K. Tanaka, and A.A. Ioannides. Consistent and precise localization of brain activity in human primary visual cortex by MEG and fMRI. *Neuroimage*, 18(3):595–609, 2003.
- [MLL92] J. Mosher, P. Lewis, and R. Leahy. Multiple dipole modeling and localization from spatio-temporal MEG data. *IEEE Trans. Biomed. Eng.*, 39:541–557, 1992.
- [MML⁺04] C. Michel, M. Murray, G. Lantz, S. Gonzales, L. Spinelli, and R. Grave de Peralta. EEG source imaging. *Clin. Neurophysiol.*, 115:2195–2222, 2004.
- [OJLSH95] W.W. Orrison Jr., J.D. Lewine, J.A. Sanders, and M.F. Hartshorne. *Functional Brain Imaging*. Mosby-Year Book, St. Louis, USA, 1995.
- [PAS05] J. Pomplun, A. Amann, and E. Schöll. Mean field approximation of time-delayed feedback control of noise-induced oscillations in the Van der Pol system. *Europhys. Lett.*, 71(366), 2005.
- [PHT05a] O. Popovych, C. Hauptmann, and P.A. Tass. Demand-controlled desynchronization of brain rhythms by means of nonlinear delayed feedback. *Proceedings of the 2005 IEEE Engineering in Medicine and Biology, 27th Annual Conference Shanghai, China*, page 4 pages, 2005.
- [PHT05b] O. Popovych, C. Hauptmann, and P.A. Tass. Effective desynchronization by nonlinear delayed feedback. *Phys. Rev. Lett.*, 94(164102), 2005.
- [PHT06a] O. Popovych, C. Hauptmann, and P.A. Tass. Control of neuronal synchrony by nonlinear delayed feedback. *Biol. Cybern.*, in press, 2006.

- [PHT06b] O. Popovych, C. Hauptmann, and P.A. Tass. Desynchronization and decoupling of interacting oscillators by nonlinear delayed feedback. *Int. J. Bif. Chaos*, in press, 2006.
- [PM99a] R.D. Pascual-Marqui. Reply to comments made by R. Grave De Peralta Menendez and S.I. Gozalez Andino. at <http://www.ee.tut.fi/rgi/ijbem/volume1/number2/html/pascual.htm>, 1999.
- [PM99b] R.D. Pascual-Marqui. Review of methods for solving the EEG inverse problem. *Bioelectromag.*, 1(1):75–86, 1999.
- [PM02] R.D. Pascual-Marqui. Standardized low resolution brain electromagnetic tomography (sLORETA): technical details. *Method. Find. Exp. Clin.*, 24D:5–12, 2002.
- [PMML94] R.D. Pascual-Marqui, C. M. Michel, and D. Lehmann. Low Resolution Electromagnetic Tomography: a new method for localizing electrical activity in the brain. *Int. J. Psychol.*, 18:49–65, 1994.
- [PR99] A. Pikovsky and S. Ruffo. Finite-size effects in a population of interacting oscillators. *Phys. Rev. E*, 59:1633–1636, 1999.
- [PRK01] A. Pikovsky, M. Rosenblum, and J. Kurths. *Synchronization, a universal concept in nonlinear sciences*. Cambridge University Press, Cambridge, UK, 2001.
- [PTVF92] W.H. Press, S.A. Teukolsky, W.T. Vetterling, and B.P. Flannery. *Numerical recipes in C*. Cambridge Univ. Press, Cambridge, UK, 1992.
- [Pyr92] K. Pyragas. Continuous control of chaos by self-controlling feedback. *Phys. Lett. A*, 170:421–428, 1992.
- [RJ00] A. Reddy and G.L. Johnston. Dynamics of a limit cycle oscillator under time delayed linear and nonlinear feedbacks. *Physica D*, 144:335–357, 2000.
- [Ron06] H. Rongen. Echtzeitsystem für die Phasenrücksetzung und Phasensynchronisationstomographie von MEG Signalen. *Inauguraldissertation zur Erlangung des akademischen Grades eines Doktors der Naturwissenschaften der Universität Mannheim*, submitted in February 2006.
- [RP04a] M.G. Rosenblum and A.S. Pikovsky. Controlling synchronization in an ensemble of globally coupled oscillators. *Phys. Rev. Lett.*, 92(114102), 2004.
- [RP04b] M.G. Rosenblum and A.S. Pikovsky. Delayed feedback control of collective synchrony: an approach to suppression of pathological brain rhythms. *Phys. Rev. E*, 70(041904), 2004.
- [Sar87] J. Sarvas. Basic mathematical and electromagnetic concepts of the biomagnetic inverse problem. *Phys. Med. Biol.*, 32(1):11–22, 1987.

- [SBS06] G. Stegemann, G. Balanov, and E. Schöll. Delayed feedback control of stochastic spatiotemporal dynamics in a resonant tunneling diode. *Phys. Rev. E*, 73(16203), 2006.
- [Sch04] E. Schöll. Pattern formation in semiconductors: control of spatio-temporal dynamics. *Ann. Phys. (Leipzig)*, 13(407), 2004.
- [SLRH05] P. Schimpf, H. Liu, C. Ramon, and J. Haueisen. Efficient electromagnetic source imaging with adaptive standardized LORETA/FOCUSS. *IEEE Trans. Biomed. Eng.*, 52(5):901–908, 2005.
- [SM97] P. Stoica and R. Moses. *Introduction to spectral analysis*. Prentice-Hall, Englewood, USA, 1997.
- [SPA+05] E. Schöll, J. Pomplun, A. Amann, A.G. Balanov, and N.B. Janson. Time-delay feedback control of nonlinear stochastic oscillations. *ENOC-2005 Conference proceedings*, 2005.
- [SSN05] K. Sekihara, M. Sahani, and S.S. Nagarajan. Localization bias and spatial resolution of adaptive and non-adaptive spatial filters for MEG source reconstruction. *Neuroimage*, 25(4):1056–1067, 2005.
- [Str00] S. Strogatz. *Nonlinear dynamics and chaos*. Westview Press, Cambridge, USA, 2000.
- [SvC86] M. Scherg and D. von Cramon. Evoked dipole source potentials of the human auditory cortex. *Electroen. Clin. Neuro.*, 65:344–360, 1986.
- [SW89] H.G. Schuster and P. Wagner. Mutual entrainment of two limit cycle oscillators with time delayed coupling. *Progr. Theor. Phys.*, 81:939–945, 1989.
- [Swi96] P.G. Swingle. Neurofeedback treatment of pseudoseizure disorder. *Biol. Psychiat.*, 44(11):1196–1199, 1996.
- [Tas01a] P.A. Tass. Desynchronizing double-pulse phase resetting and application of deep brain stimulation. *Biol. Cybern.*, 85:343–354, 2001.
- [Tas01b] P.A. Tass. Effective desynchronization by means of double-pulse phase resetting. *Europhys. Lett.*, 53:15–21, 2001.
- [Tas01c] P.A. Tass. Effective desynchronization with a resetting pulse train followed by a single pulse. *Europhys. Lett.*, 55:171–177, 2001.
- [Tas02] P.A. Tass. Desynchronization of brain rhythms with soft phase-resetting techniques. *Biol. Cybern.*, 87:102–115, 2002.
- [Tas03] P.A. Tass. A model of desynchronizing deep brain stimulation with a demand-controlled coordinated reset of neural subpopulations. *Biol. Cybern.*, 89:81–88, 2003.

- [Tas04] P.A. Tass. Transmission of stimulus-locked responses in two oscillators with bistable coupling. *Biol. Cybern.*, 91:203–211, 2004.
- [TBAVVS04] N.J. Trujillo-Barreto, E. Aubert-Vazquez, and P.A. Valdes-Sosa. Bayesian model averaging in EEG/MEG imaging. *Neuroimage*, 21:1300–1319, 2004.
- [TFD⁺03] P.A. Tass, T. Fieseler, J. Dammers, K. Dolan, P. Morosan, M. Majtanik, F. Boers, A. Muren, K. Zilles, and G.R. Fink. Synchronization tomography: a method for three-dimensional localization of phase synchronized neuronal populations in the human brain using magnetoencephalography. *Phys. Rev. Lett.*, 9008(8101), 2003.
- [Tho02] K.E. Thornton. The improvement/rehabilitation of auditory memory functioning with EEG. *Neurorehabilitation*, 17(1):69–80, 2002.
- [THP06] P.A. Tass, C. Hauptmann, and O. Popovych. Development of therapeutic brain stimulation techniques with methods from nonlinear dynamics and statistical physics. *Int. J. Bif. Chaos*, in press, 2006.
- [TIMG99] J. Taylor, A. Ioannides, and H. Müller-Gärtner. Mathematical analysis of lead field expansions. *IEEE T. Med. Image*, 2:151–163, 1999.
- [TIV01] A. Tzelepi, A.A. Ioannides, and Poghosyan V. Early (N70m) neuromagnetic signal topography and striate and extrastriate generators following pattern onset quadrant stimulation. *Neuroimage*, 13(4):702–718, 2001.
- [TRW⁺98] P.A. Tass, M. Rosenblum, J. Weule, J. Kurths, A. Pikovsky, J. Volkmann, A. Schnitzler, and H.-J. Freund. Detection of n:m phase locking from noisy data: application to magnetoencephalography. *Phys. Rev. Lett*, 81(026108):1–6, 1998.
- [TY⁺99] K. Toyama, K. Yoshikawa, Y. Yoshida, Y. Kondo, S. Tomita, Takanashi, Y. Ejima, and S. Yoshizawa. A new method for magnetoencephalography: a three-dimensional magnetometer-spatial filter system. *Neuroscience*, 91(2):405–415, 1999.
- [vVvDYS97] B. van Veen, W. van Dronglen, M. Yuchtman, and A. Suzuki. Localization of brain electric activity via linearly constrained minimum variance spatial filtering. *IEEE Trans. Biomed. Eng.*, 44:867–880, 1997.
- [WFK04] M. Wagner, M. Fuchs, and J. Kastner. Evaluation of sLORETA in the presence of noise and multiple sources. *Brain Topogr.*, 16(4):277–280, 2004.
- [ZSPGA02] K. Zilles, A. Schleicher, N. Palomero-Gallagher, and K. Amunts. *Quantitative analysis of cyto- and receptor architecture of the human brain. In: Mazziotta, J.C., and Toga, A. (Eds.), Brain Mapping: The Methods, 2nd. Ed. Academic Press, San Diego, USA, 2002.*

Publications

Volker Hadamschek, Jrgen Dammers, Thomas Fieseler, Kevin Dolan, Peter Tass
Reconstruction of current distribution in the human brain: truncating the singular value decomposition in inverse algorithms with regard to MEG data.
Biomag Conference 2004, poster.

Volker Hadamschek, Ernesto Palmero-Soler, Juergen Dammers, Thomas Fieseler, Peter Tass
A comparative study of MEG inverse methods: weighted Minimum Norm, MFT, and sLORETA.
Submitted to Phys.Med.Biol., 2006.

Acknowledgements

First of all, I thank Prof. Dr. Eckehard Schöll, Prof. Dr. Dr. Peter A. Tass, and Prof. Dr. Erwin Sedlmayr for supervising my work. Especially I acknowledge Prof. Dr. Dr. Peter A. Tass for giving me the opportunity for this thesis in a difficult economic trend, for the granted trust as well as freedom in this time, and for his scientific stimulations.

The fruitful collaboration with Heinz Rongen and Milan Majtanik regarding the implementation of the realtime MEG system and the experiment with visual stimulation was a pleasure for me. I am indebted to Dr. Oleksandr Popovych and Dr. Kevin Dolan for their very helpful and friendly hints with respect to nonlinear dynamics and to computer programming.

I enjoyed the warm and valuable support by Dr. Thomas Fieseler, Dr. Jürgen Dammers, and Andrea Muren. I thank Ernesto Palmero-Soler for very important information concerning the biomagnetic inverse problem.

My uncle Rainer Beckers paid great attention and advice to me in critical moments. Last, but not most, I thank my parents, Gisela and Gerd Hadamschek, for their love, for their values, and for their support in countless situations.